

# Nearby early-type galaxies with ionized gas

## IV. Origin and powering mechanism of the ionized gas<sup>★,★★</sup>

F. Annibali<sup>1</sup>, A. Bressan<sup>1,2,3</sup>, R. Rampazzo<sup>1</sup>, W. W. Zeilinger<sup>4</sup>, O. Vega<sup>3</sup>, and P. Panuzzo<sup>5</sup>

<sup>1</sup> INAF – Osservatorio Astronomico di Padova, vicolo dell’Osservatorio 5, 35122 Padova, Italy

e-mail: francesca.annibali@oapd.inaf.it [alessandro.bressan;roberto.rampazzo]@oapd.inaf.it

<sup>2</sup> SISSA/ISAS, via Beirut 2-4, 34151 Trieste, Italy

<sup>3</sup> INAOE, Luis Enrique Erro 1, 72840 Tonantzintla, Puebla, Mexico

e-mail: ovega@inaoep.mx

<sup>4</sup> Institut für Astronomie der Universität Wien, Türkenschanzstrae 17, 1180 Wien, Austria

e-mail: zeilinger@astro.univie.ac.at

<sup>5</sup> CEA Saclay/Service d’Astrophysique, Laboratoire AIM, CEA/DSM/IRFU-CNRS-Université Paris Diderot,

91191 Gif-sur-Yvette Cedex, France

e-mail: pasquale.panuzzo@cea.fr

Received 30 November 2009 / Accepted 8 April 2010

### ABSTRACT

**Aims.** A significant fraction of early-type galaxies (ETGs) exhibit emission lines in their optical spectra. We attempt to identify the producing the emission mechanism and the ionized gas in ETGs, and its connection with the host galaxy evolution.

**Methods.** We analyzed intermediate-resolution optical spectra of 65 ETGs, mostly located in low density environments and exhibiting spectroscopic diagnostic lines of ISM from which we had previously derived stellar population properties. To extract the emission lines from the galaxy spectra, we developed a new fitting procedure that accurately subtracts the underlying stellar continuum, and accounts for the uncertainties caused by the age-metallicity degeneracy.

**Results.** Optical emission lines are detected in 89% of the sample. The incidence and strength of emission correlate with neither the E/S0 classification, nor the fast/slow rotator classification. By means of the classical [OIII]/H $\beta$  versus [NII]/H $\alpha$  diagnostic diagram, the nuclear galaxy activity is classified such that 72% of the galaxies with emission are LINERs, 9% are Seyferts, 12% are composite/transition objects, and 7% are non-classified. Seyferts have young luminosity-weighted ages ( $\lesssim 5$  Gyr), and appear, on average, significantly younger than LINERs and composites. Excluding the Seyferts from our sample, we find that the spread in the ([OIII], H $\alpha$ , or [NII]) emission strength increases with the galaxy central velocity dispersion  $\sigma_c$ . Furthermore, the [NII]/H $\alpha$  ratio tends to increase with  $\sigma_c$ . The [NII]/H $\alpha$  ratio decreases with increasing galactocentric distance, indicative of either a decrease in the nebular metallicity, or a progressive “softening” of the ionizing spectrum. The average nebular oxygen abundance is slightly less than solar, and a comparison with the results obtained in Paper III from Lick indices shows that it is  $\approx 0.2$  dex lower than that of stars.

**Conclusions.** The nuclear ( $r < r_e/16$ ) emission can be attributed to photoionization by PAGB stars alone only for  $\approx 22\%$  of the LINER/composite sample. On the other hand, we cannot exclude an important role of PAGB star photoionization at larger radii. For the major fraction of the sample, the nuclear emission is consistent with excitation caused by either a low-accretion rate AGN or fast shocks (200–500 km s<sup>-1</sup>) in a relatively gas poor environment ( $n \lesssim 100$  cm<sup>-3</sup>), or both. The derived [SII] $\lambda$ 6717/ $\lambda$ 6731 ratios are consistent with the low gas densities required by the shock models. The derived nebular metallicities are indicative of either an external origin of the gas, or an overestimate of the oxygen yields by SN models.

**Key words.** galaxies: elliptical and lenticular, cD – galaxies: ISM – galaxies: active – galaxies: abundances

## 1. Introduction

Early-type galaxies (ETGs) have long been considered to be inert stellar systems, essentially devoid of gas and dust. However, this view has radically changed since a number of imaging and spectroscopy studies from both the ground and space have revealed the presence of a multiphase interstellar medium (ISM): a hot ( $T \sim 10^6$ – $10^7$  K), X-ray emitting halo (Forman & Jones 1985; Fabbiano et al. 1992; O’Sullivan et al. 2001); a warm ( $T \sim 10^4$  K) gas (often referred to as “ionized gas”) (e.g., Phillips et al. 1986; Sadler & Gerhard 1985; see also Goudfrooij 1999

for a review); and colder components detected in the mid and far infrared, CO and HI (for reviews see Sadler et al. 2002; Temi et al. 2004; Bressan et al. 2006; Sage & Welch 2006; Morganti et al. 2006; Helmboldt 2007; Oosterloo et al. 2007; Panuzzo et al. 2007). The hot gas component dominates the ISM in E/S0 galaxies, and only comparatively small quantities are detected in the warm and cold phases (Bregman et al. 1992). The derived masses of the warm ISM range from  $\sim 10^3$  to  $\sim 10^6 M_\odot$  (Phillips et al. 1986; Trinchieri & di Serego Alighieri 1991; Macchetto et al. 1996; Goudfrooij et al. 1994a, 1994b, 1994c; Goudfrooij & de Jong 1995), orders of magnitude below the X-ray emitting hot ISM and the stellar mass. Ionized gas is detected in 40–80% of early-type galaxies from their optical emission lines (Caldwell 1984; Phillips et al. 1986; Macchetto et al. 1996; Sarzi et al. 2006, 2009; Yan et al. 2006; Serra et al. 2008).

\* Based on observations obtained at the European Southern Observatory, La Silla, Chile.

\*\* Appendix and Tables 2 and 3 are only available in electronic form at <http://www.aanda.org>

The ionized gas is also usually morphologically associated with dust (Kim 1989; Goudfrooij et al. 1994c).

Despite the number of studies, several issues remain open. The first problem is the origin of the ISM in ETGs. Narrow-band imaging centered around  $H\alpha + [\text{NII}]\lambda 6584$  shows that the ionized gas has a variety of morphologies, from regular, disk-like structures, to filamentary structures (Demoulin-Ulrich et al. 1984; Buson et al. 1993; Macchetto et al. 1996; Zeilinger et al. 1996; Martel et al. 2004; Sarzi et al. 2006). Evidence of the acquisition of external gas comes from kinematical studies showing that the angular momentum of the gas is often decoupled from that of the stars (Bertola et al. 1992; van Dokkum & Franx 1995; Caon et al. 2000), even if according to Sarzi et al. (2006) the angular momenta are inconsistent with a purely external origin for the gas. That the ionized gas emission is always associated with dust (e.g. Tran et al. 2001) tends to exclude “cooling flows” as the origin of the warm gas in E/S0 galaxies (Goudfrooij 1999). In the scenarios proposed by Sparks et al. (1989) and de Jong et al. (1990), the dusty filaments can arise from the interaction of a small gas-rich galaxy with the giant elliptical, or from a tidal accretion event in which the gas and dust are stripped from a passing spiral (see e.g. Domingue et al. 2003; Tal et al. 2009).

The history of star formation and evolution leaves its chemical signature in the ISM of ETGs. Historically, X-ray abundance measurements of the hot ISM have been problematic, as typified by the so-called Fe discrepancy (Arimoto et al. 1997). *Chandra* and *XMM* measurements of X-ray bright galaxies at the center of groups have inferred roughly solar or even slightly supersolar abundances for the ISM (e.g. Gastaldello & Molendi 2002; Buote et al. 2003; Tamura et al. 2003) and claimed no evidence of very subsolar Fe abundances (Humphrey & Buote 2006; Ji et al. 2009). These studies also report anomalously low oxygen abundances compared to iron and magnesium. This is in conflict with results from SN stellar yields if one assumes that the source of ISM is the material injected into interstellar space by evolved stars. Until now, the only study of metallicity in the warm ISM has been that of Athey & Bregman (2009), who derived oxygen abundances for seven ETGs from optical emission lines. The authors find on average a solar metallicity, favoring an internal origin of the warm ISM. However, this study is limited by the small sample. Determining the metallicity of the warm ISM is fundamental to creating a link between the hot gas phase and the galaxy stellar population, and discriminating between an internal and an external origin of the interstellar matter in E/S0 galaxies.

The second open issue concerns the ionizing source of the warm gas. Optical spectroscopic studies show that ETGs are typically classified as LINERs (Low-Ionization Nuclear Emission-line Regions, Heckman 1980) according to their emission line ratios (e.g. Phillips et al. 1986; Yan et al. 2006). However, there is a strong debate about the ionization mechanism in LINERs. At present, the most viable excitation mechanisms are: a low accretion-rate AGN (e.g., Ho 1999b; Kewley et al. 2006; Ho 2009a), photoionization by old post-asymptotic giant branch (PAGB) stars (e.g. Trinchieri & di Serego Alighieri 1991; Binette et al. 1994; Stasińska et al. 2008), and fast shocks (Koski & Osterbrock 1976; Heckman 1980; Dopita & Sutherland 1995; Allen et al. 2008). The AGN mechanism is strongly supported by the detection of broad emission lines in optical spectra (e.g. Ho et al. 1997a; Wang & Wei 2008), by the properties of the X-ray emission (Terashima et al. 2000; Flohic et al. 2006; Gonzalez-Martín et al. 2009), by the presence of UV and X-ray variability (e.g. Maoz et al. 2005; Pian et al. 2010), and by the evidence that massive black holes (BHs) appear to be a generic component of galaxies with a bulge (Magorrian et al. 1998;

Ho 1999a; Kormendy 2004). PAGB stars are good candidates because their radiation, much harder than that from young stars, is able to reproduce the observed emission-line ratios in LINERs (Trinchieri & di Serego Alighieri 1991; Binette et al. 1994; Stasińska et al. 2008). The most compelling evidence in support of the PAGB mechanism is the finding that the emission-line flux correlates very well with the host galaxy stellar luminosity within the emission-line region (Macchetto et al. 1996), and that the emission-line flux distribution follows that of the stellar continuum (Sarzi et al. 2006, 2009). These correlations suggest that the source of ionizing photons is distributed in the same way as the stellar population. LINERs emission has also been observed in extranuclear regions associated with large-scale outflows and related shocks (Lípari et al. 2004), or regions shocked by radio jets (Cecil et al. 2000).

Evidence is growing that more than one mechanism may operate in LINERs. Sarzi et al. (2009) showed that the role of AGN activity is confined to the central regions, whereas at larger radii the stellar and nebular fluxes correlate with each other, which is indicative of a stellar ionizing source. Eracleous et al. (2010) showed that low accretion-rate AGNs do not produce enough ionizing photons to explain the observed  $H\alpha$  luminosities within a  $2'' \times 4''$  aperture, so that other mechanisms are needed.

To help us understand the formation history of ETGs, and the connection between the stellar populations and the ionized gas, we analyzed intermediate-resolution optical spectra for a sample of 65 field E/S0 galaxies (Rampazzo et al. 2005, hereafter Paper I; Annibali et al. 2006, hereafter Paper II). The stellar population properties (i.e., ages, metallicities, and elements abundance ratios) were derived at different radii in Annibali et al. (2007, hereafter Paper III) by means of the analysis of the Lick indices. In this paper, we present the study of the optical emission lines in annuli of increasing galactocentric distance. The purpose is to characterize the properties of the ionized gas, its origin, and the possible excitation mechanisms at different radii.

The paper is organized as it follows. In Sect. 2, we provide a brief overview of the sample. In Sect. 3, we describe the method used to extract the emission-line fluxes from the optical spectra. In Sect. 4, we provide a spectral classification inferred from standard diagnostic diagrams, and investigate possible correlations with the host galaxy properties. In Sect. 5, we determine the oxygen metallicity. In Sect. 6, we compare our data with the models. A summary and the conclusions are given in Sect. 7.

## 2. Sample overview

The Rampazzo et al. (2005) + Annibali et al. (2006) sample (hereafter R05+A06 sample) was selected from a compilation of ETGs exhibiting evidence of an ISM in at least one of the following bands: IRAS 100  $\mu\text{m}$ , X-ray, radio, HI, and CO (Roberts et al. 1991). All galaxies belong to the *Revised Shapley Ames Catalog of Bright Galaxies* (RSA) (Sandage & Tammann 1987) and have a redshift lower than  $\sim 5500 \text{ km s}^{-1}$ . Because of the selection criteria, the sample is biased toward the presence of emission lines. Table 1 summarizes the main characteristics of the sample. Column (1) gives the galaxy identification name; Cols. (2) and (3) provide the galaxy morphological classification according to RSA (Sandage & Tammann 1987) and RC3 (de Vaucouleurs et al. 1991), respectively: only in few cases do the two catalogues disagree in the distinction between E and S0 classes; Col. (4) provides the central velocity dispersion from HYPERLEDA<sup>1</sup>; Col. (5) gives the effective radius  $r_e$  from

<sup>1</sup> <http://leda.univ-lyon1.fr>

Table 1. Sample overview.

Galaxy Id	RSA	RC3	$\sigma_c$ km s <sup>-1</sup>	$r_e$ arcsec	$V_{hel}$ km s <sup>-1</sup>	$\rho_{xyz}$ gal Mpc <sup>-3</sup>	Age Gyr	Z	[ $\alpha$ /Fe]
NGC 128	S02(8) pec	S0 pec sp	183	17.3	4227		9.7 ± 1.7	0.024 ± 0.004	0.16 ± 0.03
NGC 777	E1	E1	317	34.4	5040		5.4 ± 2.1	0.045 ± 0.020	0.28 ± 0.10
NGC 1052	E3/S0	E4	215	33.7	1475	0.49	14.5 ± 4.2	0.032 ± 0.007	0.34 ± 0.05
NGC 1209	E6	E6:	240	18.5	2619	0.13	4.8 ± 0.9	0.051 ± 0.012	0.14 ± 0.02
NGC 1297	S02/3(0)	SAB0 pec:	115	28.4	1550	0.71	15.5 ± 1.2	0.012 ± 0.001	0.29 ± 0.04
NGC 1366	E7/S01(7)	S0 sp	120	10.6	1310	0.16	5.9 ± 1.	0.024 ± 0.004	0.08 ± 0.03
NGC 1380	S03(7)/Sa	SA0	240	20.3	1844	1.54	4.4 ± 0.7	0.038 ± 0.006	0.24 ± 0.02
NGC 1389	S01(5)/SB01	SAB(s)0-:	139	15.0	986	1.50	4.5 ± 0.6	0.032 ± 0.005	0.08 ± 0.02
NGC 1407	E0/S01(0)	E0	286	70.3	1766	0.42	8.8 ± 1.5	0.033 ± 0.005	0.32 ± 0.03
NGC 1426	E4	E4	162	25.0	1443	0.66	9.0 ± 2.5	0.024 ± 0.005	0.07 ± 0.05
NGC 1453	E0	E2	289	25.0	3906		9.4 ± 2.1	0.033 ± 0.007	0.22 ± 0.03
NGC 1521	E3	E3	235	25.5	4165		3.2 ± 0.4	0.037 ± 0.006	0.09 ± 0.02
NGC 1533	SB02(2)/SBa	SB0-	174	30.0	773	0.89	11.9 ± 6.9	0.023 ± 0.020	0.21 ± 0.10
NGC 1553	S01/2(5)pec	SA(r)0	180	65.6	1280	0.97	4.8 ± 0.7	0.031 ± 0.004	0.10 ± 0.02
NGC 1947	S03(0) pec	S0- pec	142	32.1	1100	0.24	5.9 ± 0.8	0.023 ± 0.003	0.05 ± 0.02
NGC 2749	E3	E3	248	33.7	4180		10.8 ± 2.3	0.027 ± 0.006	0.25 ± 0.04
NGC 2911	S0p or S03(2)	SA(s)0: pec	235	50.9	3131		5.7 ± 2.0	0.034 ± 0.019	0.25 ± 0.10
NGC 2962	RSB02/Sa	RSAB(rs)0+		23.3	2117	0.15			
NGC 2974	E4	E4	220	24.4	1890	0.26	13.9 ± 3.6	0.021 ± 0.005	0.23 ± 0.06
NGC 3136	E4	E:	230	36.9	1731	0.11	1.5 ± 0.1	0.089 ± 0.004	0.36 ± 0.02
NGC 3258	E1	E1	271	30.0	2778	0.72	4.5 ± 0.8	0.047 ± 0.013	0.21 ± 0.03
NGC 3268	E2	E2	227	36.1	2818	0.69	9.8 ± 1.7	0.023 ± 0.004	0.34 ± 0.04
NGC 3489	S03/Sa	SAB(rs)+	129	20.3	693	0.39	1.7 ± 0.1	0.034 ± 0.004	0.05 ± 0.02
NGC 3557	E3	E3	265	30.0	3038	0.28	5.8 ± 0.8	0.034 ± 0.004	0.17 ± 0.02
NGC 3607	S03(3)	SA(s)0:	220	43.4	934	0.34	3.1 ± 0.5	0.047 ± 0.012	0.24 ± 0.03
NGC 3818	E5	E5	191	22.2	1701	0.20	8.8 ± 1.2	0.024 ± 0.003	0.25 ± 0.03
NGC 3962	E1	E1	225	35.2	1822	0.32	10.0 ± 1.2	0.024 ± 0.003	0.22 ± 0.03
NGC 4374	E1	E1	282	50.9	1060	3.99	9.8 ± 3.4	0.025 ± 0.010	0.24 ± 0.08
NGC 4552	S01(0)	E	264	29.3	322	2.97	6.0 ± 1.4	0.043 ± 0.012	0.21 ± 0.03
NGC 4636	E0/S01(6)	E0-1	209	88.5	937	1.33	13.5 ± 3.6	0.023 ± 0.006	0.29 ± 0.06
NGC 4696	(E3)	E+1 pec	254	85.0	2958	0.00	16.0 ± 4.5	0.014 ± 0.004	0.30 ± 0.10
NGC 4697	E6	E6	174	72.0	1241	0.60	10.0 ± 1.4	0.016 ± 0.002	0.14 ± 0.04
NGC 5011	E2	E1-2	249	23.8	3104	0.27	7.2 ± 1.9	0.025 ± 0.008	0.25 ± 0.06
NGC 5044	E0	E0	239	82.3	2704	0.38	14.2 ± 10.	0.015 ± 0.022	0.34 ± 0.17
NGC 5077	S01/2(4)	E3+	260	22.8	2764	0.23	15.0 ± 4.6	0.024 ± 0.007	0.18 ± 0.06
NGC 5090	E2	E2	269	62.4	3421		10.0 ± 1.7	0.028 ± 0.005	0.26 ± 0.04
NGC 5193	S01(0)	E pec	209	26.7	3711		6.8 ± 1.1	0.018 ± 0.002	0.26 ± 0.04
NGC 5266	S03(5) pec	SA0-:	199	76.7	3074	0.35	7.4 ± 1.4	0.019 ± 0.003	0.15 ± 0.05
NGC 5328	E4	E1:	303	22.2	4671		12.4 ± 3.7	0.027 ± 0.006	0.15 ± 0.05
NGC 5363	[S03(5)]	I0:	199	36.1	1138	0.28	12.1 ± 2.3	0.020 ± 0.004	0.16 ± 0.05
NGC 5638	E1	E1	168	28.0	1676	0.79	9.1 ± 2.3	0.024 ± 0.008	0.24 ± 0.05
NGC 5812	E0	E0	200	25.5	1930	0.19	8.5 ± 2.1	0.027 ± 0.008	0.22 ± 0.05
NGC 5813	E1	E1-2	239	57.2	1972	0.88	11.7 ± 1.6	0.018 ± 0.002	0.26 ± 0.04
NGC 5831	E4	E3	164	25.5	1656	0.83	8.8 ± 3.5	0.016 ± 0.011	0.21 ± 0.09
NGC 5846	S01(0)	E0+	250	62.7	1709	0.84	8.4 ± 1.3	0.033 ± 0.005	0.25 ± 0.03
NGC 5898	S02/3(0)	E0	220	22.2	2267	0.23	7.7 ± 1.3	0.030 ± 0.004	0.10 ± 0.03
NGC 6721	E1	E+:	262	21.7	4416		5.0 ± 0.8	0.040 ± 0.007	0.24 ± 0.02
NGC 6758	E2 (merger)	E+:	242	20.3	3404		16.0 ± 2.5	0.016 ± 0.002	0.32 ± 0.05
NGC 6776	E1 pec	E+pec	242	17.7	5480		2.7 ± 0.5	0.033 ± 0.010	0.21 ± 0.05
NGC 6868	E3/S02/3(3)	E2	277	33.7	2854	0.47	9.2 ± 1.8	0.033 ± 0.006	0.19 ± 0.03
NGC 6875	S0/a(merger)	SAB(s)0- pec:		11.7	3121				
NGC 6876	E3	E3	230	43.0	3836		9.8 ± 1.6	0.023 ± 0.003	0.26 ± 0.03
NGC 6958	R?S01(3)	E+	223	19.8	2652	0.12	3.0 ± 0.3	0.038 ± 0.006	0.20 ± 0.03
NGC 7007	S02/3/a	SA0-:	125	15.4	2954	0.14	3.4 ± 0.6	0.031 ± 0.010	0.15 ± 0.05
NGC 7079	SBa	SB(s)0	155	19.8	2670	0.19	6.7 ± 1.1	0.016 ± 0.003	0.21 ± 0.05
NGC 7097	E4	E5	224	18.1	2404	0.26	10.5 ± 2.4	0.024 ± 0.005	0.30 ± 0.05
NGC 7135	S01 pec	SA0- pec	231	31.4	2718	0.32	2.2 ± 0.4	0.047 ± 0.010	0.46 ± 0.04
NGC 7192	S02(0)	E+:	257	28.6	2904	0.28	5.7 ± 2.0	0.039 ± 0.015	0.09 ± 0.05
NGC 7332	S02/3(8)	S0 pec sp	136	14.7	1207	0.12	3.7 ± 0.4	0.019 ± 0.002	0.10 ± 0.03
NGC 7377	S02/3/Sa pec	SA(s)0+	145	36.9	3291		4.8 ± 0.6	0.020 ± 0.002	0.10 ± 0.03
IC 1459	E4	E	311	34.4	1659	0.28	8.0 ± 2.2	0.042 ± 0.009	0.25 ± 0.04
IC 2006	E1	E	122	28.6	1350	0.12	8.1 ± 0.9	0.026 ± 0.003	0.12 ± 0.02
IC 3370	E2 pec	E2+	202	38.6	2934	0.20	5.6 ± 0.9	0.022 ± 0.004	0.17 ± 0.04
IC 4296	E0	E	340	41.4	3762		5.2 ± 1.0	0.044 ± 0.008	0.25 ± 0.02
IC 5063	S03(3)pec/Sa	SA(s)0+:	160	26.7	3402				

RC3; Col. (6) gives the galaxy systemic velocity,  $V_{\text{hel}}$ , which is lower than  $\sim 5000 \text{ km s}^{-1}$ ; Col. (7) provides the richness parameter  $\rho_{xyz}$  (Tully 1988), which represents the density of galaxies brighter than apparent  $B$ -mag of  $-16$  in the vicinity of the entry, in galaxies  $\times \text{Mpc}^{-3}$ . Columns (8)–(10) list the age, metallicity, and  $[\alpha/\text{Fe}]$  ratios derived in Paper III.

The galaxies of the R05+A06 sample are mainly located in low density environments. The local density of the galaxies varies from  $\rho_{xyz} \approx 0.1 \text{ Mpc}^{-3}$ , typical of very isolated galaxies, to  $\rho_{xyz} \approx 4 \text{ Mpc}^{-3}$ , characteristic of denser regions in the Virgo cluster. For comparison, in the Tully (1988) catalogue objects such as NGC 1399 and NGC 1389, members of the Fornax cluster, have  $\rho_{xyz} = 1.59$  and  $1.50 \text{ Mpc}^{-3}$ , respectively. Thus, the R05+A06 sample, even though biased towards low density environments, contains a fraction of galaxies in relatively dense environments. The sample spans a wide range in central velocity dispersion, from  $\approx 115$  to  $340 \text{ km s}^{-1}$  (see Papers I and II for details).

Following the RC3 classification, the sample is composed of  $\sim 70\%$  ellipticals and  $\sim 30\%$  lenticulars. However, if we classify the galaxies according to their amount of rotation (see Appendix A), we end up with  $\sim 70\%$  fast rotators (F) and  $\sim 30\%$  slow rotators (S).

Intermediate resolution ( $FWHM \approx 7.6 \text{ \AA}$  at  $5550 \text{ \AA}$ ) spectra in the  $3700\text{--}7250 \text{ \AA}$  wavelength range were acquired with the  $1.5 \text{ m}$  ESO-La Silla telescope for the 65 galaxies of the sample. The spectra were extracted for 7 apertures of increasing radius ( $1.5''$ ,  $2.5''$ ,  $10''$ ,  $r_e/10$ ,  $r_e/8$ ,  $r_e/4$ , and  $r_e/2$ ), corrected for the galaxy ellipticity, and 4 adjacent annuli ( $r \leq r_e/16$ ,  $r_e/16 < r \leq r_e/8$ ,  $r_e/8 < r \leq r_e/4$ , and  $r_e/4 < r \leq r_e/2$ ). The data reduction and the computation of the Lick indices are described in Papers I and II. In Paper III, we derived ages, metallicities, and  $[\alpha/\text{Fe}]$  ratios by comparing the data with our new simple stellar population (SSP) models. No stellar population parameters are derived for IC 5063, since line emission is too strong to allow a measurement of the Lick indices. Summarizing the results of Paper III, we derive a large age spread, with SSP-equivalent ages ranging from a few Gyrs to a Hubble time. The galaxies have metallicities and  $[\alpha/\text{Fe}]$  ratios above solar. Both the total metallicity and the  $[\alpha/\text{Fe}]$  exhibit a positive correlation with the central velocity dispersion, indicating that the chemical enrichment was more efficient and the duration of the star formation shorter in more massive galaxies. We also find that the youngest objects in our sample are all located in the lowest density environments ( $\rho_{xyz} < 0.4 \text{ Mpc}^{-3}$ ). We suggest that the young galaxies in the lowest density environments underwent secondary episodes of star formation, which we call “rejuvenation episodes”. Within the individual galaxies, the stellar metallicity tends to decrease from the center outwards. We derive an average metallicity gradient of  $\Delta \log Z / \Delta \log(r/r_e) \sim -0.21$ .

### 3. Emission lines

#### 3.1. Starlight subtraction and measurement of line intensities

There are a number of emission lines that we expect to detect within the wavelength range  $3700\text{--}7250 \text{ \AA}$  sampled by our spectra: [OII]  $\lambda 3727$ , [NeIII]  $\lambda 3869$ , H $\beta$   $\lambda 4861$ , [OIII]  $\lambda \lambda 4959, 5007$ , [OI]  $\lambda 6300$ , H $\alpha$   $\lambda 6563$ , [NII]  $\lambda \lambda 6548, 6584$ , and [SII]  $\lambda \lambda 6717, 6731$ .

The emission line fluxes were measured in residual spectra obtained after subtracting the stellar population contribution from the observed galaxy spectra. The starlight subtraction is a

crucial step in correctly determining the emission line properties, in particular for H $\beta$  and H $\alpha$ , which are superimposed on the Balmer absorption features of the underlying stellar population. The H $\beta$  emission, which is much fainter than that of H $\alpha$  (FH $\beta \sim 1/3$  FH $\alpha$  in the absence of extinction), is the most difficult to measure. With only a few exceptions, we never see in our spectra a true emission feature in H $\beta$ , but rather an *infilling* of the stellar absorption line. It follows that a reliable measurement of this line rests on the appropriate modeling of the underlying starlight contribution.

To subtract the underlying stellar population from the galaxy spectra, we used new SSPs (Bressan, unpublished, see also Clemens et al. 2009; Chavez et al. 2009). The SSPs were computed from the isochrones of Padova 94 (Bertelli et al. 1994) with the revision of Bressan et al. (1998), including a new AGB mass-loss treatment calibrated on LMC cluster colors. These SSPs are particularly suited to our analysis because they use the MILES spectral library (Sánchez-Blázquez et al. 2006). MILES consists of  $2.3 \text{ \AA}$  FWHM optical spectra of  $\approx 1000$  stars spanning a large range of atmospheric parameters, and represents a substantial improvement over previous libraries used in population synthesis models.

For our study, we considered the galaxy spectra extracted in 4 concentric annuli ( $r \leq r_e/16$ ,  $r_e/16 < r \leq r_e/8$ ,  $r_e/8 < r \leq r_e/4$ , and  $r_e/4 < r \leq r_e/2$ ), as described in Sect. 2. The galaxy continua were fitted with the new SSPs, previously smoothed to match the instrumental resolution and the galaxy velocity dispersion, by means of a  $\chi^2$  criterion. In the fit, we considered selected spectral regions chosen to be particularly sensitive to either age or to metallicity. For each SSP of a given age and metallicity, and  $E(B - V)$  ranging from the Galactic foreground value to  $E(B - V)_{\text{MAX}} = 0.5$ , the  $\chi^2$  is

$$\chi^2 = \frac{1}{Nr} \sum_{i=1}^{Nr} \frac{1}{(N\lambda)_i} \sum_{j=1}^{(N\lambda)_i} \frac{(F_{\text{obs}}(\lambda_j) - F_{\text{SSP}}(\lambda_j) \times C_{\text{norm},i})^2}{(\sigma(\lambda_j))^2}, \quad (1)$$

where  $Nr$  is the number of selected spectral regions,  $(N\lambda)_i$  is the number of points in the  $i$ th region,  $F_{\text{obs}}(\lambda_j)$  is the observed galaxy flux at a given wavelength,  $F_{\text{SSP}}(\lambda_j) \times C_{\text{norm},i}$  is the SSP flux normalized to the observed flux in the  $i$ th region, and  $\sigma(\lambda_j)$  is the error in the observed flux. The  $Nr$  spectral regions have widths of between  $\approx 100 \text{ \AA}$  and  $\approx 300 \text{ \AA}$ . The normalization constant  $C_{\text{norm},i}$  is computed in a  $\approx 20 \text{ \AA}$  wide region adjacent to the  $i$ th band. This approach guarantees that the solution is mostly driven by the strengths of the absorption features, rather than by the global slope of the observed galaxy spectrum. This minimizes the effect of extinction and of the flux calibration on the solution. The spectral regions were selected to include both features particularly sensitive to age (the relative strength of the Ca II H + K lines, the  $4000 \text{ \AA}$  break ( $D_{4000}$ ), the H $\gamma$  and H $\delta$  lines), and features more sensitive to metallicity (the Fe lines at  $\lambda 4383, 4531, 5270, 5335$ , and the Mg absorption features around  $\lambda 5175$ ). The region around H $\beta$ , where emission is expected, was obviously excluded from the fit. On the other hand, negligible emission is expected in the higher-order Balmer lines (H $\gamma$ , H $\delta$ , and H $\epsilon$ , blended with the CaII H line at our resolution). The residual spectrum around each line is derived by normalizing the SSP in two continuum bands adjacent to the line of interest.

Because of the degeneracy between age, metallicity, and extinction, fits with similarly good  $\chi^2$  values can produce significantly different residual spectra, in particular around H $\beta$ . Thus, to obtain a statistically meaningful determination of the emission

lines, we considered all the  $N$  fits with  $\chi^2 < 2$ , and computed the emission lines in the corresponding residual spectra.

For each line, we adopted the average emission flux  $F_\mu$  computed as

$$F_\mu = \left( \sum_{\chi^2 < 2} e^{-\chi^2} \times F_{Z,t,A_V} \right) / \left( \sum_{\chi^2 < 2} e^{-\chi^2} \right), \quad (2)$$

where  $F_{Z,t,A_V}$  is the line flux obtained by subtracting the SSP of metallicity  $Z$ , age  $t$ , and reddening  $A_V$  to the observed galaxy spectrum, and  $e^{-\chi^2}$  is its weight. The line flux  $F_{Z,t,A_V}$  is determined by fitting the residual spectrum with Gaussian curves of variable width and intensity. The emission line width is treated as a free parameter because the velocity dispersion of the gas can be significantly different from that of the stars. More specifically, single Gaussians were used to fit all the lines, with the exceptions of [SII] $\lambda\lambda 6717, 31$ , which was fitted with a sum of 2 Gaussians, and the [NII] $\lambda\lambda 6548, 84 + H\alpha$  complex, which was fitted with a sum of 3 Gaussians. The [OII] $\lambda 3727$  feature is actually a doublet ( $\lambda\lambda 3726, 29$ ), but the two lines appear completely blended in our spectra.

The error in the average emission flux is

$$\sigma_\mu^2 = \left( \sum_{\chi^2 < 2} e^{-\chi^2} \times (F_{Z,t,A_V} - F_\mu)^2 \right) / \left( \sum_{\chi^2 < 2} e^{-\chi^2} \right). \quad (3)$$

This error takes into account the uncertainty caused by the intrinsic degeneracy of the stellar populations. Because of the high signal-to-noise ratio (S/N) of our spectra, this is actually the largest source of error in the measure of the emission fluxes.

The use of a single SSP in the fitting procedure may lead to spurious effects where recent star formation is present in some amounts. We showed in Paper III that some galaxies in our sample have very young luminosity-weighted ages ( $< 4$  Gyr), possibly as a consequence of “rejuvenation” episodes. Therefore, we repeated the fitting procedure using, instead of one SSP, a combination of a young ( $t < 8$  Gyr) and an old ( $t > 8$  Gyr) SSP. This approach guarantees a more reliable spectral subtraction from the Balmer lines for the “rejuvenated” galaxies. The two-SSP fitting procedure results in some differences for the galaxies with faint  $H\beta$  emission. This may be important when discriminating between LINERs and Seyfert through the [OIII]/ $H\beta$  ratio (see Sect. 4). On the other hand, we checked that there are no significant differences between the resulting emission lines for galaxies randomly selected among those without signs of recent star formation.

In Fig. 1, we show the stellar continuum subtraction procedure for two illustrative examples: IC 1459, with relatively strong emission lines, and NGC 5813, with weak emission lines. We note that in the figure the subtracted stellar continuum is an SSP of age, metallicity, and extinction equal to the average of all the  $N$  solution with  $\chi^2 < 2$ . This is slightly different from our procedure, where we have subtracted the individual solutions  $N$  times from the same galaxy spectrum, and have computed the final emission lines to be average of the  $N$  emission fluxes. In Fig. 1, the emission features are easily visible in IC 1459. The errors in the emission line fluxes introduced by the uncertainties in the stellar continuum subtraction are thus relatively small. In the case of NGC 5813, instead, the determination of the emissions is dominated by starlight subtraction effects, in particular for  $H\beta$  and  $H\alpha$ . The errors in the emission lines are consequently quite large.

We provide in Table 2 the emission line fluxes in units of  $10^{-16}$  erg s $^{-1}$  cm $^{-2}$  arcsec $^{-2}$  derived for the R05+A06 sample

in 4 annuli of increasing galactocentric distance ( $r \leq r_e/16$ ,  $r_e/16 < r \leq r_e/8$ ,  $r_e/8 < r \leq r_e/4$ , and  $r_e/4 < r \leq r_e/2$ ). In Table 3, we provide the equivalent width (EW) of each line, derived as  $F_\mu/F_{\text{cont}}$ , where  $F_{\text{cont}}$  is the flux computed in a continuum band adjacent to the line of interest. The large errors in  $H\beta$  are due to its intrinsic faintness, accompanied by a strong dependence of the  $H\beta$  absorption line on age. The values given in Tables 2 and 3 are not corrected for reddening. The extinction-corrected emissions can be easily derived from the  $E(B - V)$  values given in Col. 3 of Table 2, and computed as described in the next paragraph.

### 3.2. Extinction

The extinction in the lines was derived from the relative observed strengths of the Balmer lines. The intrinsic flux ratio  $(FH\alpha/FH\beta)_0$  is  $\approx 2.85$  for HII regions and  $\approx 3.1$  for AGN-like objects (Osterbrock 1989). Values larger than these are due to absorption from an intervening medium.

More specifically, given an observed  $FH\alpha/FH\beta$  ratio, the reddening is computed to be

$$E(B - V) = \frac{\log_{10} [(FH\alpha/FH\beta)/(FH\alpha/FH\beta)_0]}{0.4 \times R_V \times (A_{H\beta}/A_V - A_{H\alpha}/A_V)}, \quad (4)$$

where  $A_\lambda$  is the magnitude attenuation at a given wavelength, and  $A_{H\beta}/A_V$ ,  $A_{H\alpha}/A_V$ , and  $R_V = A_V/E(B - V)$ , depend on the adopted extinction curve. We adopted the Cardelli et al. (1989) extinction law, where  $R_V = 3.05$ . We also assumed  $(FH\alpha/FH\beta)_0 = 3.1$ , since all the galaxies in the R05+A06 sample display AGN-like emission-line ratios (see Sect. 4). The assumption of  $(FH\alpha/FH\beta)_0 = 2.85$  does not significantly change our results.

In Fig. 2, we plot the  $H\alpha$  versus  $H\beta$  fluxes derived in a central  $r \leq r_e/16$  region. The majority of the galaxies have  $E(B - V) < 0.3$ . Some galaxies exhibit instead very strong extinction, as high as  $E(B - V) \approx 1.5$  or even more. They have very faint  $H\beta$  intensities, accompanied by relatively strong  $H\alpha$  emission. Vice versa, a few objects fall below the  $E(B - V) = 0$  line, in the region of “negative reddening”. In these cases, the emission derived in  $H\beta$  is incompatible (too large) with the derived  $H\alpha$ . An obvious explanation is that the underlying continuum was not subtracted properly. More specifically, that we underestimate the  $H\alpha/H\beta$  ratio suggests that we have subtracted populations that are systematically too young or too metal poor. To verify this hypothesis, we simulated the situation in which a too-young population is subtracted from the galaxy spectrum in the following way. We created a synthetic spectrum by adding  $H\beta$  and  $H\alpha$  emission lines (in the ratio  $FH\alpha = 3.1FH\beta$ ) to an old SSP. We then rederived the emission intensities by subtracting from the synthetic spectrum increasingly younger SSPs. We found that the  $FH\alpha/FH\beta$  ratio decreases as the  $\Delta$  age increases. The effect is much stronger when the initial emission intensities are weaker, because of a combination of the stronger dependence of the  $H\beta$  absorption line on age, and of the intrinsic faintness of the  $H\beta$  emission line relative to  $H\alpha$ .

Finally, there are some galaxies whose  $H\beta$  and  $H\alpha$  emissions are both consistent with zero within a  $3\sigma$  errorbar (NGC 1366, NGC 1389, NGC 1407, NGC 1426, NGC 5638, NGC 5812, and NGC 5831). These galaxies also exhibit no emission in the other lines, and are classified as *no emission* (N) galaxies.

The derived  $E(B - V)$  values at different galactocentric distances are given in Col. 3 of Table 2. For the galaxies with “negative reddening”, and galaxies with  $E(B - V)$  lower than

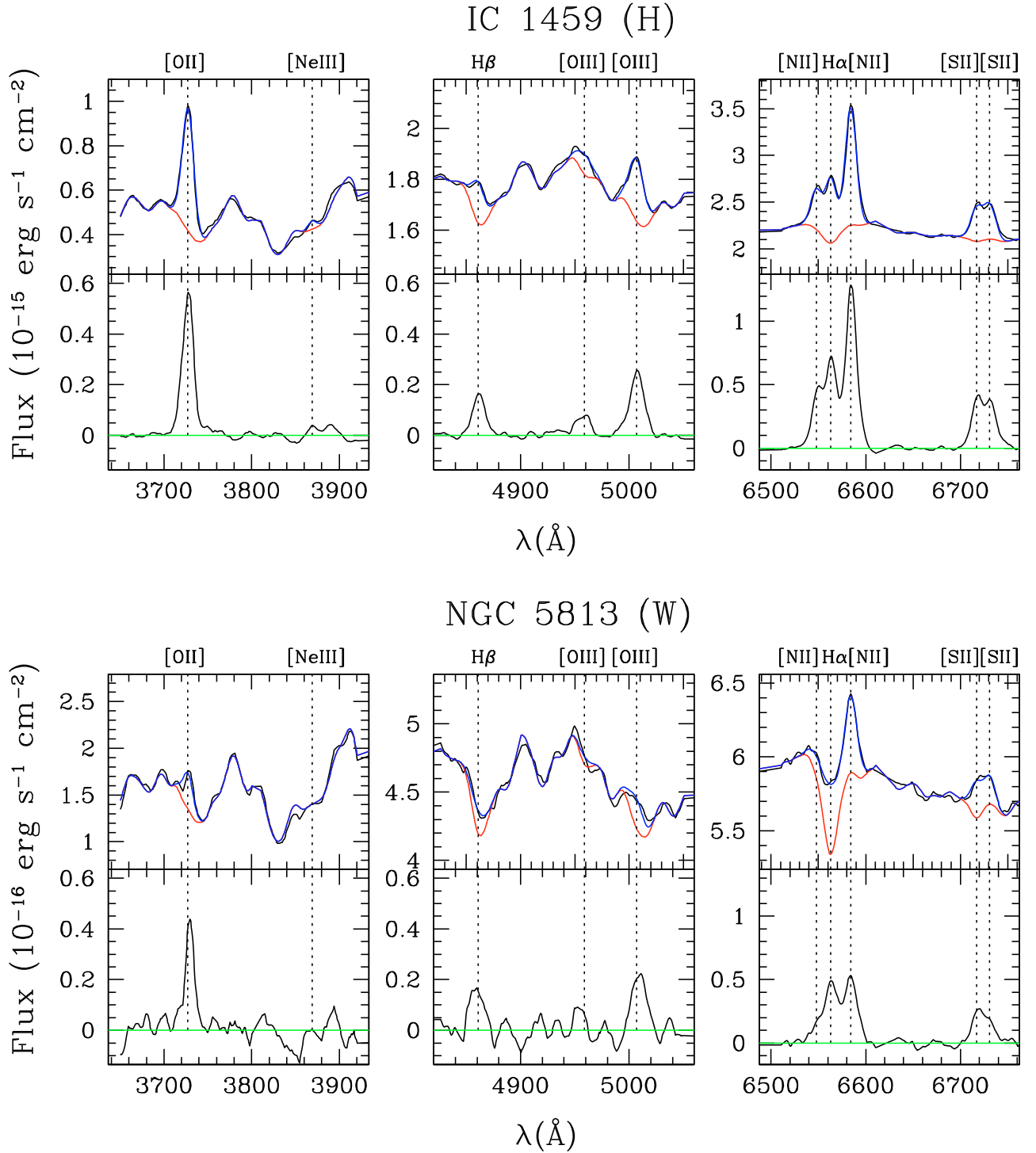


**Fig. 1.** Central ( $r \leq r_e/16$ ) spectra for a high emission galaxy (IC 1459) and a weak emission galaxy (NGC 5813) in the wavelength ranges where the most important emission lines are measured. For each galaxy, we show in the top panels the observed spectrum (black line), the underlying stellar spectrum model (red), and the fit to the observed spectrum obtained by adding emission lines (Gaussian curves) to the underlying stellar continuum (blue). In the bottom panels, we show the subtracted spectrum, where the emission lines emerge. Note that in this figure the subtracted stellar continuum is an SSP of age,  $Z$ , and extinction equal to the average of all the solution with  $\chi^2 < 2$ . However, this is only for illustration purposes, and is slightly different from the procedure described in Sect. 3.1.

the Galactic foreground extinction, the  $E(B - V)$  was set to the foreground value. Very large  $E(B - V)$  values are derived for NGC 777, NGC 1521, NGC 3136, NGC 3557, NGC 6776, NGC 7007, and NGC 3489. These strong extinction values, not observed in the continuum, suggest that the distribution of the dust is patchy. We note however that the errors in the derived

$E(B - V)$  values are quite large, due to the large uncertainty in the  $H\beta$  emission. The reddening distributions for the E and S0 classes are shown in Fig. 3. The median  $E(B - V)$  values for the two classes are 0.11 and 0.26, respectively. However, a Mann-Whitney U test shows that there is no significant difference between the two distributions.

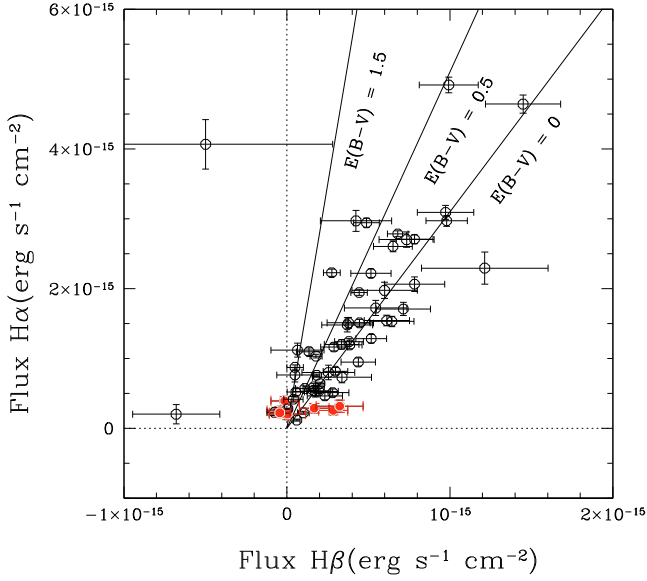


**Fig. 2.**  $H\alpha$  versus  $H\beta$  emission fluxes for the galaxy sample measured in a central  $r \leq r_e/16$  region. IC 5063, with derived emission fluxes falling outside the plot boundaries, is not included. Full dots denote the seven “no emission” galaxies (NGC 5638, NGC 5831, NGC 1407, NGC 1366, NGC 1426, NGC 5812, and NGC 1389) in the sample. The solid lines indicate regions of different reddening.

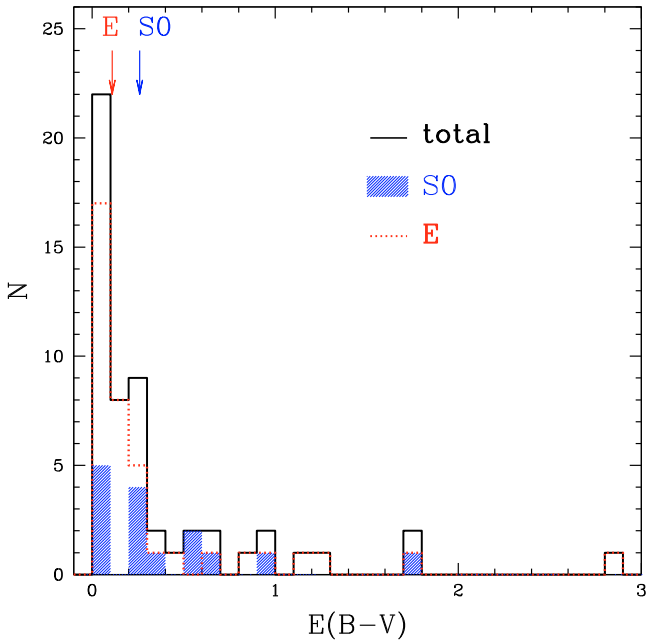


**Fig. 3.**  $E(B - V)$  distribution derived for our sample from the  $F_{H\alpha}/F_{H\beta}$  ratios. The shaded histogram denotes S0 galaxies, while the dotted line is for E galaxies. Vertical arrows indicate the median values.

After computing the  $E(B - V)$  values, we corrected the observed emission fluxes to be

$$F_{\text{corr}} = F_{\text{obs}} \times 10^{0.4 \times A}, \quad (5)$$

where

$$A = \left( \frac{A_\lambda}{A_V} \right) \times 3.05 \times E(B - V), \quad (6)$$

$\left( \frac{A_\lambda}{A_V} \right)$  is taken from the extinction curve, and  $\lambda$  is the wavelength of the line of interest.

### 3.3. Results

The galaxies are classified in Table 4 according to the intensity of their nuclear emission lines. We identify three categories: no emission galaxies (N), where no emission lines are detected within a  $3\sigma$  error; weak emission-line galaxies (W), with  $\text{EW}(H\alpha + [\text{NII}]6584) < 3 \text{ \AA}$ ; and strong emission-line galaxies (H), with  $\text{EW}(H\alpha + [\text{NII}]6584) > 3 \text{ \AA}$ .

Emission lines are detected in 58 of 65 galaxies ( $\sim 89\%$  of the sample), while strong emission is present in 57% of the sample. In the central  $r \leq r_e/16$  region, we derive median EWs of  $\approx 0.51$ , 0.72, 1.4, and 1.8 for  $H\beta$ ,  $[\text{OIII}]\lambda 5007$ ,  $H\alpha$ , and  $[\text{NII}]\lambda 6584$ , respectively. For the same lines, the median percentage errors amount to  $\approx 31\%$ , 11%, 6%, and 1%.

We investigated possible differences in the emission intensity between the E and S0 subsamples, and between the fast (F) and slow (S) rotators subsamples. The distributions and the relative median values are shown in Fig. 4. An appreciable difference is observed only between F and S for the median  $[\text{NII}]$  value. However, Mann-Whitney U tests provide  $P \geq 0.05$  (for a two-tailed test) for all the distributions, indicating that there is no significant difference between the E, S0, F, and S subsamples.

To quantify the importance of the emission with respect to the underlying stellar continuum at increasing galactocentric distance, we studied the behavior of the  $[\text{NII}]\lambda 6584$  and the  $H\alpha$  lines in the 4 annuli defined in Sect. 2. We note that the use of adjacent annuli instead of “apertures” allows us to isolate the true emission contribution from different regions within the galaxy. The  $[\text{NII}]\lambda 6584$  line is stronger than the other lines, and thus more easily measured also in the external annuli. Furthermore, it is also very poorly affected by uncertainties in the underlying stellar population subtraction, and has the lowest percentage error. On the other hand, the  $H\alpha$  line has the advantage that, being a recombination line, it directly reflects the ionizing photon flux, but its measure is far more affected than the  $[\text{NII}]$  by uncertainties in the underlying population subtraction. The behaviors of the observed  $[\text{NII}]/([\text{NII}] \leq r_e/16)$  and  $H\alpha/(H\alpha \leq r_e/16)$  ratios with increasing galactocentric distances are shown in Fig. 5. Negative values are consistent with no emission. The plotted values were not corrected for reddening, but extinction may affect the EWs if the nebular emission were more reddened than the continuum. Tran et al. (2001) indeed showed that the presence of emission lines in ETGs tends to be associated with the presence of clumpy dust.

Figure 5 shows that, with some exceptions (NGC 3489, NGC 5898, NGC 7007, NGC 7079, NGC 7192, NGC 7377), the emission EWs tend to decrease from the center outwards. The average decrease in the  $[\text{NII}]$  EW is  $\approx 0.7$ , 0.5, and 0.4 of the central value at  $\sim 0.1 r_e$ ,  $\sim 0.2 r_e$ , and  $\sim 0.4 r_e$ , while the  $H\alpha$  EW decreases more gently ( $\sim 0.8$ , 0.7, and 0.6 at the same radii). The steeper decrease in the  $[\text{NII}]$  relative to the  $H\alpha$  is indicative of a progressive softening of the ionizing spectrum from the galaxy center to more external regions. The decrease in the  $H\alpha$  EW implies that the ionizing flux decrease more rapidly than the stellar continuum around  $\sim 6500 \text{ \AA}$ . However, given the uncertainties, we can consider significant only the decrease from the center to  $\sim 0.1 r_e$ . Deeper observations are needed to trace with higher confidence the EW behavior out to larger radii.

The galaxies NGC 7079, NGC 3489, NGC 7007, NGC 7192, NGC 7377, and NGC 5898 deviate from the average decreasing trend, exhibiting flat or increasing emission EWs (although the  $H\alpha$  of NGC 3489, NGC 5898, and NGC 7079 drops in the most external annulus). NGC 3489 and NGC 7007 have large reddening, thus their increasing trend may be caused by stronger

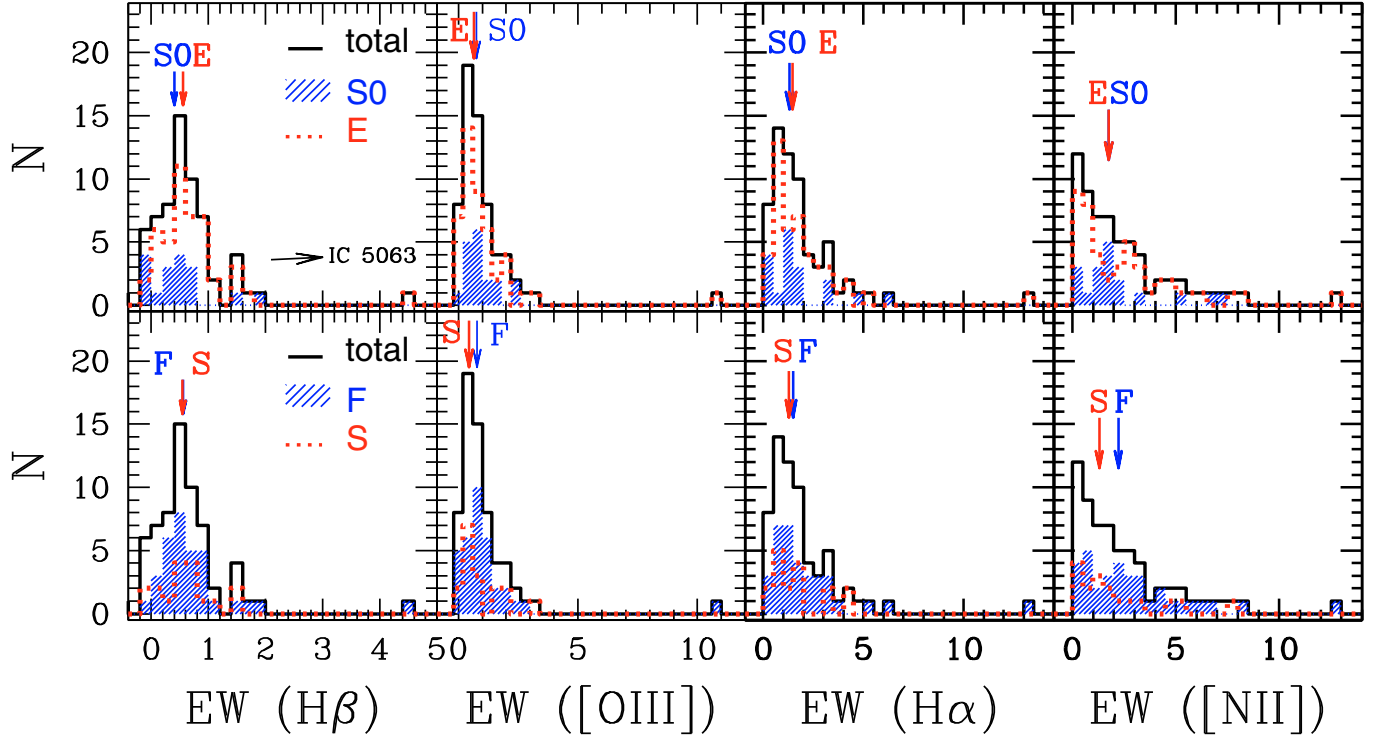


**Fig. 4.**  $H\beta$ ,  $[OIII]\lambda 5007$ ,  $H\alpha$  and  $[NII]\lambda 6584$  EW distributions at  $r \leq r_e/16$  for the total galaxy sample, for the S0 and E subsamples, and for the fast (F) and slow (S) rotators subsamples. IC 5063, with  $EW(H\beta) \sim 15$ ,  $EW([OIII]) \sim 122$ ,  $EW(H\alpha) \sim 58$ , and  $EW([NII]) \sim 38$ , falls outside the plot boundaries. The EWs are not corrected for extinction. The vertical arrows indicate the median values for the E, S0, F, and S subsamples.

extinction toward the galaxy center. Unfortunately, the errors in the derived  $E(B - V)$  values are large, and it is difficult to establish from our data if indeed the reddening decreases with galacto-centric distance. On the other hand, the other galaxies (NGC 7079, NGC 7192, NGC 7377, and NGC 5898) show very little or almost null extinction, thus the observed trends are likely to be intrinsic.

## 4. Spectral classification

### 4.1. Diagnostic diagrams

Galaxies were classified by means of the standard  $[OIII]\lambda 5007/H\beta$  versus  $[NII]\lambda 6584/H\alpha$  diagnostic diagram (Baldwin, Phillips and Terlevich (1981; hereafter BPT). Using a combination of stellar population synthesis models and photoionization models, Kewley et al. (2001) identified a “maximum starburst line” in the BPT diagram. Galaxies lying above this line are likely to be dominated by an AGN. Kauffmann et al. (2003) later revised the Kewley et al. (2001) classification scheme introducing an empirical line to divide pure star-forming galaxies from AGN-HII composite objects (also called “transition objects”), which may have a significant contribution from both AGN and star formation (see also Stasińska et al. 2006). The optical spectra of composite objects may be produced by either 1) a combination of star formation and a Seyfert nucleus, or 2) a combination of star formation and LINER emission (Kewley et al. 2006).

From the distribution in the BPT diagram of the galaxies from the Sloan Digital Sky Survey, Kewley et al. (2006) introduced an empirical horizontal line to separate “Seyfert” and LINERs. Even though LINERs exhibit  $[NII]/H\alpha$  ratios higher than the star-forming galaxies, indicating a harder ionization

continuum, it remains debated whether they are powered by active galactic nuclei or not (see Sect. 1).

The BPT diagram for the R05+A06 sample is shown in Fig. 6. The  $[NII]\lambda 6584/H\alpha$  line ratio was preferred to the  $[SII](\lambda 6717 + \lambda 6731)/H\alpha$  and  $[OI]\lambda 6300/H\alpha$  ratios because of the larger signal-to-noise ratio of the  $[NII]$  line in our spectra. Emission-line ratios were corrected for extinction adopting the  $E(B - V)$  values derived in Sect. 3.2 and reported in Col. 3 of Table 2, even though the BPT diagram is almost insensitive to reddening. The galaxies with negative reddening, or reddening lower than the foreground value, were corrected by adopting the Galactic foreground reddening from NED.

According to their nuclear ( $r < r_e/16$ ) emission, the majority of our galaxies are classified as LINERs. A few galaxies (NGC 3258, NGC 4552, NGC 5193, NGC 5328, NGC 6721, NGC 6876, and IC 2006) fall in the region of “composites”, and possibly contain a combined contribution from both star formation and AGN. The galaxies IC 5063, NGC 777, NGC 3489, NGC 7007, and NGC 6958, fall in the Seyfert region. Among them, only IC 5063 can be classified as a bona fide Seyfert galaxy. The others all have very large uncertainties in their  $[OIII]/H\beta$  ratios, due to their low  $H\beta$  emission (nuclear  $EW < 0.3 \text{ \AA}$ ), and are consistent with a LINER classification within the errors. These galaxies also exhibit very large reddenings ( $E(B - V) \gtrsim 1$ ). In contrast, NGC 3136 and NGC 6776 are LINERs, but are consistent with being Seyferts within the errors. Among the Seyferts, a spectral classification is provided in the literature only for NGC 3489 (Ho et al. 1997b; Sarzi et al. 2006), NGC 777 (Ho et al. 1997b), and NGC 6958 (Saraiva et al. 2001). These studies classify the first two galaxies as Seyferts, and the last one as LINER.

The final spectral classification obtained from the nuclear ( $r \leq r_e/16$ ) lines is given in Col. 3 of Table 4.

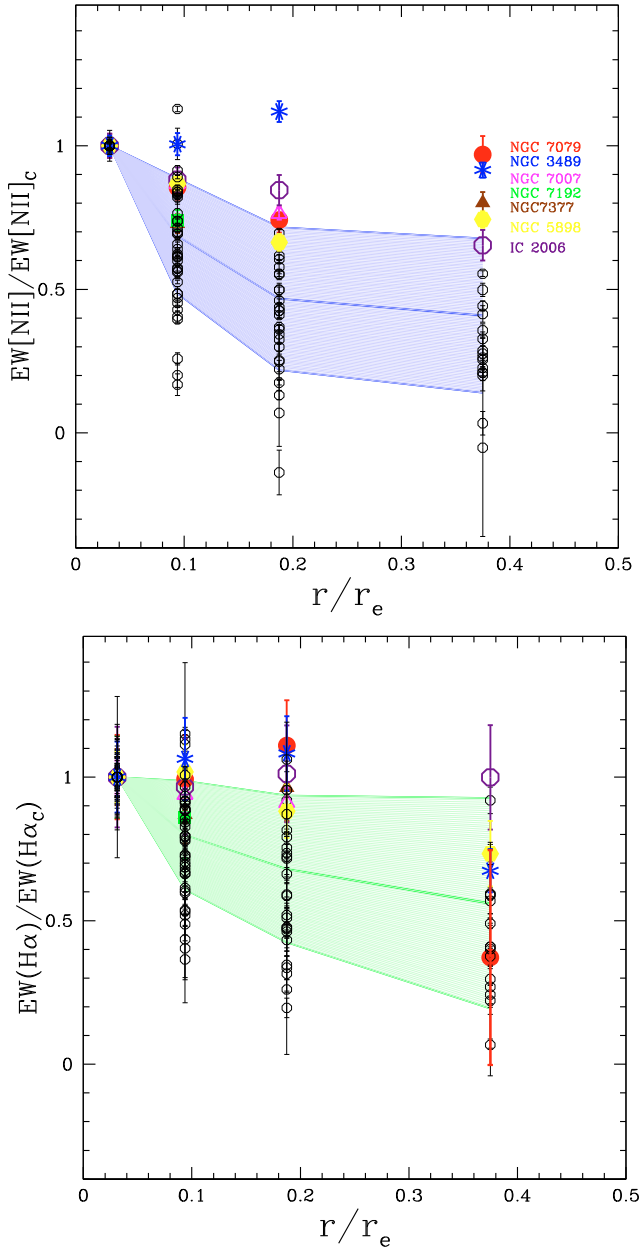


**Fig. 5.** Emission EW derived in annuli of increasing galactocentric distance ( $r \leq r_e/16$ ,  $r_e/16 < r \leq r_e/8$ ,  $r_e/8 < r \leq r_e/4$ , and  $r_e/4 < r \leq r_e/2$ ) over the central value ( $r \leq r_e/16$ ) as a function of  $r/r_e$ . The top and bottom panels refer to the [NII] 6584 Å and H $\alpha$  lines, respectively. The shaded regions indicate the average trends and the  $\pm 1\sigma$  levels. Only galaxies classified as H or W in Table 4 were included. Galaxies with flat or increasing emission trends were labeled.

#### 4.2. Gradients

We investigated how the distribution of the galaxies in the BPT diagram changes at annuli of increasing galactocentric distance ( $r \leq r_e/16$ ,  $r_e/16 < r \leq r_e/8$ ,  $r_e/8 < r \leq r_e/4$ , and  $r_e/4 < r \leq r_e/2$ ). This emerges by comparing the four panels of Fig. 6. Only a few galaxies have sufficiently high S/N ratios that allow us to measure the emission line ratios in the most external annuli.

The clear result is that, from the center outwards, the bulk of the galaxies moves left and down in the BPT diagram. An increasing number of galaxies move from being LINERs to “composite” objects as the emission lines are measured at larger galactocentric distances. This effect would probably not have

been observed by considering apertures instead of annuli, since the central emission almost always predominates. The effect is more accurately quantified in Fig. 7, where we plot the distribution of the [NII]/H $\alpha$  and [OIII]/H $\beta$  ratios over the central  $r \leq r_e/16$  values (C) for the different annuli. The peak of the  $([NII]/H\alpha)/([NII]/H\alpha)_C$  distribution moves from 1 to values  $< 1$  at larger radii. The average  $([NII]/H\alpha)/([NII]/H\alpha)_C$  values are  $\approx 0.85$ ,  $0.73$ , and  $0.69$  at  $r_e/16 < r \leq r_e/8$ ,  $r_e/8 < r \leq r_e/4$ , and  $r_e/4 < r \leq r_e/2$ , respectively. These correspond to horizontal shifts of  $\approx -0.07$ ,  $-0.14$ , and  $-0.16$  dex in the BPT diagram. However, given the large errors in the emission-line measures in the most external annulus, we consider this result significant only out to  $r \leq r_e/4$ . The  $([OIII]/H\beta)/([OIII]/H\beta)_C$  distribution is less peaked, in part also because of the large errors in the derived [OIII]/H $\beta$  ratios. The average values are  $0.92$ ,  $0.77$ , and  $0.64$ , for the three annuli, corresponding to vertical shifts of  $\approx -0.04$ ,  $-0.11$ , and  $-0.19$  dex in the BPT diagram. However, given the intrinsic faintness and large errors of the [OIII] and H $\beta$  lines compared to [NII] and H $\alpha$ , none of our conclusions will be based on the spatial behavior of the [OIII]/H $\beta$  ratio.

When the galaxies are inspected individually, we see that for the majority of them the [NII]/H $\alpha$  ratio decreases monotonically with galactocentric distance. The only exceptions are: IC 5063, NGC 1521, NGC 3136, NGC 3489, NGC 5813, NGC 5898, NGC 6721, NGC 6876, NGC 7135, and NGC 7192. In all these galaxies, the [NII]/H $\alpha$  ratio does not exhibit a clear trend. In NGC 3489, the ratio increases from the center outwards. The [NII]/H $\alpha$  ratio decreases very steeply in IC 1459, IC 4296, NGC 3607, NGC 4374, NGC 4697, NGC 5090, and NGC 5266. We show in Fig. 8 the individual BPT diagrams in different annuli for some galaxies of the sample. The [NII]/H $\alpha$  and [OIII]/H $\beta$  ratios in the four annuli for the whole sample are shown in Appendix B.

*Summarizing, the hardness of the ionizing continuum decreases with galactocentric distance.*

#### 4.3. Central correlations with galaxy properties

We investigated possible correlations between the emission-line properties and the galaxy properties. Our results are summarized in Fig. 9.

In the top panels of Fig. 9, we plotted the central ( $r < r_e/16$ ) H $\alpha$  and [NII] $\lambda$ 6584 equivalent widths versus the central velocity dispersion  $\sigma_c$ , the age, the metallicity, and the  $\alpha$ /Fe enhancement. The H $\alpha$  and [NII] EWs quantify the strength of the emission with respect to the stellar continuum. However, the [NII] line is much less affected than the H $\alpha$  by uncertainties or systematics caused by the stellar continuum subtraction. The scatter in both the H $\alpha$  and [NII] EW increases with  $\sigma_c$ . This remains true if the [OIII] emission is considered. If we exclude the Seyfert galaxy IC 5063, strong emission is observed only for galaxies with  $\sigma_c \gtrsim 200$  km s $^{-1}$ . The galaxies with the strongest emission tend to be fast rotators. All the low  $\sigma_c$  galaxies are also fast rotators. For the stellar population parameters, the trend is preserved only for the [NII] line versus the  $[\alpha/Fe]$  ratio (it is barely present in the H $\alpha$  versus  $[\alpha/Fe]$  plane). We note that this trend could be driven by the contamination of the Mg $b$  index by the [NI] $\lambda$ 5199 line, which causes larger  $[\alpha/Fe]$  values for galaxies with stronger emission (Goudfrooij & Emsellem 1996). The lack of a trend between the EW and metallicity is rather surprising in the light of the well known metallicity- $\sigma$  relation for ETGs.

In the third row panels of Fig. 9, we show the central ( $r < r_e/16$ ) [NII] $\lambda$ 6584/H $\alpha$  ratio, which is a measure of the hardness



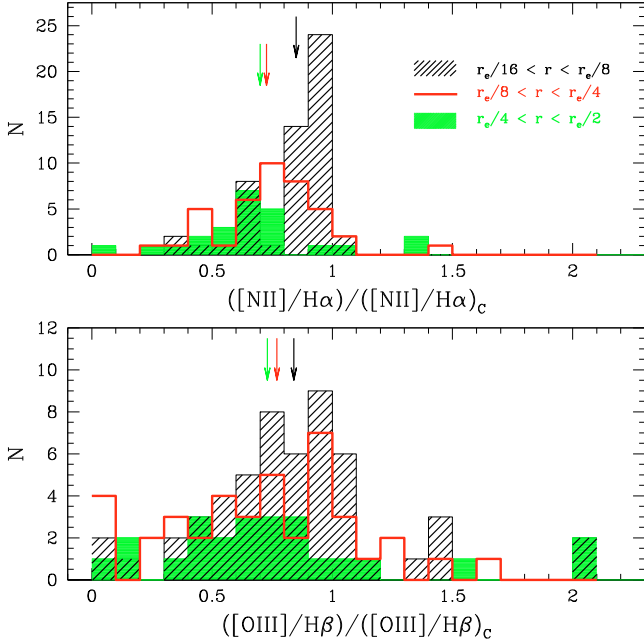


**Fig. 7.** Distribution of emission line ratios over the central  $r \leq r_e/16$  value for the galaxies in the four BPT diagrams of Fig. 6. The dashed, empty, and full histograms correspond, respectively, to the  $r_e/16 < r \leq r_e/8$ ,  $r_e/8 < r \leq r_e/4$ , and  $r_e/4 < r \leq r_e/2$  annuli. Vertical arrows indicate the average values. From the galaxy center outwards, the average  $[\text{NII}]/\text{H}\alpha / [\text{NII}]/\text{H}\alpha_c$  ratios drop to 0.85, 0.73, and 0.69 in the three annuli, respectively. For the same annuli, we derive average  $[\text{OIII}]/\text{H}\beta / [\text{OIII}]/\text{H}\beta_c$  values of 0.92, 0.77, and 0.64.

ages younger than  $\sim 4$  Gyr. “Composite” galaxies have ages older than 5 Gyr. LINERs cover the whole age range from a few Gyrs to a Hubble time. For the three classes, the average ages are 3.8, 7.5, and 9 Gyr, respectively. The average metallicities are  $\log Z/Z_\odot \sim 0.39, 0.29,$  and  $0.22$ , respectively. No significant difference is observed in the  $[\alpha/\text{Fe}]$  ratio.

It emerges that Seyferts tend to have luminosity-weighted ages significantly younger than LINERs, probably because of recent star formation episodes. The only caveat in this statement is that the only bona fide Seyfert in our sample (IC 5063), does not have an age determination.

## 5. Oxygen abundance

When the ionizing source is known, one can derive the element abundance of the warm gas. In their nuclear ( $r < r_e/16$ ) region, the majority of the galaxies in our sample are classified as LINERs, a few are classified as “composites”, and only IC 5063 is classified as a bona fide Seyfert galaxy. We also noticed a progressive increase in the fraction of “composites” with respect to pure LINERs moving from the galaxy center to more external regions. As discussed in Sect. 1, the ionizing mechanism in LINERs/composites is still far from being understood. For this reason, we derived the oxygen metallicity for the R05+A06 sample in the two extreme assumptions of 1) photoionization by hot stars; and 2) AGN excitation. A calibration in the case of shock heating is not provided in the literature.

### 5.1. HII region calibration

In HII regions, the oxygen metallicity is determined by means of the standard  $R_{23} = ([\text{OII}]\lambda 3727 + [\text{OIII}]\lambda 4959, 5007)/\text{H}\beta$

**Table 4.** Classification from optical lines in the nuclear ( $r \leq r_e/16$ ) region.

Galaxy Id	Emission type <sup>a</sup>	Activity Class <sup>b</sup>
NGC 128	H	LINER
NGC 777	W	Sy/ LINER
NGC 1052	H	LINER
NGC 1209	H	LINER
NGC 1297	H	LINER
NGC 1366	N	
NGC 1380	H	LINER
NGC 1389	N	
NGC 1407	N	
NGC 1426	N	
NGC 1453	H	LINER
NGC 1521	W	LINER
NGC 1533	H	LINER
NGC 1553	W	LINER
NGC 1947	H	LINER
NGC 2749	H	LINER
NGC 2911	H	LINER
NGC 2962	H	
NGC 2974	H	LINER
NGC 3136	H	LINER/ Sy
NGC 3258	H	Comp
NGC 3268	H	LINER
NGC 3489	H	Sy/ LINER
NGC 3557	W	LINER
NGC 3607	H	LINER
NGC 3818	Traces	
NGC 3962	H	LINER
NGC 4374	H	LINER
NGC 4552	W	Comp
NGC 4636	H	LINER
NGC 4696	H	LINER
NGC 4697	W	LINER
NGC 5011	W	LINER
NGC 5044	H	LINER
NGC 5077	H	LINER
NGC 5090	H	LINER
NGC 5193	W	Comp
NGC 5266	H	LINER
NGC 5328	W/Traces	Comp
NGC 5363	H	LINER
NGC 5638	N	
NGC 5812	N	
NGC 5813	W	LINER
NGC 5831	N	
NGC 5846	H	LINER
NGC 5898	W	LINER
NGC 6721	W/Traces	Comp
NGC 6758	H	LINER
NGC 6776	H	LINER/ Sy
NGC 6868	H	LINER
NGC 6875	W	
NGC 6876	W /Traces	Comp
NGC 6958	H	Sy/ LINER
NGC 7007	W	Sy/ LINER
NGC 7079	W	LINER
NGC 7097	H	LINER
NGC 7135	H	LINER
NGC 7192	W	LINER
NGC 7332	W/Traces	
NGC 7377	W	LINER
IC 1459	H	LINER
IC 2006	W	Comp
IC 3370	H	LINER
IC 4296	H	LINER
IC 5063	H	Sy

**Notes.** <sup>(a)</sup> N = no emission; W = weak emission ( $EW(\text{H}\alpha + [\text{NII}]6584) < 3 \text{ \AA}$ ); H = high emission ( $EW(\text{H}\alpha + [\text{NII}]6584) > 3 \text{ \AA}$ ). <sup>(b)</sup> At larger radii, some LINERs are classified as composites.

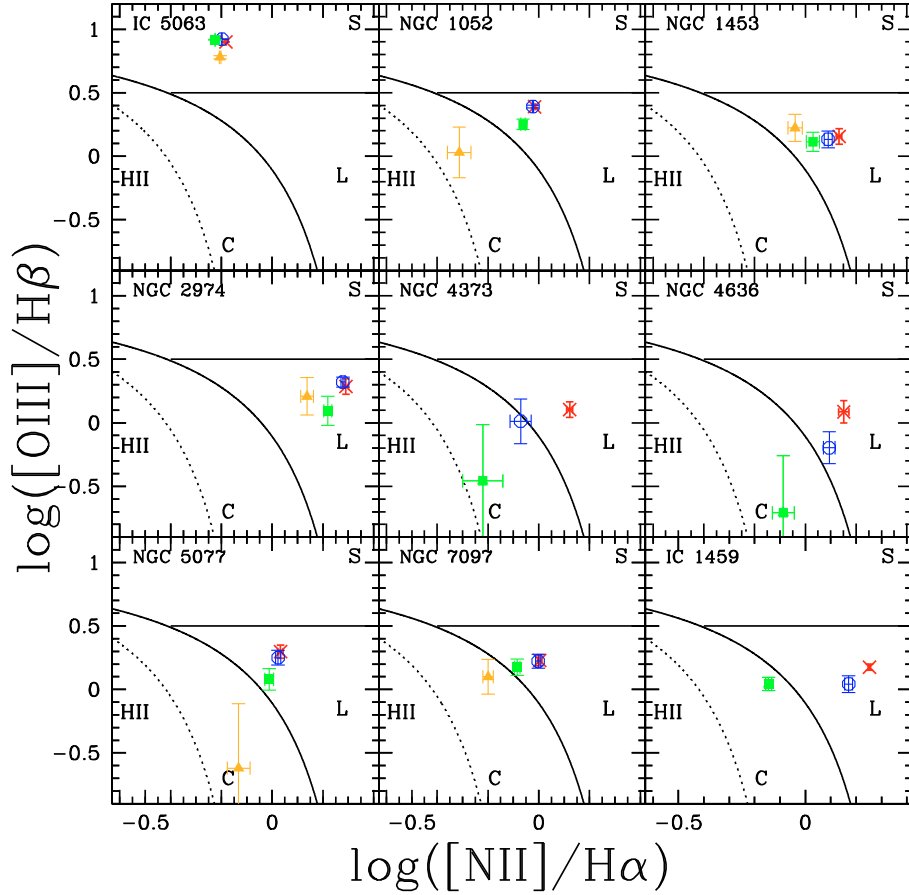


**Fig. 8.** BPT diagrams of some galaxies representing the general trends of the whole sample in the four annuli:  $r \leq r_e/16$  (red cross),  $r_e/16 < r \leq r_e/8$  (blue open circle),  $r_e/8 < r \leq r_e/4$  (green full square), and  $r_e/4 < r \leq r_e/2$  (yellow full triangle). Note that while the error in  $[\text{OIII}]/\text{H}\beta$  is large, the error in  $[\text{NII}]/\text{H}\alpha$  is significantly smaller.

parametrization, first introduced by Pagel et al. (1979), and then revised by other authors (Edmund & Pagel 1984; McCall et al. 1985; Dopita & Evans 1986; McGaugh 1991; Zaritsky et al. 1994). The main problem with this calibration is that the relationship between  $R_{23}$  and the oxygen abundance is double valued, requiring some a priori knowledge of a galaxy’s metallicity to determine its correct location in the upper or lower branch of the curve. A good discriminator is the  $[\text{OIII}]\lambda 5007/[\text{NII}]\lambda 6584$  ratio, which is usually less than  $\approx 100$  for galaxies with  $12 + \log(\text{O}/\text{H}) > 8.3$ , on the metal-rich branch (Edmunds & Pagel 1984; Kobulnicky et al. 1999). The various calibrations, based on different photoionization models and HII region data, show a dispersion of  $\sim 0.2$  dex in the metal-rich branch. Kobulnicky et al. (1999) report analytic expressions based on a set of photoionization models that fit the empirical calibrations within less than 0.05 dex, and that include the effect of the ionization parameter through  $\text{O}_{32} = [\text{OIII}]\lambda 4959, 5007/[\text{OII}]\lambda 3727$ .

We computed the oxygen abundance for our sample adopting the calibration in Kobulnicky et al. (1999, hereafter Kob99). Because of the lack of star-forming regions in ETGs, this calibration is valid if: 1) the gas is photoionized by hot old stars, probably PAGB stars; and 2) the calibration is still valid even though PAGB stars have different spectral shapes than high-mass main sequence stars. The same approach was adopted by Athey & Bregman (2009) to determine oxygen abundances in a sample of 7 ETGs. We computed the  $R_{23}$  and  $\text{O}_{32}$  values using the emission line fluxes in Table 2, and correcting for reddening using the values in Col 3 of Table 2. The derived oxygen metallicities

at  $r \leq r_e/16$  are given in Col. 2 of Table 6. The errors were computed by combining the intrinsic uncertainty in the calibration ( $\sim 0.15$  dex, see Kob99), with the uncertainty in the emission line fluxes. We could not determine the oxygen abundance in 13 galaxies, namely IC 5063, NGC 777, NGC 1297, NGC 1521, NGC 1947, NGC 2749, NGC 3136, NGC 3489, NGC 3557, NGC 5011, NGC 6776, NGC 6958, and NGC 7007, since  $R_{23}$  is larger than 10, and falls outside the valid calibration range for HII regions.

There are 6 galaxies in common with the sample of Athey and Bregman (2009): NGC 3489, NGC 3607, NGC 4374, NGC 4636, NGC 5044, and NGC 5846. Excluding NGC 3489, we derived for the other galaxies central  $\log R_{23}$  values of  $0.50 \pm 0.15$ ,  $0.58 \pm 0.11$ ,  $0.63 \pm 0.1$ ,  $0.70 \pm 0.05$ , and  $0.51 \pm 0.11$ . For the same galaxies, they derived  $0.93^{0.08}_{-0.11}$ ,  $0.58^{0.09}_{-0.10}$ ,  $0.68^{0.09}_{-0.11}$ ,  $0.75^{0.05}_{-0.06}$ ,  $0.68^{0.08}_{-0.09}$ . With the exception of NGC 3607, our and their results are in agreement within the errors.

The oxygen metallicity distribution is shown in the top panel of Fig. 13. The  $[\text{O}/\text{H}] = \log(\text{O}/\text{H}) - \log(\text{O}/\text{H})_{\odot}$  values were computed adopting a solar abundance of  $12 + \log(\text{O}/\text{H}) = 8.76$  from Caffau et al. (2008). The average metallicity is  $[\text{O}/\text{H}] = -0.06$ . Some values are as low as  $\approx 0.25$  times solar, while the highest derived metallicity is  $\approx$  twice solar.

## 5.2. AGN calibration

Storchi-Bergmann et al. (1998) (hereafter SB98) derived oxygen metallicity calibrations from a grid of models assuming

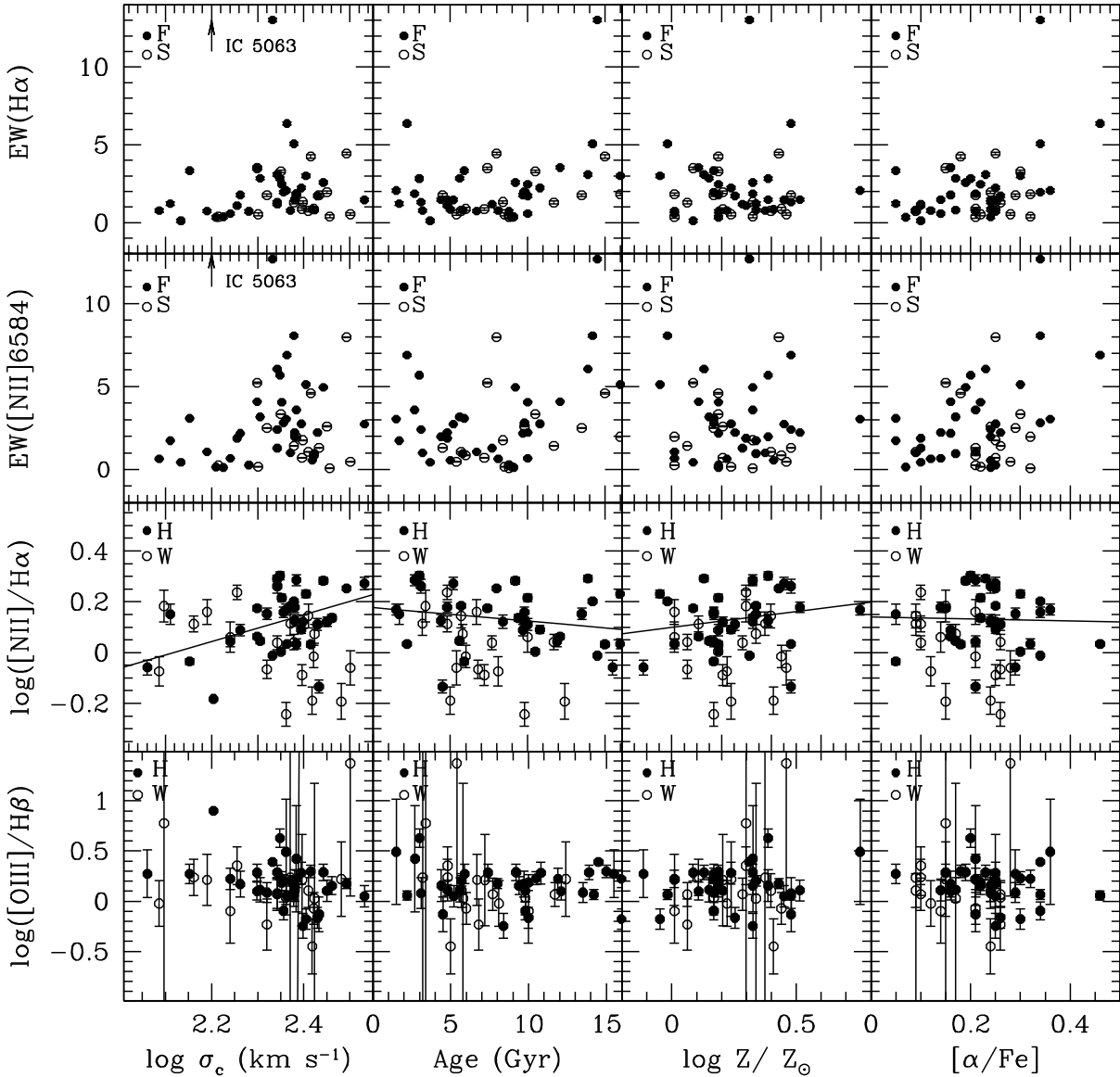


**Fig. 9.**  $H\alpha$  and [NII] equivalent widths, [NII]/ $H\alpha$  ratio, and [OIII]/ $H\beta$  ratio versus galaxy central velocity dispersion  $\sigma_c$ , age, metallicity  $Z$ , and  $[\alpha/Fe]$  ratio. In the two top rows, full dots are for fast rotators (F), while empty dots are for slow rotators (S). In the two bottom rows, full dots are for high emission galaxies (H), and empty dots are for weak emission galaxies (W), as defined in Sect. 3 and Table 4. For the third row panels, we show least square fits for the H subsample.

photoionization by a typical AGN continuum (the segmented power law of Mathews & Ferland 1987). The first calibration (hereafter SB1) is in terms of  $[OIII]\lambda\lambda 4959, 5007/H\beta$  and  $[NII]\lambda\lambda 6548, 6584/H\alpha$  (Eq. (2) in SB98), while the second calibration (hereafter SB2) is in terms of  $[OII]\lambda 3727/[OIII]\lambda\lambda 4959, 5007$  and  $[NII]\lambda\lambda 6548, 6584/H\alpha$  (Eq. (3) in SB98). The fitted calibrations are within  $\sim 0.05$  dex of the models. The models were computed assuming a gas density  $n_g = 300 \text{ cm}^{-3}$ . The correction required because of deviations from this density is  $-0.1 \times \log(n_g/300)$ , valid for  $100 \text{ cm}^{-3} \lesssim n_g \lesssim 10000 \text{ cm}^{-3}$ .

We derived oxygen metallicities for the R05+A06 sample using both SB1 and SB2. The electron densities  $n_e$  were calculated from the  $[SII]\lambda\lambda 6717, 31$  line ratios using the *temden* task within IRAF/STSDAS (Shaw & Dufour 1995), and assuming an electronic temperature  $T_e = 10000 \text{ K}$ . This was possible only for some galaxies in our sample (see Table 5), because the quality of our spectra is significantly poorer redward of  $\sim 6600 \text{ \AA}$ , and telluric absorption lines around  $6800 \text{ \AA}$  prevent in many cases

a reliable fit to the [SII] doublet. The derived electron densities are given in Table 5. As evident from the [SII] fluxes given in Table 2, both increasing and decreasing density profiles are present within our sample. The oxygen metallicities were then corrected for the density dependence assuming  $n_e \approx n_g$ . Because of the limited range of validity for the density correction, we discarded the galaxies with  $n_e < 100 \text{ cm}^{-3}$ . The [O/H] values obtained with SB1 and SB2 are compared in Fig. 12. The metallicities obtained with SB2 are on average  $\sim 0.09$  dex higher than those obtained with SB1, in agreement with SB98 who derived a shift of  $\sim 0.11$  dex between the two calibrations. The final metallicities are computed to be the average between the two values. The results are given in Col. 3 of Table 6.

We compare the results obtained with the Kob99 and with the SB98 calibrations in Fig. 13. The SB98 calibration provides an average oxygen abundance  $\sim 0.04$  dex higher than that obtained with Kob99. In addition, Kob99 infers a broader metallicity range than SB98.

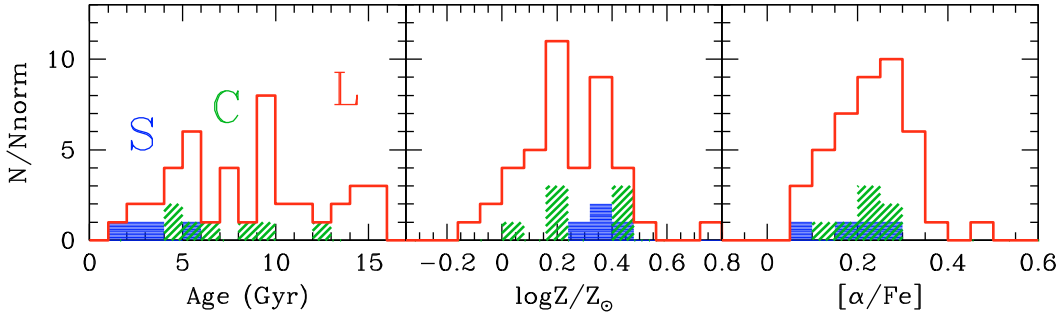


**Fig. 10.** Age, metallicity, and  $[\alpha/\text{Fe}]$  distributions for Seyfert-like galaxies (S), LINERs (L), and “composites” (C).

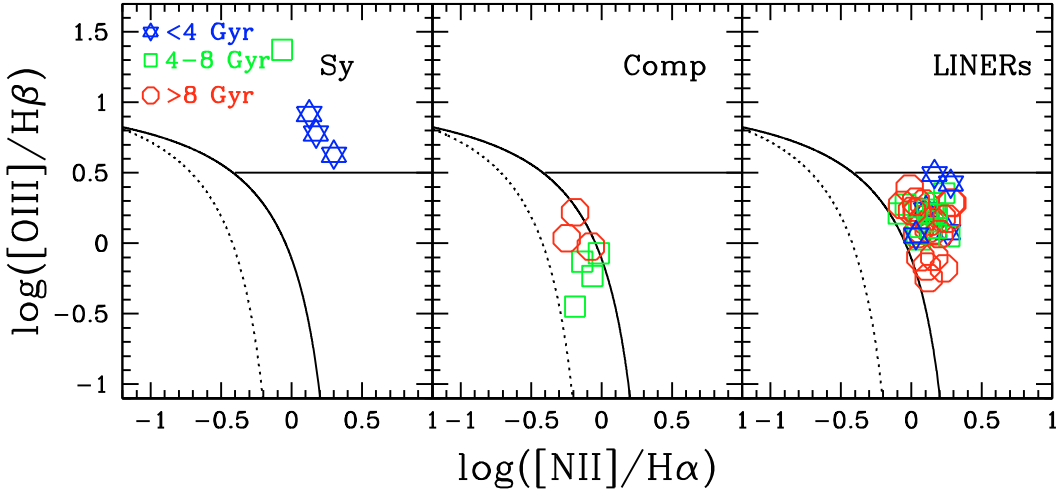


**Fig. 11.** BPT diagnostic diagram for Seyfert galaxies (*left panel*), “composites” (*center*), and LINERs (*right panel*). The data were color-coded according to the galaxy age as derived in Paper III: blue stars are for ages younger than 4 Gyr, green squares for ages between 4 and 8 Gyr, and red circles for ages older than 8 Gyr.

### 5.3. Abundance gradients

We studied the behavior of the oxygen metallicity as function of galactocentric distance. The  $[\text{O}/\text{H}]$  distributions obtained with Kob99 and SB98 in the three more internal annuli ( $r \leq r_e/16$ ,  $r_e/16 < r \leq r_e/8$ ,  $r_e/8 < r \leq r_e/4$ ) are shown in Fig. 14. The samples are not very large because of the increased difficulty in measuring the emission lines in the more external annuli. Emission lines are too faint to allow a reliable abundance measurement in the more external annulus ( $r_e/4 < r \leq r_e/2$ ). The results obtained with the Kob99 and SB98 calibrations are inconsistent: in the first case, the oxygen metallicity tends to increase from the galaxy center outwards. In the second case, the opposite behavior is observed. The latter trend is more consistent with the negative metallicity gradients of the stellar populations.

### 5.4. Comparison with stellar metallicities

To understand the origin of the warm gas in ETGs, it is important to compare the nebular metallicities with those of the stellar populations. We already derived the (total) stellar metallicities ( $Z$ ) and the  $[\alpha/\text{Fe}]$  ratios for the R05+A06 sample using the Lick indices in Paper III. The comparison with the nebular metallicities is not straightforward, since the emission lines provide a direct measure of the oxygen abundance, while the Lick indices depend on a mixture of different elements. In this paper, we compute the oxygen stellar metallicities from the  $Z$  and  $[\alpha/\text{Fe}]$  values derived in Paper III, assuming that O belongs to the  $\alpha$ -enhanced group (Ne, Na, Mg, Si, S, Ca, Ti, and also N). The comparison between

gas and stellar metallicities is shown in Fig. 15. The clear result is that, irrespective of the adopted calibration (Kob99 or SB98), the gas metallicity tends to be lower than the stellar metallicity. The effect is more severe for the galaxies with the highest stellar metallicities. A Spearman test shows that in both cases the stellar and gas metallicities are poorly correlated.

We plot the central ( $r \leq r_e/16$ ) nebular metallicities obtained with Kob99 and SB98 versus the galaxy stellar velocity dispersions in Fig. 16. Linear square fits provide an increasing trend of  $[\text{O}/\text{H}]$  with  $\sigma_c$  in both cases. However, the Spearman correlation coefficients are low ( $r_s = 0.25$  with  $N = 39$  degrees of freedom for Kob99, top panel, and  $r_s = 0.08$  with  $N = 22$  degrees of freedom for SB98, bottom panel), indicating that the correlations are weak. For comparison, we plot in Fig. 16 the stellar metallicity- $\sigma_c$  relations derived by ourselves in Paper III (A07) and by Thomas et al. (2005) for low density environment ETGs. The A07 relation was appropriately rescaled to account for the solar metallicity adopted in this paper<sup>2</sup>. In Fig. 16, the fits provide  $[\text{O}/\text{H}]_{\text{gas}} \sim -0.08$  and  $[\text{O}/\text{H}]_{\text{gas}} \sim -0.03$  at  $\sigma_c = 200 \text{ km s}^{-1}$  for Kob99 and SB98, respectively. For comparison, the A07 relation gives a stellar metallicity of  $\sim 0.18$  dex at the same  $\sigma$ , i.e., 0.26 dex and 0.21 dex higher than those obtained for the warm gas with Kob99 and SB98, respectively. The discrepancy is even larger if we consider the Thomas et al. (2005) relation, which provides a metallicity of 0.34 dex at  $\sigma_c = 200 \text{ km s}^{-1}$ , i.e.

<sup>2</sup>  $Z_\odot = 0.018$  in A07, while we adopt  $Z_\odot = 0.0156$  from Caffau et al. (2009) in this paper. This implies a correction term of  $\log(0.018/0.0156) = 0.06$  dex to be applied to the A07 relation.

**Table 5.** Electron densities  $n_e$  derived from [SII]6716/6731 assuming  $T = 10\,000$  K.

Galaxy	[SII]6717/6731	$n_e$ (cm <sup>-3</sup> )
NGC 1052	1.11 ± 0.03	384.1
NGC 1209	1.19 ± 0.13	254.8
NGC 1297	1.08 ± 0.10	423.6
NGC 1380	0.98 ± 0.15	653.9
NGC 1453	1.28 ± 0.09	141.5
NGC 1533	1.22 ± 0.16	212.0
NGC 1553	1.21 ± 0.30	229.3
NGC 1947	1.32 ± 0.04	95.0
NGC 2749	1.18 ± 0.08	267.7
NGC 2974	1.10 ± 0.05	385.1
NGC 3136	1.60 ± 0.11	<26
NGC 3268	1.32 ± 0.13	103.4
NGC 3489	1.21 ± 0.14	223.1
NGC 3607	1.24 ± 0.20	185.4
NGC 3962	1.27 ± 0.06	147.1
NGC 4374	1.45 ± 0.17	<26
NGC 4636	1.45 ± 0.15	<26
NGC 4696	1.31 ± 0.08	110.0
NGC 5044	1.51 ± 0.06	<26
NGC 5077	1.26 ± 0.06	158.7
NGC 5090	1.48 ± 0.20	<26
NGC 5193	1.57 ± 0.50	<26
NGC 5266	1.06 ± 0.04	476.7
NGC 5363	1.27 ± 0.05	148.8
NGC 5813	1.34 ± 0.22	83.4
NGC 5846	1.10 ± 0.21	395.6
NGC 5898	1.55 ± 0.34	<26
NGC 6758	1.42 ± 0.17	<26
NGC 6868	1.43 ± 0.08	<26
NGC 6958	0.77 ± 0.03	1605.9
NGC 7007	1.53 ± 0.15	<26
NGC 7079	0.95 ± 0.21	732.3
NGC 7097	1.23 ± 0.06	200.4
NGC 7377	1.43 ± 0.14	<26
IC 1459	0.97 ± 0.04	674.2
IC 3370	1.48 ± 0.05	<26
IC 4296	1.10 ± 0.15	400.7
IC5063	1.08 ± 0.01	433.3

~0.4 dex higher than the nebular metallicity. We notice that the discrepancy between gas and stars persists (and is even more significant) if we consider only the strong emission-line (H) galaxies (see classification in Table 4).

## 6. Comparison with models

The ionizing source in LINERs remains poorly understood. Among the proposed mechanisms, we recall sub-Eddington accretion onto a supermassive black hole (e.g., Ho 1999b; Kewley et al. 2006; Ho 2009a), photoionization by old PAGB stars (e.g. Trinchieri & di Serego Alighieri 1991; Binette et al. 1994; Stasińska et al. 2008), and fast shocks (Koski & Osterbrock 1976; Heckman 1980; Dopita & Sutherland 1995; Allen et al. 2008).

The first hypothesis is strongly supported by our current knowledge of the demography of central BHs based on direct dynamical searches (Magorrian et al. 1998; Ho 1999a; Kormendy 2004), according to which massive BHs appear to be a generic component of galaxies with a bulge. As shown by Ho et al. (1997c), local stellar mass loss can supply the fuel necessary for accretion rates of  $\dot{M} = 0.001\text{--}0.1 M_{\odot} \text{ yr}^{-1}$ . Thus, radiatively inefficient accretion flows onto a central BH (see Quataert 2001

**Table 6.** [O/H] values obtained with the Kobulnicky et al. (1999) calibration (Kob99), and the Storch-Bergmann et al. (1998) calibration (SB98).

Galaxy	log(O/H) + 12 (Kob99)	log(O/H) + 12 (SB98)
NGC 128	8.44 ± 0.24	–
NGC 1052	8.52 ± 0.15	8.67 ± 0.03
NGC 1209	8.63 ± 0.19	8.78 ± 0.04
NGC 1297	–	8.59 ± 0.04
NGC 1380	8.81 ± 0.20	8.75 ± 0.04
NGC 1453	8.55 ± 0.19	8.76 ± 0.04
NGC 1533	8.76 ± 0.18	8.74 ± 0.04
NGC 1553	8.48 ± 0.31	8.87 ± 0.04
NGC 2749	–	8.7 ± 0.04
NGC 2911	8.56 ± 0.16	–
NGC 2974	8.53 ± 0.18	8.86 ± 0.04
NGC 3258	8.94 ± 0.17	–
NGC 3268	8.83 ± 0.16	8.85 ± 0.04
NGC 3607	8.86 ± 0.18	8.94 ± 0.04
NGC 3962	8.62 ± 0.18	8.83 ± 0.04
NGC 4374	8.79 ± 0.17	–
NGC 4552	8.98 ± 0.16	–
NGC 4636	8.75 ± 0.17	–
NGC 4696	8.71 ± 0.16	8.82 ± 0.04
NGC 4697	8.85 ± 0.26	–
NGC 5044	8.66 ± 0.16	–
NGC 5077	8.40 ± 0.17	8.69 ± 0.04
NGC 5090	8.93 ± 0.16	–
NGC 5193	9.01 ± 0.16	–
NGC 5266	8.20 ± 0.22	8.72 ± 0.04
NGC 5328	8.96 ± 0.23	8.54 ± 0.17
NGC 5363	8.32 ± 0.21	8.68 ± 0.03
NGC 5813	8.84 ± 0.17	–
NGC 5846	8.84 ± 0.17	8.71 ± 0.04
NGC 5898	8.75 ± 0.21	–
NGC 6721	8.88 ± 0.16	–
NGC 6758	8.63 ± 0.18	–
NGC 6776	–	–
NGC 6868	8.48 ± 0.19	–
NGC 6876	8.97 ± 0.16	–
NGC 6958	–	8.82 ± 0.04
NGC 7079	8.72 ± 0.28	8.78 ± 0.05
NGC 7097	8.59 ± 0.17	8.67 ± 0.03
NGC 7135	8.64 ± 0.16	–
NGC 7192	8.83 ± 0.19	–
NGC 7377	8.60 ± 0.25	–
IC 1459	8.54 ± 0.16	8.78 ± 0.03
IC 2006	8.85 ± 0.21	–
IC 3370	8.49 ± 0.21	–
IC 4296	8.85 ± 0.17	8.88 ± 0.04
IC5063	–	8.69 ± 0.03

for a review) provide an attractive solution for explaining the origin of LINERs. Additional evidence of AGN activity come from X-ray and radio observations, which have detected compact nuclear X-ray and radio sources, sometimes exhibiting variability, in a significant fraction of LINERs (see e.g. Terashima 1999; Flohic et al. 2006; Filho et al. 2006; Gonzalez-Martin et al. 2009; Pian et al. 2010). On the other hand, some LINERs lack evidence of a central AGN, leaving space for alternative explanations of the observed emission lines. X-ray and radio studies are available in the literature for a few galaxies in our sample. Compact nuclear X-ray and/or radio sources have been detected in IC 5063 (Koyama et al. 1992), NGC 777 (Ho & Ulvestad 2001), NGC 1052, NGC 4374, IC 1459 (Gonzalez-Martin et al. 2009), NGC 5363 (Gonzalez-Martin et al. 2009; Filho et al. 2006), NGC 1553 (Blanton et al. 2001), NGC 3557

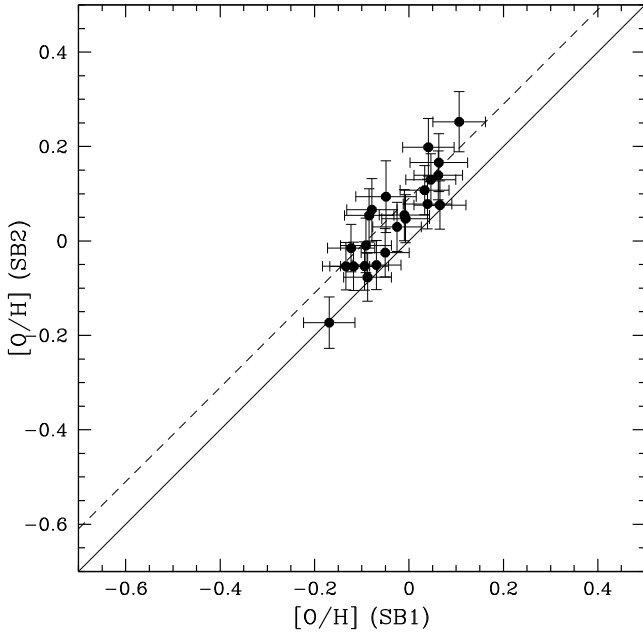


**Fig. 12.** Oxygen abundance at  $r \leq r_e/16$  obtained with the second calibration of Storchi-Bergmann et al. (1998) against the values obtained with the first calibration. For comparison, the one-to-one relation is drawn as a solid line, while the dashed line indicates a systematic shift of 0.09 dex.

(Balmaverde et al. 2006), NGC 5090 (Grützbauch et al. 2007), IC 4296 (Pellegrini et al. 2003), NGC 5077, (Filho et al. 2006), and NGC 4552 (Nagar et al. 2002; Filho et al. 2004). Other galaxies observed in X-ray and/or radio lack evidence of AGN activity: NGC 3607, NGC 4636, NGC 5813, (Gonzalez-Martin et al. 2009; Filho et al. 2006), NGC 4696, NGC 5846 (Gonzalez-Martin et al. 2009), and NGC 6876 (Machacek et al. 2005). High quality X-ray imaging of NGC 4636 revealed the signature of shocks, probably driven by energy deposited off-center by jets (Jones et al. 2002; Baldi et al. 2009).

Shock heating was initially proposed as a viable excitation mechanism to solve the so-called “temperature problem” of Seyferts and LINERs, in which the electron temperatures observed were found to be systematically higher than predicted by photoionization models. Koski & Osterbrock (1976) and Fosbury et al. (1978) argued that shocks are essential for explaining the observed [OIII] line ratios of the prototypical LINER NGC 1052. Dopita & Sutherland (1995) and Allen et al. (2008) presented extensive grids of high velocity shock models, and showed that the emission line ratios observed in LINERs can be modeled in terms of fast shocks ( $150\text{--}500\text{ km s}^{-1}$ ) in a relatively gas poor environment.

The findings that the emission-line flux correlates with the host galaxy stellar luminosity within the emission-line region (Macchetto et al. 1996), and that the line flux distribution closely follows that of the stellar continuum (Sarzi et al. 2006, 2009), have been presented as evidences in support of the PAGB scenario. These results suggest that the sources of ionizing photons are distributed in the same way as the stellar population. Sarzi et al. (2009) tried to model the  $H\beta$  EW spatial distribution based on the assumption that the ionizing photons originate in an underlying old stellar population. They showed that to obtain an almost constant EW it is necessary to assume that the gas radial profile decreases more gently than the ionizing radiation, or alternatively that the ionizing photons are more concentrated

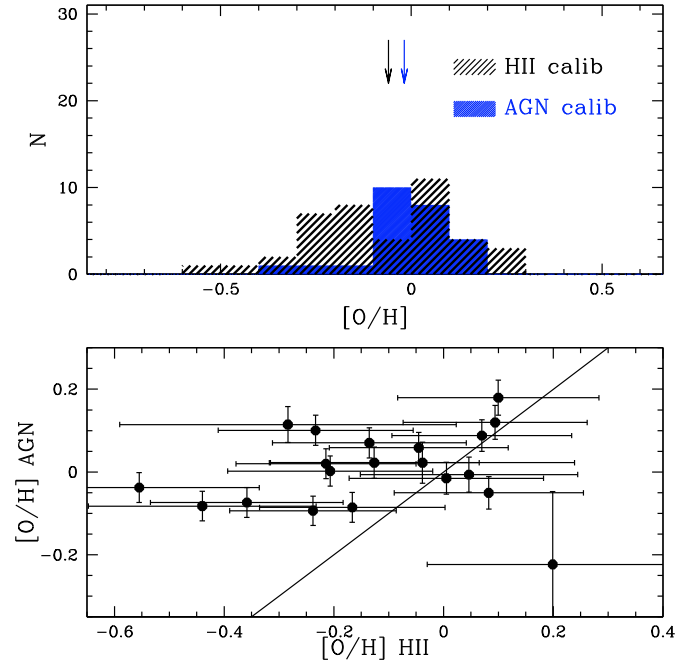


**Fig. 13.** *Top panel:* oxygen abundance distributions ( $[O/H] = \log(O/H) - \log(O/H)_\odot$ , where  $12 + \log(O/H)_\odot = 8.76$  from Caffau et al. 2008) derived for the R05+A06 sample at  $r \leq r_e/16$ . The dashed histogram was obtained with the Kobulnicky et al. (1999) calibration valid for HII regions, while the full histogram was obtained with the Storchi-Bergmann et al. (1998) calibration for AGNs. Vertical arrows indicate the average [O/H] values obtained with the two methods. *Bottom panel:* comparison of the metallicities obtained with the two methods for 20 galaxies in common. The solid line is the one-to-one relation.

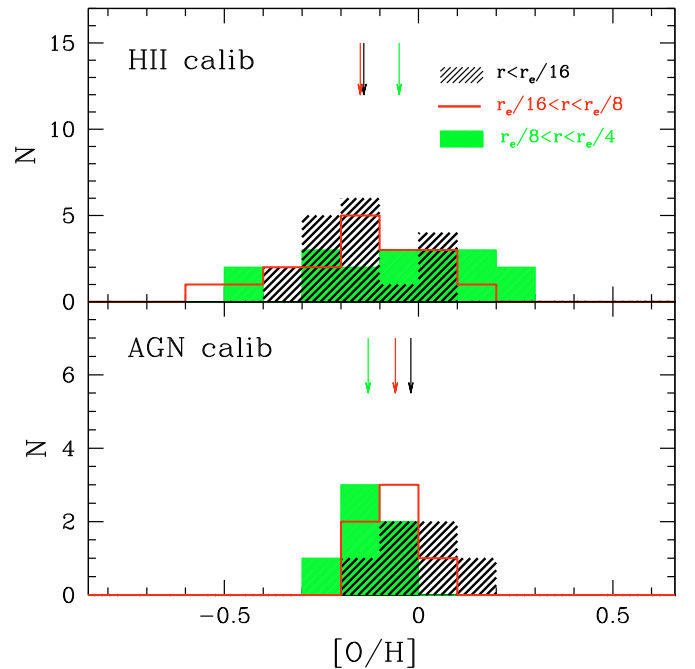


**Fig. 14.** Oxygen abundance distributions in the three more internal annuli ( $r \leq r_e/16$ ,  $r_e/16 < r \leq r_e/8$ ,  $r_e/8 < r \leq r_e/4$ ) obtained with the Kob99 calibration (18 galaxies, *top panel*), and with the SB98 calibration (6 galaxies, *bottom panel*). Vertical arrows indicate the average values for the distributions. Note that the metallicity increases from the galaxy center outwards with the Kob99 calibration, while the opposite trend is obtained with the SB98 calibration.

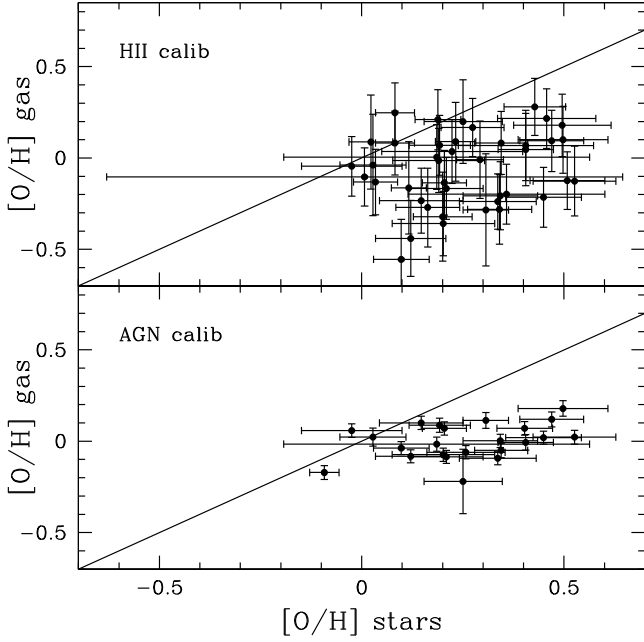


**Fig. 15.** Nebular oxygen abundance versus star oxygen abundance. The latter was derived from the  $Z$  and  $[\alpha/\text{Fe}]$  values obtained in Paper III. In the top and bottom panels, the nebular metallicities were obtained with the Kob99 and SB98 calibration, respectively.

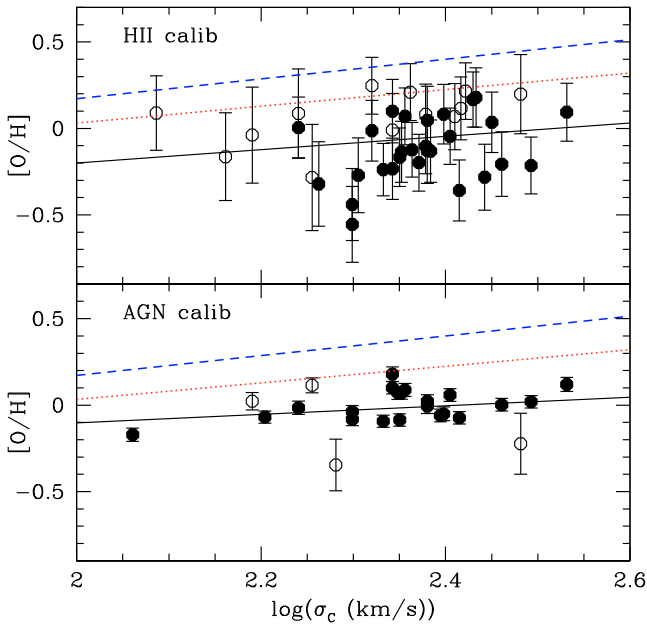


**Fig. 16.** Oxygen abundances derived with the Kob99 (*top*) and SB98 (*bottom*) calibration at  $r \leq r_e/16$  versus the galaxy central stellar velocity dispersion. Full symbols are the high emission galaxies (H), as defined in Table 4. The solid lines are the least square fits to the data. The dashed and dotted lines are the relations derived by Thomas et al. (2005) and A07 for the stars, rescaled to account for the solar metallicity  $Z_\odot = 0.0156$  adopted in this paper.

than the bulk of the stellar populations. The presence of negative metallicity gradients in ETGs (e.g., Annibali et al. 2007) may explain this effect, because in general the ionizing flux from old populations is stronger for higher metallicities. The Stasińska et al. (2008) models are able to reproduce the emission line ratios of LINERs provided that the ionization parameter is sufficiently high ( $\log U > -4$ ). Binette et al. (1994) and

Cid Fernandes et al. (2009) demonstrated that photoionization by PAGB stars can only explain LINERs with relatively weak emission lines. Binette et al. (1994) estimated that the  $H\alpha$  equivalent width produced by a 8 Gyr old and a 13 Gyr old simple stellar populations is  $0.6 \text{ \AA}$  and  $1.7 \text{ \AA}$ , respectively. Stronger emission lines require far more ionizing photons than old stars can provide.

A first-order test of the validity of the PAGB scenario consists of a comparison of the observed and predicted EWs. Following the computations of Binette et al. (1994), we assume that photoionization by old stars produce a typical emission of  $1 \text{ \AA}$  in  $H\alpha$ . Comparing this value with our measured central ( $r < r_e/16$ ) EWs, we find that PAGB photoionization alone can explain the observed nuclear emission in only 11 out of the 49 galaxies classified as LINERs/composites in our sample (i.e. in  $\approx 22\%$  of the LINERs/Comp sample). This implies that, for the majority of the cases, some mechanism other than PAGB stars must operate in the central regions of LINERs. On the other hand, as we progressively move toward larger radii, an increasing number of LINERs enter the  $\text{EW}(H\alpha) \sim 1 \text{ \AA}$  transition region, where the emission strength is compatible with photoionization by PAGB stars alone. Thus, while our computations exclude PAGB stars playing a significant role in the central galaxy regions, we cannot exclude them from being an important excitation source at larger radii. Interestingly, Sarzi et al. (2009) quote a  $3''$  radius for the maximum extent of central activity, which for their sample galaxies corresponds on average to  $0.11 r_e$ .

One of the arguments presented in support of the PAGB photoionization scenario is that the emission flux closely follows the stellar continuum. In disagreement with other results (e.g. Sarzi et al. 2009), we have shown in Sect. 3.3 that the EW (emission flux over continuum flux) decreases with radius. Is this incompatible with the PAGB scenario? Answering this question is not straightforward. First of all, we have shown that the strongest decrease in EW occurs from the nuclear to the second ( $r_e/16 < r \leq r_e/8$ ) annulus, the decrease with radius being much gentler at larger radii. Unfortunately, our data lack the depth necessary to reliably trace the emission strength beyond  $r_e/4$ . Second, a well established decreasing trend in EW would not be *per se* incompatible with the PAGB scenario: because of the presence of age/metallicity gradients in the stellar population, the ratio of the ionizing flux to the optical continuum is not necessarily constant. A reliable radial prediction of the ionizing photon budget stems from a detailed analysis of the combined effect of age and metallicity on the PAGB population, which is beyond the aims of this paper.

Since the nuclear emission requires a different mechanism from PAGB photoionization, we compare in Fig. 17 our ( $r \leq r_e/16$ ) data, corrected for reddening, with the dusty AGN models of Groves et al. (2004), and the fast shock models of Allen et al. (2008). Among the data points, we identify objects with compact nuclear X-ray and/or radio source detections, probably hosting an AGN, and objects with equivalent width in  $H\alpha < 1 \text{ \AA}$ , compatible with sole ionization from PAGBs. We note that three galaxies (NGC 777, NGC 4552, and NGC 3557) exhibit AGN activity in X ray or radio observations, and at the same time have  $\text{EW}(H\alpha) < 1$ . Comparing dusty models with reddening-corrected data is not completely self-consistent; however, the effect of extinction in the BPT diagram is negligible.

Both the AGN and shock models were developed using the code MAPPINGS III (Dopita et al. 1982; Sutherland & Dopita 1993), implemented with dust and radiation pressure

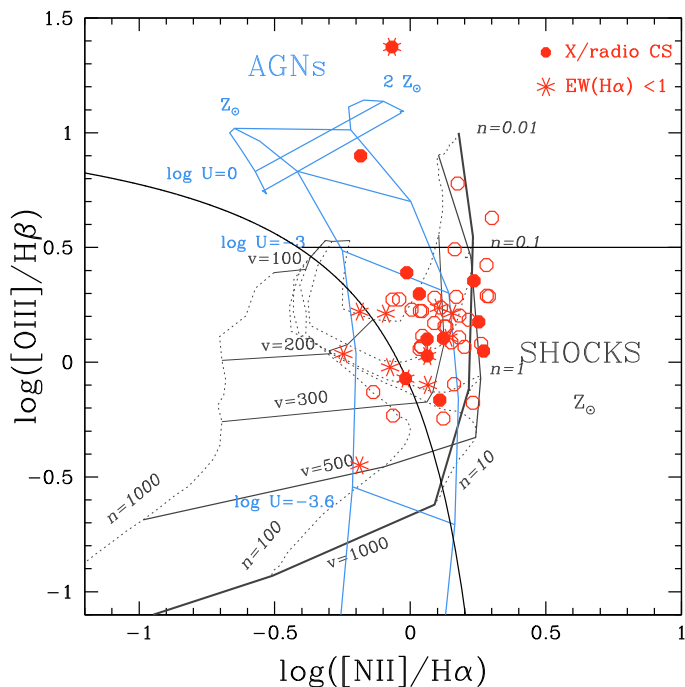


**Fig. 17.** BPT diagram for our galaxies at  $r \leq r_e/16$  with superimposed the shock models of Allen et al. (2008) and the dusty-AGN models of Groves et al. (2004). Full dots indicate objects where compact nuclear X-ray and/or radio sources have been detected (X/radio CS), consistently with the presence of an AGN, while stars are for objects with equivalent width in  $H\alpha < 1 \text{ \AA}$ , compatible with ionization from PAGBs. Notice that three galaxies (NGC 777, NGC 4552, and NGC 3557) are X/radio CS and at the same time have  $EW(H\alpha < 1)$ . The shock models have solar metallicity, densities from  $n = 0.01 \text{ cm}^{-3}$  to  $1000 \text{ cm}^{-3}$ , velocities from  $v = 100 \text{ km s}^{-1}$  to  $500 \text{ km s}^{-1}$ , and magnetic field  $B = 1 \text{ \mu G}$ . The plotted AGN models have solar and twice solar metallicities,  $n = 1000 \text{ cm}^{-3}$ , and ionization parameters from  $\log U \sim -4$  to 0. The models were downloaded from the Brent Groves web page <http://www.strw.leidenuniv.nl/~brent/itera.html> using the ITERA tool.

(Groves et al. 2004). The AGN models were developed for different metallicities, and assuming a power law with slope  $\alpha$  between  $-1.2$  and  $-2.0$  for the ionizing spectrum. For the AGN models in Fig. 17,  $\alpha = -1.4$ ,  $Z = Z_\odot$  and  $2 Z_\odot$ ,  $n_H = 1000 \text{ cm}^{-3}$ , and  $\log U$  between  $-4$  and 0. LINERs and Seyferts are both explainable with being AGNs, provided that the former have much lower ionization parameters than the latter. According to these models, the galaxies in our sample should have gas metallicities much above solar. This disagrees with the oxygen metallicities derived in Sect. 5 with the Storchi-Bergmann et al. (1998) calibration. The discrepancy arises from the use of a power law in the Groves et al. (2004) models compared to the typical AGN continuum of Mathews & Ferland (1987) adopted by SB98. Indeed, SB98 noticed that models obtained with power-law ionizing continua yield systematically higher (up to 0.5 dex) metallicities than models that adopt a typical AGN continuum.

Based on the assumption that all the central LINERs activity is powered by a sub-Eddington accretion AGN, we can determine the accretion rate from the  $L_{[\text{OIII}]} / \sigma^4$  ratio (where  $L_{[\text{OIII}]}$  is the extinction-corrected  $[\text{OIII}]$  luminosity), which is proportional to  $L/L_{\text{EDD}}$  (Heckman et al. 2004). The result is shown in Fig. 18. The accretion rate increases systematically along the sequence composite  $\rightarrow$  LINERs  $\rightarrow$  Seyferts (left panel) in agreement with the findings of Ho (2009a). Galaxies with compact

nuclear X-ray/ radio sources, likely hosting an AGN, also tend to have higher accretion rates than non-AGN galaxies (right panel). We note that since  $L \propto \eta L_{\text{EDD}} \propto \eta \sigma^4$ , and  $\eta \ll 1$  in the sub-Eddington accretion regime, the AGN luminosity can vary significantly for a fixed  $\sigma$  depending on the accretion  $\eta$ . This implies that it is necessary to assume a maximum, sub-Eddington, accretion rate to reproduce the observed trend between the emission strength and  $\sigma$ .

The Allen et al. (2008) shock models are dust free, and were computed for different chemical abundances, pre-shock densities  $n$  from  $0.01$  to  $1000 \text{ cm}^{-3}$ , velocities up to  $1000 \text{ km s}^{-1}$ , and magnetic parameters  $B/n^{1/2}$  from  $10^{-4}$  to  $10 \text{ \mu G cm}^{3/2}$ , where  $B$  is the pre-shock transverse magnetic field. In Fig. 17, we plot the models with solar metallicity and  $B = 1$ . With these parameters, the bulk of LINERs in our sample is well reproduced by pre-shock densities  $n = 0.01 - 10 \text{ cm}^{-3}$ , and shock velocities  $v = 200 - 500 \text{ km s}^{-1}$ . Using a stronger magnetic field implies higher densities for our sample. For instance, for  $B = 10 \text{ \mu G}$ , our data are consistent with pre-shock densities as high as  $n \approx 100 \text{ cm}^{-3}$ . This range in  $B$  is typical of the ISM (e.g., Rand & Kulkarni 1989).

Are these densities consistent with those derived from the observed  $[\text{SII}](6717)/[\text{SII}](6731)$  ratios? As shown in Table 5, the majority of our galaxies have ratios  $> 1$ , implying  $n_e \lesssim 600 \text{ cm}^{-3}$  for an assumed  $T = 10000 \text{ K}$ . A significant fraction of galaxies have ratios around 1.45, which is the saturation limit for  $n \rightarrow 0$ . These values are consistent with pre-shock densities as low as  $n < 10 \text{ cm}^{-3}$ . Indeed, as the density of the material passing through the shock increases, the density indicated by the  $[\text{SII}]$  ratio also increases. However, the amount of compression depends critically upon the magnetic parameter (Dopita & Sutherland 1995). In the Allen et al. (2008) models,  $[\text{SII}](6717)/[\text{SII}](6731) \sim 0.7$  and  $\sim 1$  for a pre-shock density  $n = 10 \text{ cm}^{-3}$ , and  $B = 1$  and  $10 \text{ \mu G}$ , respectively.

In the fast shock scenario, where does the mechanical energy come from? Dopita & Sutherland (1995) distinguish between two possible types of gas dynamical flows: jet-driven and accretion-driven flows. Evidence of jets in LINERs comes from observations that detect low-luminosity AGNs associated with radio sources with a high brightness temperature and/or elongated radio morphology (e.g., Nagar et al. 2001). In accretion-driven flows, the shock is either the result of the collision of cool clouds that have dropped out of a cooling flow into the potential of the galaxy (e.g. Crawford & Fabian 1992) or have been accreted from a companion galaxy. Shocks may also occur in the outer accretion disk about the central object either by means of the dissipation of turbulence, dynamical instabilities, or spiral shocks (e.g. Dopita et al. 1997). We suppose that the mechanical energy may also come from turbulent motion of gas clouds, either injected by stellar mass loss or accreted, within the potential well of the galaxy.

Figure 17 shows that the shock velocities required to reproduce the distribution of LINERs in the BPT diagram range between  $200$  and  $500 \text{ km s}^{-1}$ . Are the before mentioned mechanisms able to account for these high shock velocities? It seems that jet-driven flows or accretion onto a central massive BH may well do (e.g., Nagar et al. 2005, Dopita et al. 1997). On the other hand, it is difficult to establish whether, in the absence of these sources, pure gravitational motion of clouds within the potential well of the galaxy can produce collision at the required velocities. Close to the center of a relaxed stellar system, the gas should quickly relax into a disk-like configuration and orbit at a velocity close to the circular one, even though not necessarily in the same direction of stars. This is indeed confirmed by

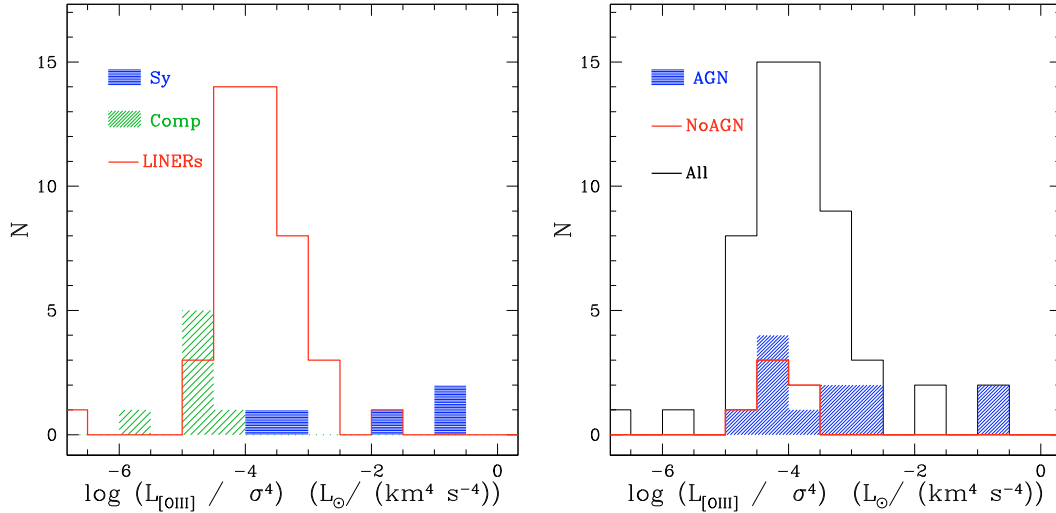


**Fig. 18.** Distribution of  $L_{[\text{OIII}]}/\sigma^4$  ratio for Seyferts, composites and LINERs (left panel), and for the total sample and galaxies classified as AGN and non-AGN from X-ray/radio data (right panel).

observations, showing regular gaseous disk structures and coherent gas motions (see e.g. Zeilinger et al. 1996; Sarzi et al. 2006). If most of the clouds were to rotate in the same direction, it would then be rather difficult for them to collide at the high speed required. On the other hand, observations detect an additional gaseous component of high gas velocity dispersion, in the range 150–250 km s<sup>-1</sup> (Bertola et al. 1995; Zeilinger et al. 1996; Emsellem et al. 2003). Sarzi et al. (2006) found that  $\sigma_{\text{gas}}$  is generally smaller than the stellar velocity dispersion  $\sigma_*$ , but in some cases  $\sigma_{\text{gas}} \sim \sigma_*$ , either only in the central regions or over most of the field. For a sample of 345 galaxies, with Hubble type from E to Sbc, Ho (2009b) found that the gas dispersions strongly correlate with the stellar dispersions over the velocity dispersion range of  $\sigma \approx 30\text{--}350$  km s<sup>-1</sup>, such that  $\sigma_{\text{gas}}/\sigma_* \approx 0.6\text{--}1.4$ , with an average value of 0.80. All these observations suggest that random motions are crucial for the dynamical support of the gas. Projected velocity dispersions in the range 150–250 km s<sup>-1</sup> translate, based on the assumption of isotropy, into intrinsic 3D velocity dispersions in the range 260–430 km s<sup>-1</sup><sup>3</sup>. This is a crude estimate of the intrinsic velocity dispersions since studies indicate deviation from isotropy (e.g. Merrifield et al. 2001). Given these values, collisions at a speed between 200 and 500 km s<sup>-1</sup> cannot be excluded.

We compare the shock models of Allen et al. (2008) with our data in a luminosity versus velocity plane in Fig. 19. For the data, we adopted a velocity of  $\sqrt{3}\sigma_c$ , which is a first-order approximation for the shock velocity based on the assumption that the shocks are caused by motions of gas clouds in the galaxy potential well. The models are plotted for four density values ( $n = 0.01, 1, 10, 100$  cm<sup>-3</sup>), and for three values of the transverse magnetic field ( $B = 0.1, 1, 10$   $\mu\text{G}$ ). The shock luminosity increases significantly with both the shock velocity and the gas density. The dependence on the magnetic parameter is almost null in H $\alpha$  (and modest in [NII]). The observed nuclear H $\alpha$  luminosities were corrected for reddening in terms of the values derived in Table 2. Some galaxies have very large reddening, associated with large uncertainties, and have quite high luminosities once corrected for extinction (NGC 777, NGC 1521,

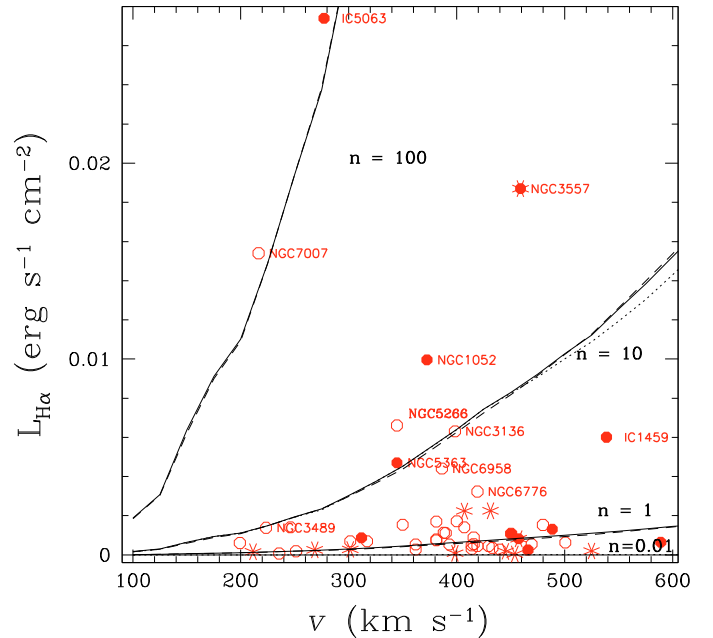


**Fig. 19.** Shock models of Allen et al. (2008) compared with our  $r \leq r_c/16$  H $\alpha$  luminosities, corrected for reddening. The shock models are plotted for 4 density values ( $n = 0.01, 1, 10, 100$  cm<sup>-3</sup>), and magnetic fields  $B = 0.1$  (dotted line),  $B = 1$  (solid line), and  $B = 10$   $\mu\text{G}$  (dashed line). The velocity in the abscissa is the shock velocity for the models, and  $\sqrt{3}\sigma_c$  for the galaxies. The different symbols used to plot the data are the same as in Fig. 17. We indicate the name of the galaxies with the largest  $L_{\text{H}\alpha}$  values, NGC 777, once corrected for the high extinction ( $E(B - V) = 1.6$ ), has  $L_{\text{H}\alpha} \sim 0.06$  erg s<sup>-1</sup> cm<sup>-2</sup> and falls outside the plot boundaries.

NGC 7007, NGC 3557). Their  $L_{\text{H}\alpha}$  should be interpreted with caution. Figure 19 shows that, for almost all the galaxies in our sample, the observed luminosities are well reproduced by models with pre-shock densities  $n \lesssim 10$  cm<sup>-3</sup>. This does not prove that shocks are the excitation mechanism in LINERs, but indicates that this scenario is compatible with the data. We note that shocks could provide a natural explanation of the observed *half-cone-shaped* distribution in the line luminosity/EW versus  $\sigma$  plane (see also Fig. 9). They could also explain the observed

<sup>3</sup> The total 3D velocity dispersion satisfies  $\sigma^2 = \sigma_x^2 + \sigma_y^2 + \sigma_z^2$ , because of the Pythagoras theorem and basic statistics of the second moments. If the dispersion is isotropic,  $\sigma_x = \sigma_y = \sigma_z$  by definition, and  $\sigma^2 = 3\sigma_x^2$ .

[NII]/H $\alpha$  versus  $\sigma_c$  correlation (Fig. 9). The shock models predict an increase in the [NII]/H $\alpha$  line ratio with the shock velocity. This is because higher velocity shocks result in harder and more luminous ionizing spectra. It is interesting that the weak emission galaxies in our sample, compatible with pure photoionization by PAGB stars at their center, are those deviating from the [NII]/H $\alpha$  vs  $\sigma_c$  relation in Fig. 9. Phillips et al. (1986) also found that the [NII]/H $\alpha$  ratio increases with the galaxy absolute magnitude in a sample of LINERs. They interpreted this behavior as being caused by differences in metallicities or differing ionization conditions.

## 7. Summary and conclusions

We have detected optical emission lines in 89% of the galaxies in our sample. This large fraction is somehow expected, since our sample was selected among a compilation of galaxies showing traces of ISM, and it is thus biased toward spectra containing emission lines. This fraction is higher than that derived by Phillips et al. (1986) (55%–60%), Macchetto et al. (1996) (72%–85%), Sarzi et al. (2006) (75%), Yan et al. (2006) (52%), and Serra et al. (2008) (60%) for other samples of early-type galaxies. If we consider only the galaxies in our sample with  $\text{EW}(\text{H}\alpha + [\text{NII}]6584) > 3 \text{ \AA}$ , the detection fraction drops to 57%.

The incidence and the strength of emission in our sample is independent of their elliptical or lenticular morphological classes. These results agree with Phillips et al. (1986), while on the other hand Macchetto et al. (1996) and Sarzi et al. (2006) found a higher incidence of emission in lenticular than in elliptical galaxies. Following the studies of Cappellari et al. (2007) and Emsellem et al. (2007), we attempted a classification between fast and slow rotators in our sample. Fast and slow rotators account for  $\sim 70\%$  and  $\sim 30\%$  of the sample, respectively. This is interesting given that the sample is composed of  $\sim 70\%$  ellipticals and  $\sim 30\%$  lenticulars. Emission does not depend on the fast and slow rotator classification in our sample.

The EW of the lines tends to decrease from the center outwards. The [NII] line declines more steeply than the H $\alpha$ . However, given the uncertainties, we consider only the decrease from the center to  $\sim 0.1 r_e$  to be significant. Deeper observations are needed to trace with higher confidence the EW out to larger radii. Some galaxies deviate from the general trend, either because they have a flatter emission profile (NGC 3489, NGC 7007, NGC 7377, NGC 5898), or because their emission is nuclear concentrated (IC 4296, NGC 4374, NGC 5090). Previous narrow-band imaging and integral field spectroscopy studies have revealed extended distribution for the ionized gas (Caldwell 1984; Goudfrooij et al. 1994b; Macchetto et al. 1996; Sarzi et al. 2006, 2009).

Extinction was derived from the observed H $\alpha$ /H $\beta$  flux ratio, assuming an intrinsic value of  $\approx 3.1$  for AGN-like objects (Osterbrock 1989). This choice was driven by our galaxies having AGN-like [NII]/H $\alpha$  ratios. For the majority of the galaxies, the derived  $E(B - V)$  values are lower than 0.3. Some galaxies however have very large reddenings, up to  $E(B - V) \sim 1.5$  or even more. Since the observed continuum is incompatible with these large values, our result suggests that in these galaxies the dust has a patchy distribution. This is consistent with narrow-band imaging studies that have detected dust lanes and patches in early-type galaxies (e.g. Goudfrooij et al. 1994b).

We performed a spectral classification for our sample using the classical [OIII]/H $\beta$  versus [NII]/H $\alpha$  diagnostic diagram (BPT diagram). The classification based on the central  $r < r_c/16$

emission lines is provided in Table 4. About 72% of the galaxies exhibit a central LINER emission activity. Seyferts account for  $\sim 9\%$  of the emission sample. However, only IC 5063 can be classified as a bona fide Seyfert galaxy. The other 4 Seyferts (NGC 3489, NGC 777, NGC 7007, and NGC 6958), have very large errors in [OIII]/H $\beta$  (because of the faint emission in H $\beta$ ), and the classification is less robust. We note however that NGC 3489 and NGC 777 were also classified as Seyferts by other authors (Ho et al. 1997b, Sarzi et al. 2006). Seven galaxies ( $\sim 12\%$  of the emission line sample) are “composites” (or transition objects): NGC 3258, NGC 4552, NGC 5193, NGC 5328, NGC 6721, NGC 6876, and IC 2006. They have [NII]/H $\alpha$  ratios intermediate between HII regions and LINERs/Seyferts. In our sample, these galaxies exhibit the weakest emission lines. For the remaining 7% of the emission-line galaxies, we cannot provide a classification, either because the lines are too weak, or because the spectra are too noisy.

We derive spatial trends in the emission line ratios: moving from the center toward annuli of increasing galactocentric distance, we detect a clear decrease in the [NII]/H $\alpha$  ratio. The decrease in [OIII]/H $\beta$  is less clear. It implies that galaxies classified as LINERs on the basis of their nuclear line ratios, would shift toward the region of “composites” if one were to consider the emission from more external regions. This could be interpreted as either a decrease in the nebular metallicity, or a progressive “softening” of the ionizing spectrum.

We have investigated possible relations between the central line emission properties and the host galaxy properties. The main results are:

1. Seyferts have young luminosity weighted ages ( $\lesssim 5$  Gyr), and are on average younger than LINERs. LINERs span a wide age range, from a few Gyrs to a Hubble time. “Composites” have ages older than 5 Gyr, at variance with the idea that they may originate from the combined contribution of AGN and star formation.
2. Excluding the Seyferts, the spread in the emission equivalent width ([NII], H $\alpha$ , or [OIII]) increases with the galaxy central velocity dispersion. Low- $\sigma$  galaxies have weak emission lines, while high- $\sigma$  galaxies exhibit both weak and strong emission lines. Equivalent widths of [NII] $\lambda 6584$  stronger than  $\sim 5 \text{ \AA}$  are found only in galaxies with  $\sigma_c > 200 \text{ km s}^{-1}$ .
3. If we consider only the high-emission subsample (H) (see Table 4), where the emission line ratios are more reliable, a positive correlation exists between the [NII]/H $\alpha$  ratio and  $\sigma_c$ .
4. Excluding the Seyferts, which have higher [OIII]/H $\beta$  and younger ages, no relation between the emission line ratios and the galaxy age, metallicity, or  $\alpha/\text{Fe}$  enhancement is found.

### 7.1. The AGN-starburst connection in Seyferts

The first result agrees with previous findings that LINERs are older than Seyferts (e.g., Kewley et al. 2006), and supports the idea that the star formation and the AGN phenomena coexist (Terlevich et al. 1990; Cid Fernandes & Terlevich 1995; Heckman et al. 1997; González Delgado et al. 2001; Kauffmann et al. 2003; Cid Fernandes et al. 2005; Davies et al. 2007; Riffel et al. 2009). The young luminosity-weighted ages in the Seyferts of our sample are probably caused by recent star formation episodes superimposed on a several Gyr old stellar population (see Paper III). Davies et al. (2007) provide evidence for a delay of 50–100 Myr between the onset of star formation and the subsequent fueling of the black hole. Given the short

duration of the AGN phenomenon ( $\lesssim 100$  Myr), this suggests that star formation has occurred a few hundreds Myr ago in the Seyfert galaxies of our sample. Because of the short duration of the AGN phase, we also expect to observe galaxies with relatively young luminosity-weighted ages but no signatures of current Seyfert activity. This agrees with the LINERs spanning a wide luminosity-weighted age range, from a few Gyr to a Hubble time.

## 7.2. The ionization mechanism in LINERs

Several studies have demonstrated that a minimum level of ionizing photons are produced in any evolved stellar systems. Thus, if cold gas is present, some level of nebular emission is always expected in early-type galaxies. However, the critical question is: can PAGB stars provide *all* the ionization observed in early-type galaxies? In answering this question, we should first of all distinguish between the central LINER activity and the more extended LINER-like emission. By means of the BPT classification carried out in annuli of increasing galactocentric distance, we have demonstrated that ETGs have both a central and an extended LINER-like emission. When comparing the stronger nuclear  $r < r_c/16$  emission with the results of the photoionization models from Binette et al. (1994), we have found that only 11 of the 49 galaxies classified as LINERs/composites in our sample (i.e. in  $\approx 22\%$  of the LINER/comp sample) can be explained with photoionization by old stars alone. Of these 11 galaxies, 6 are classified as LINERs and 5 as composites.

For the other 78% of LINERs/composites, some mechanism other than photoionization by PAGB stars must operate. We caution however that this fraction is very uncertain, since there is no precise description yet for the evolution and number of PAGB stars (e.g., Brown et al. 2008).

On the other hand, we cannot exclude the importance of hot old stars as a photoionization source at larger radii. The emission strength indeed progressively decreases toward larger galactocentric distances, so that an increasing number of LINERs become compatible with pure PAGB star photoionization.

*Summarizing, we cannot exclude a scenario in which more than a source of ionizing photons are present, with different roles at different radii. We can think of a transition region from the center, where PAGB stars fail in accounting alone for the ionizing photon budget, to more extended regions, where they may do well the job, in agreement with the findings of Sarzi et al. (2009) and Eracleous et al. (2010).*

Studies of LINERs based on large sample, such as the SDSS, were presented by Stasińska et al. (2008) and Cid Fernandes et al. (2009). However, we warn against direct comparisons of our findings with the results from SDSS for at least two reasons: the  $3''$ -wide aperture of the SDSS usually encompasses large kpc-scale regions where diffuse emission contribute to the nebular fluxes; and our sample is biased toward the presence of emission lines.

After ascertaining the limited role of PAGB stars in the nuclear LINER region, we investigated other possible scenarios, more specifically photoionization by sub-Eddington accretion rate AGN and fast shocks. Direct evidence of AGNs comes from the detection of compact nuclear X-ray/ radio sources. High resolution X-ray and/or radio data are available for 18 galaxies in our sample, 16 of which are classified as LINERs. Among the 16 LINERs, evidence of an AGN is found in 10. Even if the statistics are small, this result suggests that there is a low accretion rate AGNs in  $\sim 62\%$  of LINERs. However, the presence

of an AGN does not exclude the coexistence of shock heating: indeed, jet-driven flows and dissipative accretion disks in active galaxies with strongly sub-Eddington accretion have been proposed as possible sources of shocks (Dopita & Sutherland 1995; Dopita et al. 1997), and bubbles probably produced by an AGN outburst have been observed in LINERs (e.g. Baldi et al. 2009).

Both AGN and shock models reproduce the central emission line ratios in our sample. In the dusty AGN models of Groves et al. (2004), LINERs require a ionization parameter  $\log U < -3$ , significantly lower than for Seyferts. This is consistent with a scenario in which LINERs are AGNs accreting at a much lower rate than Seyferts. LINERs can also be modeled in terms of fast shocks ( $200\text{--}500 \text{ km s}^{-1}$ ) in a relatively gas poor environment (pre-shock densities  $n \approx 0.01\text{--}100 \text{ cm}^{-3}$ , depending on the magnetic field), with gas metallicity  $\sim$  solar. These low pre-shock densities are consistent with the observed  $[\text{SII}]6717/[\text{SII}]6731$  ratios. A critical point concerns the high shock velocities required to explain the emission-line spectrum in LINERs. Jet-driven flows or accretion onto a massive BH may well produce these velocities (Nagar et al. 2005; Dopita et al. 1997). We suppose that an alternative source of mechanical energy comes from turbulent motion of gas clouds, either injected by stellar mass loss or accreted, within the potential well of the galaxy. This scenario cannot be excluded since several studies have found a gaseous component of high velocity dispersion, in the range  $150\text{--}250 \text{ km s}^{-1}$ , in the center of early-type galaxies (e.g. Bertola et al. 1995; Zeilinger et al. 1996; Sarzi et al. 2006), which translates into higher intrinsic 3D velocity dispersions. This scenario is very appealing since it would naturally explain the observed trends between the emission strength, and the  $[\text{NII}]/\text{H}\alpha$  ratio, with the galaxy stellar central velocity dispersion.

A solid result from our study is that the  $[\text{NII}]/\text{H}\alpha$  ratio decreases with increasing galacto-centric distance. This trend may reflect metallicity gradients in the gas, similarly to what is observed for the stars. However, this is difficult to reproduce in a scenario in which the gas has an external origin (see Sect. 7.3). If not caused by metallicity variations, the  $[\text{NII}]/\text{H}\alpha$  gradient should reflect variations in the properties of the ionization mechanism. In the shock scenario, this requires decreasing shock velocities with increasing galactocentric distances. Unfortunately, we lack the spectral resolution necessary to determine the gas velocity dispersion and, ultimately, to ascertain the presence of a radial gradient in the shock velocity.

A large fraction (40/65) of our sample was observed with *Spitzer*-IRS. In a forthcoming paper, we will use MIR ionic and molecular emission lines, and polycyclic aromatic hydrocarbon features, to investigate the powering mechanism in LINERs, and more clearly distinguish the contributions from AGN photoionization and shock heating.

## 7.3. Origin of the gas

We derived the oxygen abundance using two calibrations present in the literature: the Kobulnicky et al. (1999) calibration, valid for HII regions, and the Storch-Bergmann et al. (1998) calibration, based on the assumption of photoionization by a typical AGN continuum (Mathews & Ferland 1987). The first approach was also adopted by Athey & Bregman (2009) to derive nebular metallicities in 7 early-type galaxies, and is probably reasonable in the case of photoionization by PAGB stars. The second calibration is valid in the case of AGN excitation, and may be reasonable if LINERs are low-accretion rate AGNs. Our result is the following: irrespective of the adopted calibration, the nebular oxygen metallicities are significantly lower than the stellar ones.

The main caveat is that power-law ionizing spectra tend to provide abundances up to  $\sim 0.5$  dex higher than a typical AGN continuum. A calibration in the case of shock heating is not available in the literature. However, we can see that shock models indicate nebular metallicities not higher than solar in our sample, in agreement with the results obtained with the Kobulnicky et al. (1999) and Storch-Bergmann et al. (1998) calibrations.

Our result has an important implication for the origin of the gas, suggesting that it may be at least in part of external origin (e.g., from either a cooling flow or accretion from a companion galaxy). This is in agreement with photometric and kinematical studies in ETGs showing in many cases gas/star misalignment and gas/star angular momentum decoupling (Bertola et al. 1992; van Dokkum & Franx 1995; Caon et al. 2000; Sarzi et al. 2006). Kinematical and morphological peculiarities are present in 50% of our sample, suggesting that accretion is frequent. Accretion of fresh gas can feed the central supermassive BH, and activate the AGN emission. This is consistent with a major fraction of our galaxies studied in the X-ray and/or radio containing nuclear compact sources.

Finally, we cannot exclude that the low oxygen abundance is unrelated to the gas origin, and reflects that oxygen does not vary on lockstep with the other  $\alpha$ -elements. In a survey of 27 Milky Way bulge giants, Fulbright et al. (2006) found that, although Mg appears to be enhanced at all [Fe/H], [O/Fe] declines with increasing [Fe/H] and is solar or mildly sub-solar at [Fe/H]  $\geq 0$ . X-ray studies have also derived subsolar [O/Fe] values, but supersolar [Mg/Fe] values, in the hot gas of elliptical galaxies (e.g., Humphrey & Buote 2006; Ji et al. 2009). This may be evidence of an overestimate of O yield by SNII models, which do not consider significant mass loss at the late evolutionary stages of massive progenitor stars (Ji et al. 2009).

*Acknowledgements.* We acknowledge a financial contribution from contract ASI-INAF I/016/07/0. F. A. thanks R. van der Marel for useful suggestions. We thank the anonymous referee for having carefully read the manuscript, and for his/her useful comments and suggestions that helped to improve significantly the paper.

## References

- Allen, M. G., Groves, B. A., Dopita, M. A., Sutherland, R. S., & Kewley, L. J. 2008, *ApJS*, 178, 20
- Annibali, F., Bressan, A., Rampazzo, R., & Zeilinger, W. W. 2006, *A&A*, 445, 79
- Annibali, F., Bressan, A., Rampazzo, R., Zeilinger, W. W., & Danese, L. 2007, *A&A*, 463, 455
- Arimoto, N., Matsushita, K., Ishimaru, Y., Ohashi, T., & Renzini, A. 1997, *ApJ*, 477, 128
- Athey, A. E., & Bregman, J. N. 2009, *ApJ*, 696, 681
- Baldi, A., Forman, W., Jones, C., et al. 2009, [[arXiv:0909.2942](https://arxiv.org/abs/0909.2942)]
- Baldwin, J. A., Phillips, M. M., & Terlevich, R. 1981, *PASP*, 93, 5
- Balmaverde, B., & Capetti, A. 2006, *A&A*, 447, 97
- Bertelli, G., Bressan, A., Chiosi, C., Fagotto, F., & Nasi, E. 1994, *A&AS*, 106, 275
- Bertola, F., Buson, L. M., & Zeilinger, W. W. 1992, *ApJ*, 401, L79
- Bertola, F., Cinzano, P., Corsini, E. M., Rix, H.-W., & Zeilinger, W. W. 1995, *ApJ*, 448, L13
- Binette, L., Magris, C. G., Stasińska, G., & Bruzual, A. G. 1994, *A&A*, 292, 13
- Blanton, E. L., Sarazin, C. L., & Irwin, J. A. 2001, *ApJ*, 552, 106
- Bregman, J. N., Hogg, D. E., & Roberts, M. S. 1992, *ApJ*, 387, 484
- Bressan, A., Granato, G. L., & Silva, L. 1998, *A&A*, 332, 135
- Bressan, A., Panuzzo, P., Buson, L., et al. 2006, *ApJ*, 639, L55
- Brown, T. M., Smith, E., Ferguson, H. C., et al. 2008, *ApJ*, 682, 319
- Buote, D. A., Lewis, A. D., Brighenti, F., & Mathews, W. G. 2003, *ApJ*, 595, 151
- Buson, L. M., Sadler, E. M., Zeilinger, W. W., et al. 1993, *A&A*, 280, 409
- Caffau, E., Ludwig, H.-G., Steffen, M., et al. 2008, *A&A*, 488, 1031
- Caffau, E., Maiorca, E., Bonifacio, P., et al. 2009, *A&A*, 498, 877
- Caldwell, N. 1984, *PASP*, 96, 287
- Caon, N., Macchetto, D., & Pastoriza, M. 2000, *ApJS*, 127, 39
- Cappellari, M., Emsellem, E., Bacon, R., Bureau, M., & Davies, R. L. 2008, *MNRAS*, 379, 418
- Cardelli, J. A., Clayton, G. C., & Mathis, J. S. 1989, *ApJ*, 345, 245
- Cecil, G., Greenhill, L. J., DePree, C. G., et al. 2000, *ApJ*, 536, 675
- Chavez, M., Bertone, E., Morales-Hernandez, J., & Bressan, A. 2009, *ApJ*, 700, 694
- Cid Fernandes, R. J., & Terlevich, R. 1995, *MNRAS*, 272, 423
- Cid Fernandes, R., González Delgado, R. M., Storch-Bergmann, T., Martins, L. P., & Schmitt, H. 2005, *MNRAS*, 356, 270
- Cid Fernandes, R., Schlickmann, M., Stasinska, G., et al. 2009, *ASP Conf. Ser.*, 408, 122
- Clemens, M. S., Bressan, A., Nikolic, B., & Rampazzo, R. 2009, *MNRAS*, 392, L35
- Corsini, E. M., & Bertola, F. 1998, *Journal of the Korean Physical Society*, 33, 574
- Crawford, C. S., & Fabian, A. C. 1992, *MNRAS*, 259, 265
- Davies, R. L., Efstathiou, G., Fall, S. M., Illingworth, G., & Schechter, P. L. 1983, *ApJ*, 266, 41
- Davies, R. L., Sánchez, F. M., Genzel, R., et al. 2007, *ApJ*, 671, 1388
- de Jong, T., Norgaard-Nielsen, H. U., Jorgensen, H. E., & Hansen, L. 1990, *A&A*, 232, 317
- Demoulin-Ulrich, M.-H., Butcher, H. R., & Boksenberg, A. 1984, *ApJ*, 285, 527
- de Vaucouleurs, G., de Vaucouleurs, A., Corwin, H. G., Jr., et al. 1991, *S&T*, 82, 621
- Domingue, D. L., Sulentic, J. W., Xu, C., et al. 2003, *AJ*, 125, 555
- Dopita, M. A., & Evans, I. N. 1986, *ApJ*, 307, 431
- Dopita, M. A., & Sutherland, R. S. 1995, *ApJ*, 455, 468
- Dopita, M. A., Binette, L., & Schwartz, R. D. 1982, *ApJ*, 261, 183
- Dopita, M. A., Koratkar, A. P., Allen, M. G., et al. 1997, *ApJ*, 490, 202
- Edmunds, M. G., & Pagel, B. E. J. 1984, *MNRAS*, 211, 507
- Emsellem, E., Goudfrooij, P., & Ferruit, P. 2003, *MNRAS*, 345, 1297
- Emsellem, E., Cappellari, M., Peletier, R. F., McDermid, R. M., & Bacon, R. 2004, *MNRAS*, 352, 721
- Emsellem, E., Cappellari, M., Krajnović, D., van de Ven, G., Bacon, R., et al. 2007, *MNRAS*, 379, 401.
- Eracleous, M., Hwang, J. A., & Flohic, H. M. L. G. 2010, *ApJ*, 711, 796
- Fabbiano, G., Kim, D.-W., & Trinchieri, G. 1992, *ApJS*, 80, 531
- Filho, M. E., Fraternali, F., Markoff, S., et al. 2004, *A&A*, 418, 429
- Filho, M. E., Barthel, P. D., & Ho, L. C. 2006, *A&A*, 451, 71
- Forman, W., & Jones, C. 1985, *BAAS*, 17, 586
- Fosbury, R. A. E., Mebold, U., Goss, W. M., & Dopita, M. A. 1978, *MNRAS*, 183, 549
- Flohic, H. M. L. G., Eracleous, M., Chartas, G., Shields, J. C., & Moran, E. C. 2006, *ApJ*, 647, 140
- Fulbright, J. P., Rich, R. M., & McWilliam, A. 2006, *Chemical Abundances and Mixing in Stars in the Milky Way and its Satellites*, *ESO Astrophys. Symp.* (Springer-Verlag), 93, 93
- Gastaldello, F., & Molendi, S. 2002, *ApJ*, 572, 160
- González Delgado, R. M., Heckman, T., & Leitherer, C. 2001, *ApJ*, 546, 845
- Gonzalez-Martín, O., Masegosa, J., Marquez, I., Guainazzi, M., & Jimenez-Bailon, E. 2009, *A&A*, 506, 1107
- Goudfrooij, P. 1999, *Star Formation in Early Type Galaxies*, 163, 55
- Goudfrooij, P., & de Jong, T. 1995, *A&A*, 298, 784
- Goudfrooij, P., & Emsellem, E. 1996, *A&A*, 306, L45
- Goudfrooij, P., Hansen, L., Jorgensen, H. E., et al. 1994a, *A&AS*, 104, 179
- Goudfrooij, P., Hansen, L., Jorgensen, H. E., & Norgaard-Nielsen, H. U. 1994b, *A&AS*, 105, 341
- Goudfrooij, P., de Jong, T., Hansen, L., & Norgaard-Nielsen, H. U. 1994c, *MNRAS*, 271, 833
- Groves, B. A., Dopita, M. A., & Sutherland, R. S. 2004, *ApJS*, 153, 9
- Grützbauch, R., Trinchieri, G., Rampazzo, R., et al. 2007, *AJ*, 133, 220
- Heckman, T. M. 1980, *A&A*, 87, 152
- Heckman, T. M., Gonzalez-Delgado, R., Leitherer, C., et al. 1997, *ApJ*, 482, 114
- Heckman, T. M., Kauffmann, G., Brinchmann, J., et al. 2004, *ApJ*, 613, 109
- Helmboldt, J. F. 2007, *MNRAS*, 379, 1227
- Ho, L. 1999a, *Observational Evidence for the Black Holes in the Universe*, 234, 157
- Ho, L. C. 1999b, *Adv. Space Res.*, 23, 813
- Ho, L. C. 2009a, *ApJ*, 699, 626
- Ho, L. C. 2009b, *ApJ*, 699, 638
- Ho, L. C., & Ulvestad, J. S. 2001, *ApJS*, 133, 77
- Ho, L. C., Filippenko, A. V., Sargent, W. L. W., & Peng, C. Y. 1997a, *ApJS*, 112, 391
- Ho, L. C., Filippenko, A. V., & Sargent, W. L. W. 1997b, *ApJS*, 112, 315
- Ho, L. C., Filippenko, A. V., & Sargent, W. L. W. 1997c, *ApJ*, 487, 591
- Humphrey, P. J., & Buote, D. A. 2006, *ApJ*, 639, 136

- Ji, J., Irwin, J. A., Athey, A., Bregman, J. N., & Lloyd-Davies, E. J. 2009, *ApJ*, 696, 2252
- Jones, C., Forman, W., Vikhlinin, A., et al. 2002, *ApJ*, 567, L115
- Kauffmann, G., Heckman, T. M., Tremonti, C., et al. 2003, *MNRAS*, 346, 1055
- Kewley, L. J., Dopita, M. A., Sutherland, R. S., Heisler, C. A., & Trevena, J. 2001, *ApJ*, 556, 121
- Kewley, L. J., Groves, B., Kauffmann, G., & Heckman, T. 2006, *MNRAS*, 372, 961
- Kim, D.-W. 1989, *ApJ*, 346, 653
- Kobulnicky, H. A., Kennicutt, R. C., Jr., Pizagno, & James, L. 1999, *ApJ*, 514, 544 (Kob99)
- Kormendy, J. 2004, *Coevolution of Black Holes and Galaxies*, 1
- Koski, A. T., & Oosterbrock, D. E. 1976, *ApJ*, 203, L49
- Koyama, K., Awaki, H., Iwasawa, K., & Ward, M. J. 1992, *ApJ*, 399, L129
- Lípari, S., Mediavilla, E., García-Lorenzo, B., et al. 2004, *MNRAS*, 355, 641
- Macchetto, F., Pastoriza, M., Caon, N., et al. 1996, *A&AS*, 120, 463
- Machacek, M. E., Nulsen, P., Stirbat, L., Jones, C., & Forman, W. R. 2005, *ApJ*, 630, 280
- Magorrian, J., Tremaine, S., Richstone, D., et al. 1998, *AJ*, 115, 2285
- Malin, D. F., & Carter, D. 1983, *ApJ*, 274, 534
- Maoz, D., Nagar, N. M., Falcke, H., & Wilson, A. S. 2005, *ApJ*, 625, 699
- Martel, A. R., Ford, H. C., Bradley, L. D., et al. 2004, *AJ*, 128, 2758
- Mathews, W. G., & Ferland, G. J. 1987, *ApJ*, 323, 456
- McCall, M. L., Rybski, P. M., & Shields, G. A. 1985, *ApJS*, 57, 1
- McGaugh, S. S. 1991, *ApJ*, 380, 140
- Merrifield, M. R., Gerssen, J., & Kuijken, K. 2001, *Galaxy Disks and Disk Galaxies*, 230, 221
- Morganti, R., de Zeeuw, P. T., Oosterloo, T. A., et al. 2006, *MNRAS*, 371, 157
- Nagar, N. M., Wilson, A. S., & Falcke, H. 2001, *ApJ*, 559, L87
- Nagar, N. M., Falcke, H., Wilson, A. S., & Ulvestad, J. S. 2002, *A&A*, 392, 53
- Nagar, N. M., Falcke, H., & Wilson, A. S. 2005, *A&A*, 435, 521
- Oosterbrock, D. E. 1989, *S&T*, 78, 491
- Oosterloo, T. A., Morganti, R., Sadler, E. M., van der Hulst, T., & Serra, P. 2007, *A&A*, 465, 787
- O'Sullivan, E., Forbes, D. A., & Ponman, T. J. 2001, *MNRAS*, 328, 461
- Pagal, B. E. J., Edmunds, M. G., Blackwell, D. E., Chun, M. S., & Smith, G. 1979, *MNRAS*, 189, 95
- Panuzzo, P., Vega, O., Bressan, A., et al. 2007, *ApJ*, 656, 206
- Pellegrini, S., Venturi, T., Comastri, A., et al. 2003, *ApJ*, 585, 677
- Phillips, M. M., Jenkins, C. R., Dopita, M. A., Sadler, E. M., & Binette, L. 1986, *AJ*, 91, 1062
- Pian, E., Romano, P., Maoz, D., et al. 2010, *MNRAS*, 401, 677
- Pierfederici, F., & Rampazzo, R. 2004, *AN*, 325, 359
- Quataert, E. 2001, *Probing the Physics of Active Galactic Nuclei*, 224, 71
- Rampazzo, R., Annibali, F., Bressan, A., et al. 2005, *A&A*, 433, 497
- Rand, R. J., & Kulkarni, S. R. 1989, *ApJ*, 343, 760
- Riffel, R. A., Storchi-Bergmann, T., Dors, O. L., & Winge, C. 2009, *MNRAS*, 393, 783
- Roberts, M. S., Hogg, D. E., Bregman, J. N., Forman, W. R., & Jones, C. 1991, *ApJS*, 75, 751
- Sadler, E. M., & Gerhard, O. E. 1985, *MNRAS*, 214, 177
- Sadler, E. M., Oosterloo, T., & Morganti, R. 2002, *The Dynamics, Structure & History of Galaxies: A Workshop in Honour of Professor Ken Freeman*, ASP Conf. Proc., 273, ed. G. S. Da Costa, & H. Jerjen
- Sage, L. J., & Welch, G. A. 2006, *ApJ*, 644, 850
- Sánchez-Blázquez, P., Peletier, R. F., Jiménez-Vicente, J., et al. 2006, *MNRAS*, 371, 703
- Sandage, A., & Tammann, G. A. 1987, *Carnegie Institution of Washington Publication*, Washington: Carnegie Institution, 2nd edn
- Saraiva, M. F., Bica, E., Pastoriza, M. G., & Bonatto, C. 2001, *A&A*, 376, 43
- Sarzi, M., F.-B., Jesús, Davies, R. L., et al. 2006, *MNRAS*, 366, 1151
- Sarzi, M., et al. 2009 [arXiv:0912.0275]
- Serra, P., Trager, S. C., Oosterloo, T. A., & Morganti, R. 2008, *A&A*, 483, 57
- Shaw, R. A., & Dufour, R. J. 1995, *PASP*, 107, 896
- Sparks, W. B., Macchetto, F., & Golombek, D. 1989, *ApJ*, 345, 153
- Stasińska, G., Cid Fernandes, R., Mateus, A., Sodr e, L., & Asari, N. V. 2006, *MNRAS*, 371, 972
- Stasińska, G., Vale Asari, N., Cid Fernandes, R., et al. 2008, *MNRAS*, 391, L29
- Storchi-Bergmann, T., Schmitt, H. R., Calzetti, D., & Kinney, A. L. 1998, *AJ*, 115, 909 (SB98)
- Sutherland, R. S., & Dopita, M. A. 1993, *ApJS*, 88, 253
- Tal, T., van Dokkum, P. G., Nelan, J., & Bezanson, R. 2009, *AJ*, 138, 1417
- Tamura, T., Kaastra, J. S., Makishima, K., & Takahashi, I. 2003, *A&A*, 399, 497
- Tem, P., Brighenti, F., Mathews, W. G., & Bregman, J. D. 2004, *ApJS*, 151, 237
- Terashima, Y. 1999, *Adv. Space Res.*, 23, 851
- Terashima, Y., Ho, L. C., & Ptak, A. F. 2000, *ApJ*, 539, 161
- Terlevich, E., Díaz, A. I., & Terlevich, R. 1990, *Rev. Mex. Astron. Astrofis*, 21, 218
- Thomas, D., Maraston, C., Bender, R., & Mendes de Oliveira, C. 2005, *ApJ*, 621, 673
- Tran, H. D., Tsvetanov, Z., Ford, H. C., et al. 2001, *AJ*, 121, 2928
- Trinchieri, G., & di Serego Alighieri, S. 1991, *AJ*, 101, 1647
- Tully, R. B. 1988, *Nearby Galaxy Catalog* (Cambridge University Press)
- Yan, R., Newman, J. A., Faber, S. M. 2006, *ApJ*, 648, 281
- Zaritsky, D., Kennicutt, R. C. Jr., & Huchra, J. P. 1994, *ApJ*, 420, 87
- Zeilinger, W. W., Pizzella, A., Amico, P., Bertin, G., et al. 1996, *A&AS*, 120, 257
- van Dokkum, P. G., & Franx, M. 1995, *AJ*, 110, 2027
- Wang, J., & Wei, J. Y. 2008, *ApJ*, 679, 86

Table 2. Observed emission line fluxes in units of  $10^{-16}$  erg  $s^{-1}$   $cm^{-2}r^{-2}$ .

Galaxy	Reg <sup>4</sup>	$E(B-V)$	[O III] <sup>5</sup> λ3727	[Ne III] λ3869	H $\beta$ λ4861	[O III] λ4959	[O III] λ5007	[O I] λ6300	[N II] λ6548	H $\alpha$ λ6563	[N II] λ6584	[S II] λ6717	[S II] λ6731
NGC 128	1	0.26 ± 0.29	6.77 ± 0.55	0.40 ± 0.55	1.76 ± 0.50	1.35 ± 0.20	2.71 ± 0.25	0.99 ± 0.06	2.96 ± 0.16	7.13 ± 0.34	8.72 ± 0.10	2.70 ± 0.23	1.51 ± 0.18
NGC 128	2	0.03 ± 0.28	5.87 ± 0.49	0.07 ± 0.44	1.68 ± 0.45	0.85 ± 0.15	1.96 ± 0.19	0.51 ± 0.09	2.29 ± 0.17	5.26 ± 0.30	6.02 ± 0.04	2.16 ± 0.19	1.64 ± 0.18
NGC 128	3	0.15 ± 0.41	2.96 ± 0.34	-0.06 ± 0.31	0.74 ± 0.30	0.48 ± 0.08	1.02 ± 0.11	-0.67 ± 0.06	1.09 ± 0.11	2.68 ± 0.20	2.99 ± 0.04	1.07 ± 0.12	0.98 ± 0.12
NGC 128	4	0.03 ± 0.46	0.62 ± 0.15	-0.09 ± 0.15	0.39 ± 0.17	0.22 ± 0.05	0.35 ± 0.06	0.57 ± 0.03	0.46 ± 0.05	0.76 ± 0.10	-0.12 ± 0.01	0.36 ± 0.07	0.39 ± 0.07
NGC 777 <sup>6</sup>	1	2.81 ± 3.53	0.89 ± 0.16	0.13 ± 0.23	0.03 ± 0.12	-0.03 ± 0.00	1.14 ± 0.07	0.81 ± 0.02	1.13 ± 0.12	1.71 ± 0.05	1.51 ± 0.02	7.44 ± 0.13	-
NGC 777 <sup>6</sup>	2	0.52 ± 0.71	0.46 ± 0.10	-0.21 ± 0.15	0.16 ± 0.12	-0.09 ± 0.05	0.67 ± 0.08	0.15 ± 0.03	0.65 ± 0.09	0.85 ± 0.04	0.58 ± 0.01	3.82 ± 0.09	-
NGC 777 <sup>6</sup>	3	0.05 ± 0.24	0.20 ± 0.04	-0.14 ± 0.04	0.14 ± 0.03	-0.00 ± 0.00	0.23 ± 0.02	0.16 ± 0.02	0.09 ± 0.01	0.35 ± 0.01	0.17 ± 0.00	1.74 ± 0.01	-
NGC 777 <sup>6</sup>	4	0.05 ± 0.94	0.13 ± 0.04	-0.01 ± 0.05	-0.04 ± 0.04	0.02 ± 0.01	0.06 ± 0.02	0.13 ± 0.01	0.04 ± 0.01	0.07 ± 0.02	0.00 ± 0.00	0.43 ± 0.01	-
NGC 1052	1	0.22 ± 0.04	88.41 ± 0.87	10.79 ± 1.11	29.21 ± 1.18	15.98 ± 0.55	73.78 ± 0.64	53.41 ± 0.45	49.57 ± 0.94	112.80 ± 0.94	109.76 ± 0.55	67.68 ± 1.16	60.98 ± 0.99
NGC 1052	2	0.38 ± 0.09	30.98 ± 0.76	2.71 ± 0.54	7.68 ± 0.65	8.54 ± 0.56	19.70 ± 0.39	13.29 ± 0.20	15.98 ± 0.42	34.57 ± 0.53	32.99 ± 0.18	23.96 ± 0.44	17.44 ± 0.32
NGC 1052	3	0.24 ± 0.20	6.71 ± 0.32	0.53 ± 0.28	1.37 ± 0.27	0.74 ± 0.09	2.52 ± 0.13	1.59 ± 0.07	1.98 ± 0.13	5.38 ± 0.18	4.67 ± 0.04	3.62 ± 0.15	2.62 ± 0.12
NGC 1052	4	0.03 ± 0.45	0.60 ± 0.14	0.04 ± 0.19	0.29 ± 0.13	0.07 ± 0.06	0.31 ± 0.08	0.00 ± 0.01	0.34 ± 0.04	0.71 ± 0.08	0.35 ± 0.01	0.25 ± 0.05	0.21 ± 0.03
NGC 1209	1	0.04 ± 0.23	12.74 ± 0.96	-0.39 ± 0.96	3.74 ± 0.85	2.04 ± 0.30	4.82 ± 0.37	1.10 ± 0.17	5.46 ± 0.28	9.39 ± 0.46	14.21 ± 0.09	4.69 ± 0.36	3.94 ± 0.31
NGC 1209	2	0.04 ± 0.24	7.80 ± 0.71	-0.57 ± 0.84	3.10 ± 0.71	1.72 ± 0.22	3.52 ± 0.29	0.91 ± 0.13	3.43 ± 0.19	6.34 ± 0.36	9.02 ± 0.11	2.41 ± 0.25	2.36 ± 0.22
NGC 1209	3	0.04 ± 0.25	2.83 ± 0.47	-0.63 ± 0.63	1.79 ± 0.43	0.80 ± 0.22	1.21 ± 0.28	0.53 ± 0.04	1.08 ± 0.11	2.63 ± 0.21	3.07 ± 0.05	0.73 ± 0.14	0.75 ± 0.11
NGC 1209	4	0.04 ± 0.52	0.14 ± 0.18	-0.13 ± 0.26	0.35 ± 0.17	0.31 ± 0.10	0.31 ± 0.18	0.13 ± 0.03	0.26 ± 0.04	0.42 ± 0.09	0.43 ± 0.02	-0.04 ± 0.05	-0.00 ± 0.04
NGC 1297	1	0.52 ± 0.52	3.74 ± 0.43	0.16 ± 0.51	0.67 ± 0.34	0.64 ± 0.19	1.35 ± 0.24	0.64 ± 0.06	1.38 ± 0.10	3.49 ± 0.23	3.04 ± 0.04	2.07 ± 0.15	1.91 ± 0.11
NGC 1297	2	0.06 ± 0.44	1.30 ± 0.17	-0.01 ± 0.25	0.40 ± 0.17	0.34 ± 0.10	0.74 ± 0.15	0.41 ± 0.04	0.59 ± 0.04	1.33 ± 0.10	1.08 ± 0.02	0.77 ± 0.06	0.64 ± 0.04
NGC 1297	3	0.03 ± 0.50	0.42 ± 0.08	0.07 ± 0.10	0.18 ± 0.09	0.19 ± 0.05	0.19 ± 0.05	0.04 ± 0.02	0.19 ± 0.02	0.36 ± 0.05	0.24 ± 0.01	0.14 ± 0.03	0.11 ± 0.01
NGC 1297	4	1.00 ± 1.83	0.08 ± 0.02	0.03 ± 0.04	0.03 ± 0.04	0.03 ± 0.02	0.07 ± 0.02	0.09 ± 0.01	0.14 ± 0.01	0.22 ± 0.02	-0.23 ± 0.00	0.18 ± 0.01	0.04 ± 0.01
NGC 1380	1	0.25 ± 0.35	3.20 ± 0.84	-0.58 ± 0.86	2.31 ± 0.80	1.23 ± 0.25	3.41 ± 0.39	1.85 ± 0.16	5.32 ± 0.31	9.21 ± 0.47	12.32 ± 0.11	3.49 ± 0.37	3.55 ± 0.40
NGC 1380	2	0.51 ± 0.47	2.86 ± 0.70	0.00 ± 0.73	1.45 ± 0.68	0.76 ± 0.20	2.13 ± 0.29	0.94 ± 0.15	3.09 ± 0.22	7.44 ± 0.37	8.29 ± 0.10	2.73 ± 0.29	1.98 ± 0.25
NGC 1380	3	0.44 ± 0.49	1.52 ± 0.45	-0.10 ± 0.50	0.91 ± 0.44	-0.02 ± 0.06	1.02 ± 0.22	0.59 ± 0.11	1.69 ± 0.14	4.38 ± 0.26	4.66 ± 0.05	1.80 ± 0.18	1.16 ± 0.16
NGC 1380	4	0.02 ± 0.44	0.47 ± 0.23	0.01 ± 0.32	0.61 ± 0.26	0.03 ± 0.10	0.62 ± 0.15	0.01 ± 0.02	0.93 ± 0.07	1.64 ± 0.13	1.63 ± 0.03	0.55 ± 0.09	0.26 ± 0.07
NGC 1453	1	0.11 ± 0.19	10.06 ± 0.51	0.08 ± 0.42	2.72 ± 0.52	1.72 ± 0.24	3.93 ± 0.27	1.42 ± 0.12	4.37 ± 0.23	9.21 ± 0.31	12.56 ± 0.05	6.28 ± 0.29	4.89 ± 0.26
NGC 1453	2	0.11 ± 0.21	5.37 ± 0.39	-0.14 ± 0.38	1.88 ± 0.38	1.35 ± 0.13	2.59 ± 0.17	0.59 ± 0.07	2.45 ± 0.14	4.96 ± 0.23	6.10 ± 0.04	2.65 ± 0.18	2.40 ± 0.20
NGC 1453	3	0.11 ± 0.23	1.39 ± 0.16	-0.17 ± 0.21	0.75 ± 0.17	0.54 ± 0.06	0.98 ± 0.09	0.09 ± 0.02	0.58 ± 0.06	1.34 ± 0.10	1.43 ± 0.02	0.40 ± 0.06	0.59 ± 0.07
NGC 1453	4	0.11 ± 0.29	0.43 ± 0.06	-0.03 ± 0.09	0.21 ± 0.06	0.09 ± 0.03	0.36 ± 0.07	-0.00 ± 0.02	0.15 ± 0.02	0.44 ± 0.03	0.40 ± 0.01	0.14 ± 0.02	0.08 ± 0.02
NGC 1521 <sup>6</sup>	1	1.22 ± 1.51	0.80 ± 0.40	0.04 ± 0.63	0.24 ± 0.36	0.51 ± 0.12	0.49 ± 0.23	-0.00 ± 0.03	1.16 ± 0.14	2.54 ± 0.25	3.27 ± 0.06	0.56 ± 0.22	0.46 ± 0.19
NGC 1521 <sup>6</sup>	2	0.30 ± 1.20	0.54 ± 0.37	0.05 ± 0.59	0.30 ± 0.36	0.07 ± 0.18	0.17 ± 0.28	-0.01 ± 0.02	0.33 ± 0.09	1.26 ± 0.19	1.40 ± 0.05	0.48 ± 0.09	0.28 ± 0.07
NGC 1521 <sup>6</sup>	3	0.04 ± 8.66	0.32 ± 0.17	-0.29 ± 0.27	-0.02 ± 0.18	-0.01 ± 0.10	0.14 ± 0.15	0.00 ± 0.01	0.42 ± 0.04	0.29 ± 0.09	0.52 ± 0.03	0.10 ± 0.04	0.09 ± 0.04
NGC 1521 <sup>6</sup>	4	0.04 ± 0.77	0.04 ± 0.05	-0.06 ± 0.08	0.08 ± 0.06	0.08 ± 0.04	0.22 ± 0.06	0.03 ± 0.01	-0.01 ± 0.01	0.14 ± 0.04	0.10 ± 0.01	0.01 ± 0.01	0.01 ± 0.01
NGC 1533	1	0.01 ± 0.24	9.45 ± 1.24	0.43 ± 0.76	4.77 ± 1.13	2.71 ± 0.40	7.99 ± 0.47	3.88 ± 0.19	6.02 ± 0.32	12.56 ± 0.63	13.90 ± 0.09	4.66 ± 0.42	3.82 ± 0.38
NGC 1533	2	0.01 ± 0.23	4.99 ± 0.70	-0.42 ± 0.80	2.94 ± 0.65	1.31 ± 0.23	3.54 ± 0.30	1.23 ± 0.13	2.06 ± 0.17	4.71 ± 0.36	4.70 ± 0.08	1.62 ± 0.24	1.34 ± 0.20
NGC 1533	3	0.01 ± 0.30	2.54 ± 0.32	0.01 ± 0.39	1.01 ± 0.28	0.83 ± 0.12	1.90 ± 0.18	0.29 ± 0.06	0.56 ± 0.07	1.72 ± 0.15	1.37 ± 0.03	0.88 ± 0.10	0.65 ± 0.08
NGC 1533	4	0.01 ± 0.45	0.62 ± 0.11	-0.01 ± 0.14	0.18 ± 0.08	0.17 ± 0.05	0.30 ± 0.04	0.01 ± 0.01	0.16 ± 0.02	0.50 ± 0.05	0.39 ± 0.01	0.33 ± 0.03	0.17 ± 0.02

Notes. <sup>(4)</sup> Reg 1 =  $r \leq r_c/16$ ; Reg 2 =  $r_c/16 < r \leq r_c/8$ ; Reg 3 =  $r_c/8 < r \leq r_c/4$ ; Reg 4 =  $r_c/4 < r \leq r_c/2$ . <sup>(5)</sup> Negative emission values are consistent with no emission. <sup>(6)</sup> The continuum was fitted with 2 SSPs.

Table 3. Observed emission line equivalent widths.

Galaxy	Reg <sup>7</sup>	[O II] <sup>8</sup> λ3727	[Ne III] λ3869	Hβ λ4861	[O III] λ4959	[O III] λ5007	[O I] λ6300	[N II] λ6548	Hγ λ6563	[N II] λ6584	[S II] λ6717	[S II] λ6731
NGC 128	1	7.25 ± 0.59	0.59 ± 0.81	0.57 ± 0.16	0.43 ± 0.06	0.87 ± 0.08	0.27 ± 0.02	0.74 ± 0.04	1.78 ± 0.09	2.18 ± 0.03	0.73 ± 0.06	0.41 ± 0.05
NGC 128	2	7.13 ± 0.59	0.13 ± 0.75	0.64 ± 0.17	0.32 ± 0.05	0.73 ± 0.07	0.17 ± 0.03	0.69 ± 0.05	1.58 ± 0.09	1.81 ± 0.01	0.71 ± 0.06	0.54 ± 0.06
NGC 128	3	5.00 ± 0.58	-0.15 ± 0.74	0.40 ± 0.16	0.25 ± 0.04	0.54 ± 0.06	-0.31 ± 0.03	0.48 ± 0.05	1.18 ± 0.09	1.32 ± 0.02	0.51 ± 0.06	0.47 ± 0.06
NGC 128	4	1.92 ± 0.48	-0.41 ± 0.68	0.39 ± 0.17	0.22 ± 0.05	0.34 ± 0.06	0.51 ± 0.03	0.38 ± 0.04	0.62 ± 0.08	-0.10 ± 0.01	0.32 ± 0.06	0.34 ± 0.06
NGC 777 <sup>9</sup>	1	1.36 ± 0.24	0.27 ± 0.50	0.01 ± 0.04	-0.01 ± 0.00	0.42 ± 0.03	0.27 ± 0.01	0.36 ± 0.04	0.54 ± 0.02	0.47 ± 0.01	2.53 ± 0.05	-
NGC 777 <sup>9</sup>	2	1.16 ± 0.25	-0.71 ± 0.50	0.11 ± 0.08	-0.06 ± 0.03	0.47 ± 0.06	0.09 ± 0.02	0.37 ± 0.05	0.49 ± 0.02	0.33 ± 0.01	2.38 ± 0.06	-
NGC 777 <sup>9</sup>	3	1.10 ± 0.20	-1.04 ± 0.28	0.23 ± 0.05	-0.00 ± 0.00	0.39 ± 0.04	0.24 ± 0.03	0.12 ± 0.02	0.49 ± 0.02	0.24 ± 0.01	2.64 ± 0.02	-
NGC 777 <sup>9</sup>	4	2.34 ± 0.74	-0.31 ± 1.10	-0.22 ± 0.20	0.09 ± 0.05	0.33 ± 0.12	0.66 ± 0.03	0.17 ± 0.04	0.33 ± 0.08	0.02 ± 0.01	2.09 ± 0.07	-
NGC 1052	1	56.64 ± 0.56	9.73 ± 1.00	4.44 ± 0.18	2.32 ± 0.08	10.71 ± 0.09	6.84 ± 0.06	5.73 ± 0.11	13.03 ± 0.11	12.68 ± 0.06	8.54 ± 0.15	7.69 ± 0.12
NGC 1052	2	31.55 ± 0.78	3.89 ± 0.77	2.03 ± 0.17	2.23 ± 0.14	5.14 ± 0.10	2.96 ± 0.04	3.23 ± 0.09	6.98 ± 0.11	6.66 ± 0.04	5.23 ± 0.10	3.81 ± 0.07
NGC 1052	3	13.17 ± 0.64	1.47 ± 0.77	0.81 ± 0.16	0.43 ± 0.05	1.48 ± 0.08	0.83 ± 0.04	0.94 ± 0.06	2.56 ± 0.09	2.22 ± 0.02	1.85 ± 0.08	1.34 ± 0.06
NGC 1052	4	2.69 ± 0.63	0.24 ± 1.14	0.43 ± 0.19	0.10 ± 0.08	0.46 ± 0.11	0.01 ± 0.01	0.42 ± 0.05	0.87 ± 0.09	0.43 ± 0.02	0.33 ± 0.07	0.28 ± 0.05
NGC 1209	1	6.97 ± 0.53	-0.30 ± 0.73	0.67 ± 0.15	0.37 ± 0.05	0.87 ± 0.07	0.19 ± 0.03	0.85 ± 0.04	1.47 ± 0.07	2.22 ± 0.01	0.80 ± 0.06	0.67 ± 0.05
NGC 1209	2	5.42 ± 0.50	-0.55 ± 0.82	0.73 ± 0.17	0.41 ± 0.05	0.84 ± 0.07	0.21 ± 0.03	0.73 ± 0.04	1.35 ± 0.08	1.91 ± 0.02	0.55 ± 0.06	0.54 ± 0.05
NGC 1209	3	3.49 ± 0.58	-1.06 ± 1.07	0.78 ± 0.19	0.35 ± 0.10	0.53 ± 0.12	0.23 ± 0.02	0.43 ± 0.04	1.05 ± 0.08	1.22 ± 0.02	0.31 ± 0.06	0.32 ± 0.05
NGC 1209	4	0.43 ± 0.55	-0.55 ± 1.08	0.39 ± 0.19	0.35 ± 0.11	0.35 ± 0.20	0.15 ± 0.04	0.27 ± 0.04	0.43 ± 0.09	0.44 ± 0.02	-0.04 ± 0.06	-0.00 ± 0.05
NGC 1297	1	7.88 ± 0.90	0.47 ± 1.46	0.40 ± 0.21	0.38 ± 0.11	0.81 ± 0.14	0.33 ± 0.03	0.66 ± 0.05	1.67 ± 0.11	1.46 ± 0.02	1.07 ± 0.08	0.99 ± 0.06
NGC 1297	2	4.66 ± 0.59	-0.04 ± 1.17	0.45 ± 0.19	0.37 ± 0.11	0.82 ± 0.17	0.38 ± 0.04	0.51 ± 0.03	1.15 ± 0.08	0.93 ± 0.02	0.71 ± 0.06	0.59 ± 0.04
NGC 1297	3	3.22 ± 0.64	0.63 ± 0.99	0.45 ± 0.22	0.48 ± 0.12	0.47 ± 0.13	0.09 ± 0.04	0.38 ± 0.04	0.72 ± 0.10	0.47 ± 0.02	0.29 ± 0.06	0.25 ± 0.03
NGC 1297	4	1.43 ± 0.31	0.75 ± 0.82	0.17 ± 0.31	0.19 ± 0.10	0.47 ± 0.10	0.54 ± 0.03	0.71 ± 0.05	1.17 ± 0.12	-0.17 ± 0.02	1.02 ± 0.08	0.22 ± 0.05
NGC 1380	1	1.88 ± 0.50	-0.46 ± 0.69	0.42 ± 0.15	0.23 ± 0.05	0.64 ± 0.07	0.32 ± 0.03	0.86 ± 0.05	1.48 ± 0.08	1.98 ± 0.02	0.60 ± 0.06	0.61 ± 0.07
NGC 1380	2	1.95 ± 0.47	0.00 ± 0.67	0.32 ± 0.15	0.18 ± 0.05	0.49 ± 0.07	0.21 ± 0.03	0.62 ± 0.04	1.50 ± 0.07	1.67 ± 0.02	0.59 ± 0.06	0.43 ± 0.05
NGC 1380	3	1.43 ± 0.42	-0.13 ± 0.64	0.30 ± 0.14	-0.01 ± 0.02	0.34 ± 0.07	0.19 ± 0.04	0.50 ± 0.04	1.30 ± 0.08	1.38 ± 0.01	0.58 ± 0.06	0.37 ± 0.05
NGC 1380	4	0.79 ± 0.38	0.02 ± 0.71	0.36 ± 0.15	0.02 ± 0.06	0.37 ± 0.09	0.01 ± 0.01	0.50 ± 0.04	0.88 ± 0.07	0.88 ± 0.02	0.32 ± 0.05	0.15 ± 0.04
NGC 1453	1	10.44 ± 0.53	0.12 ± 0.61	0.82 ± 0.16	0.52 ± 0.07	1.20 ± 0.08	0.36 ± 0.03	1.02 ± 0.05	2.14 ± 0.07	2.93 ± 0.01	1.57 ± 0.07	1.22 ± 0.06
NGC 1453	2	7.87 ± 0.57	-0.28 ± 0.77	0.82 ± 0.17	0.58 ± 0.06	1.12 ± 0.07	0.22 ± 0.03	0.84 ± 0.05	1.70 ± 0.08	2.09 ± 0.01	0.97 ± 0.07	0.88 ± 0.07
NGC 1453	3	4.15 ± 0.49	-0.70 ± 0.88	0.69 ± 0.15	0.51 ± 0.06	0.91 ± 0.09	0.08 ± 0.01	0.44 ± 0.04	1.01 ± 0.07	1.08 ± 0.02	0.33 ± 0.05	0.48 ± 0.06
NGC 1453	4	3.90 ± 0.51	-0.33 ± 1.07	0.62 ± 0.17	0.26 ± 0.10	1.05 ± 0.21	-0.00 ± 0.04	0.35 ± 0.05	1.05 ± 0.08	0.96 ± 0.02	0.36 ± 0.06	0.20 ± 0.04
NGC 1521 <sup>9</sup>	1	0.82 ± 0.41	0.06 ± 0.90	0.09 ± 0.13	0.19 ± 0.04	0.18 ± 0.08	-0.00 ± 0.01	0.36 ± 0.04	0.78 ± 0.08	1.00 ± 0.02	0.18 ± 0.07	0.15 ± 0.06
NGC 1521 <sup>9</sup>	2	0.76 ± 0.51	0.09 ± 1.14	0.15 ± 0.18	0.03 ± 0.09	0.08 ± 0.14	-0.00 ± 0.01	0.14 ± 0.04	0.55 ± 0.08	0.61 ± 0.02	0.23 ± 0.04	0.13 ± 0.03
NGC 1521 <sup>9</sup>	3	0.88 ± 0.48	-0.06 ± 0.99	-0.02 ± 0.18	-0.01 ± 0.10	0.14 ± 0.16	0.00 ± 0.01	0.38 ± 0.04	0.27 ± 0.08	0.47 ± 0.02	0.10 ± 0.04	0.09 ± 0.04
NGC 1521 <sup>9</sup>	4	0.33 ± 0.42	-0.61 ± 0.82	0.25 ± 0.18	0.23 ± 0.11	0.67 ± 0.19	0.09 ± 0.02	-0.02 ± 0.02	0.39 ± 0.11	0.27 ± 0.03	0.03 ± 0.04	0.02 ± 0.02
NGC 1533	1	4.51 ± 0.59	0.29 ± 0.52	0.75 ± 0.18	0.43 ± 0.06	1.26 ± 0.07	0.55 ± 0.03	0.77 ± 0.04	1.60 ± 0.08	1.77 ± 0.01	0.64 ± 0.06	0.53 ± 0.05
NGC 1533	2	3.80 ± 0.53	-0.45 ± 0.88	0.77 ± 0.17	0.35 ± 0.06	0.94 ± 0.08	0.31 ± 0.03	0.46 ± 0.04	1.06 ± 0.08	1.06 ± 0.02	0.39 ± 0.06	0.33 ± 0.05
NGC 1533	3	4.38 ± 0.56	0.03 ± 0.96	0.64 ± 0.18	0.53 ± 0.08	1.22 ± 0.11	0.17 ± 0.04	0.31 ± 0.04	0.94 ± 0.08	0.75 ± 0.02	0.52 ± 0.06	0.38 ± 0.05
NGC 1533	4	3.53 ± 0.64	-0.11 ± 1.15	0.40 ± 0.17	0.36 ± 0.12	0.64 ± 0.08	0.02 ± 0.02	0.30 ± 0.04	0.94 ± 0.09	0.73 ± 0.02	0.68 ± 0.06	0.35 ± 0.04

Notes. <sup>(7)</sup> Reg 1 =  $r \leq r_c/16$ ; Reg 2 =  $r_c/16 < r \leq r_c/8$ ; Reg 3 =  $r_c/8 < r \leq r_c/4$ ; Reg 4 =  $r_c/4 < r \leq r_c/2$ . <sup>(8)</sup> Negative emission values are consistent with no emission. <sup>(9)</sup> The continuum was fitted with 2 SSPs

## Appendix A: Short description of morphological and kinematic characteristics and peculiarities of the galaxy sample (Paper I+Paper II)

We collect in Table A1 the morphological and kinematic characteristics, as well as the peculiarities, of the complete R05+A06 sample. The morphological and kinematic properties in Table A1 are derived from the literature, and were in part already described in the Appendix (provided as on-line material) of Paper I and Paper II.

We list in Cols. 3 and 4 the galaxy ellipticity,  $\epsilon$ , and the  $(V/\sigma)_{\text{scaled}}$ . The latter is computed from slit spectroscopy measurements through the relation provided by Cappellari et al. (2007),  $(V/\sigma)_{\text{scaled}} = 0.57 \times (V/\sigma)_{\text{slit}}$ . It should be a reasonable approximation of the  $(V/\sigma)_e$ , computed on a luminosity weighted spectrum within  $r_e$ . For the eight galaxies in common with the SAURON sample, i.e. NGC 2974, NGC 3489, NGC 4374, NGC 4552, NGC 5813, NGC 5831, NGC 5846 and NGC 7332, the  $\epsilon$  and  $V/\sigma$  values are those derived through integral field spectroscopy. Cappellari et al. (2007) noticed that there is a good agreement between  $\epsilon$  values derived in the literature with different methods.

Emsellem et al. (2007) defined a new parameter,  $\lambda_R = \langle R|V| \rangle / \langle R \sqrt{V^2 + \sigma^2} \rangle$ , where  $R$  is the galacto-centric distance, and  $V$  and  $\sigma$  are luminosity weighted averages over the two-dimensional kinematic field. This parameter is a proxy to quantify the observed projected stellar angular momentum per unit mass, and can be used to classify ETGs into slow or fast rotators. In the  $\epsilon$  vs.  $(V/\sigma)_e$  plane, Cappellari et al. (2007) identified a region ( $0.0 \lesssim \epsilon \lesssim 0.3$ ,  $0.0 \lesssim (V/\sigma)_e \lesssim 0.13$ ) where slow-rotators are generally found. Lacking the 2D  $V$  and  $\sigma$  information for most of our galaxies, we used  $(V/\sigma)_{\text{scaled}}$  to identify in the  $\epsilon$  vs.  $(V/\sigma)_e$  plane the fast and slow rotators. The derived classification is provided in Col. 5 of Table A1 (F = fast rotator; S = slow rotator). We obtain that  $\approx 68\%$  (36/53) of our sample is fast rotator (to be compared with 75% fast rotators in the SAURON sample). Less than 1/3 of our galaxies are slow rotators (vs. 25% in the SAURON sample).

In Cols. 6 and 7 of Table A1 we provide the kinematic and morphological peculiarities, respectively. A large fraction, approximately 50% of our ETGs, displays kinematic peculiarities, like counter-rotation, or peculiar faint features, like shells, tails, or decoupled gas distributions with respect to the stars.

**Table A.1.** Kinematic and morphological overview.

Ident	RSA	$\epsilon$	$(V/\sigma)_{\text{scaled}}$	Rot. class	Gas vs. stars kinematic peculiarities	Gas vs. stars morphological peculiarities
NGC 128	S02(8) pec	0.67	0.44	F	CR g-s (1)	g- d and g-maj $t \approx 23^\circ$ (5)
NGC 777	E1	0.21	0.06	S		
NGC 1052	E3/S0	0.28	0.27	F	CR g-g (1,5)	
NGC 1209	E6	0.52	0.50	F		X- like struct.; NW linear feature (2)
NGC 1297	S02/3(0)	0.13				
NGC 1366	E7/S01(7)	0.56				
NGC 1380	S03(7)/Sa	0.41	0.59	F		
NGC 1389	S01(5)/SB01	0.37				
NGC 1407	E0/S01(0)	0.07	0.11	S	rotat. min. axis (5)	
NGC 1426	E4	0.34	0.40	F		
NGC 1453	E0	0.17				g-d and g-maj $t$ (5)
NGC 1521	E3	0.35	0.54	F		
NGC 1533	SB02(2)/SBa	0.19				
NGC 1553	S01/2(5)pec	0.38	0.68	F		shells (3)
NGC 1947	S03(0) pec	0.11	0.23	F	rotat. min. axis (5)	dust-lane min. axis (5)
NGC 2749	E3	0.07	0.21	F	rotat. min. axis (5)	
NGC 2911	S0p or S03(2)	0.32				
NGC 2962	RSB02/Sa	0.37	0.51	F		
NGC 2974	E4	0.37	0.70	F		shells (2); g-d and g-maj $t \approx 20^\circ$ (5)
NGC 3136	E4	0.24	0.67	F	CR s-s (5)	
NGC 3258	E1	0.13	0.08	S	CR g-s (1)	
NGC 3268	E2	0.24	0.53	F		
NGC 3489	S03/Sa	0.37	0.29	F	gas rot. min. axis (5)	
NGC 3557	E3	0.21	0.30	F		SW fan; asym. outer isophotes (2)
NGC 3607	S03(3)	0.11	0.28	F		
NGC 3818	E5	0.36	0.27	F		
NGC 3962	E1	0.22	0.23	F		gas disk+outer arc-like struct. (5)
NGC 4374	E1	0.13	0.03	S		
NGC 4552	S01(0)	0.06	0.05	S		shells (3)
NGC 4636	E0/S01(6)	0.24	0.07	S	gas irr. motion (5)	
NGC 4696	(E3)	0.34	0.18	F		Faint outer shells (2)
NGC 4697	E6	0.32	0.39	F		Non spherical inner isophotes (2)
NGC 5011	E2	0.15	0.11	S		
NGC 5044	E0	0.11	0.13	F	CR s-s; gas irr.motion (5)	gas fil. shape (5)
NGC 5077	S01/2(4)	0.15	0.06	S	CR s-s (5); g-d and g-maj $t \approx 90^\circ$ (5)	
NGC 5090	E2	0.15	0.17	F		
NGC 5193	S01(0)	0.07				
NGC 5266	S03(5) pec	0.31	0.12	S	stellar rot. min. axis (5)	dust-lane and gas along min. axis (5)
NGC 5328	E4	0.31				
NGC 5363	[S03(5)]	0.34	0.39	F		dust-lane along min. axis (5)
NGC 5638	E1	0.11	0.21	F		
NGC 5812	E0	0.13	0.11	S		Tidal tail (2)
NGC 5813	E1	0.15	0.14	S	CR s-s; gas irr. motion (5)	gas fil. shape (5)
NGC 5831	E4	0.15	0.08	S	CR s-s (6,7)	
NGC 5846	S01(0)	0.07	0.03	S	gas irr. motion (5)	Faint outer shells (2)
NGC 5898	S02/3(0)	0.07	0.21	F	CR g-s (1)	Three spiral arm-like tidal tails (2)
NGC 6721	E1	0.15	0.26	F		
NGC 6758	E2 (merger)	0.22	0.12	S	CR g-s (5)	
NGC 6776	E1 pec	0.17	0.24	F		shell or loops NE (3,4); gas fil. shape (5)
NGC 6868	E3/S02/3(3)	0.19	0.14	F	CR g-s (5)	
NGC 6875	S0/a(merger)	0.41				
NGC 6876	E3	0.13				
NGC 6958	R?S01(3)	0.15	0.20	F		Shells (2,3)
NGC 7007	S02/3/a	0.42			CR g-s (1)	g-d and g- maj $t \approx 30^\circ$ (5)
NGC 7079	SBa	0.32	0.96	F	CR g-s + s-s (1)	
NGC 7097	E4	0.29	0.10	S	CR s-s (1)	
NGC 7135	S01 pec	0.31	0.20	F		jet-like debris and shells (3)
NGC 7192	S02(0)	0.15	0.04	S	CR s-s (5)	Shell (2)
NGC 7332	S02/3(8)	0.42	0.32	F	CR g-g (1)	
NGC 7377	S02/3/Sa pec	0.19				
IC 1459	E4	0.28	0.10	S	CR g-g (1)	shells (2)
IC 2006	E1	0.15	0.16	F	CR g-s (1)	
IC 3370	E2 pec	0.21	0.28	F		X-like struct.; broad N fan (2); polar ring ? (5)
IC 4296	E0	0.17	0.13	F	CR s-s (5)	
IC 5063	S03(3)pec/Sa	0.28	0.26	F		

**Notes.** Columns. 4 and 5 list respectively  $(V/\sigma)_{\text{scaled}} = 0.57(V/\sigma)_{\text{slit}}$ , and the rotation class (F = fast rotator; S = slow rotator). Legend: **CR g-s**: counter rotation gas vs. stars; **CR s-s**: counter rotation stars vs. stars; **CR g-g**: counter rotation gas vs. gas; **stars rotat. min. axis**: stars rotate along the galaxy minor axis; **g-d and g-maj t**: gas disk and galaxy major axis are tilted by the reported angle, if provided in the literature.

**References.** (1) Corsini & Bertola 1998; (2) Tal et al. 2009; (3) Malin & Carter 1983; (4) Pierfederici & Rampazzo 2004; (5) the description of the kinematic and morphological peculiarities of the galaxies and full references are reported in the on-line notes of Paper I and Paper II; (6) Davies et al. 1983; (7) Emsellem et al. 2004.

## Appendix B: Emission line ratios for the total sample in annuli of increasing galacto-centric distance

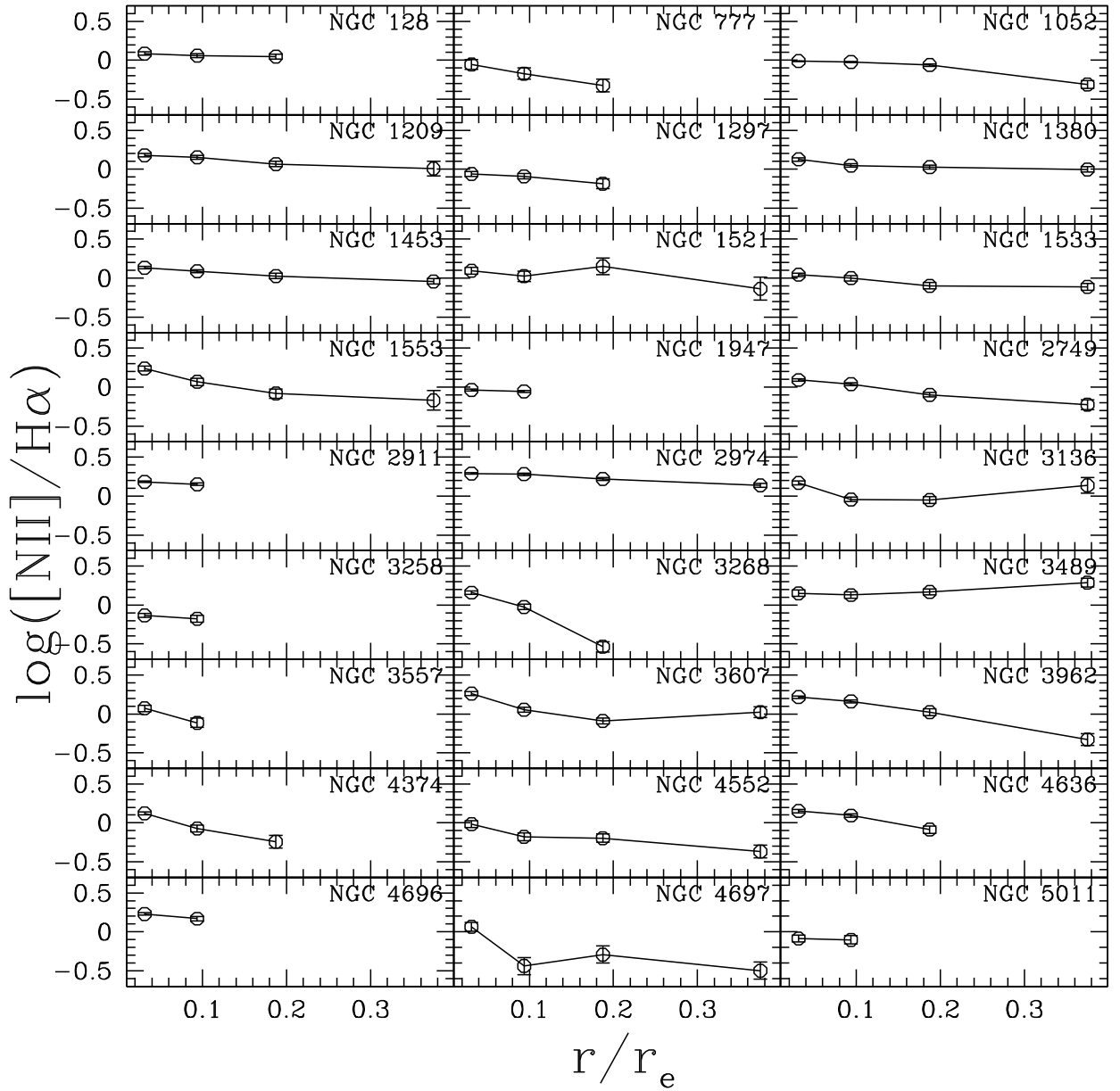


**Fig. B.1.**  $\log([NII]/H\alpha)$  ratio for the sample in the annuli  $r \leq r_e/16$ ,  $r_e/16 < r \leq r_e/8$ ,  $r_e/8 < r \leq r_e/4$ , and  $r_e/4 < r \leq r_e/2$ .

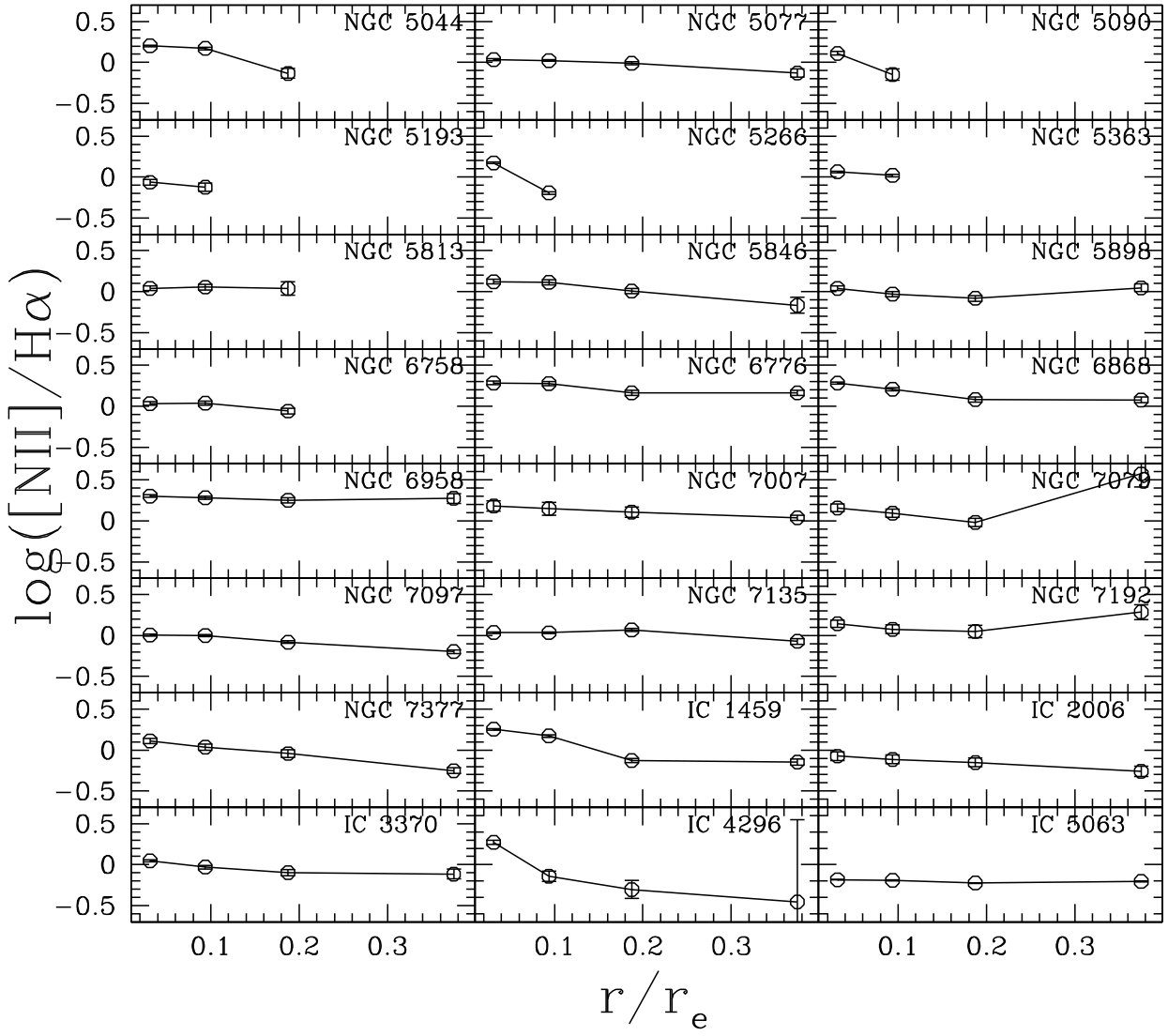


**Fig. B.2.**  $\log([NII]/H\alpha)$  ratio for the sample in the annuli  $r \leq r_e/16$ ,  $r_e/16 < r \leq r_e/8$ ,  $r_e/8 < r \leq r_e/4$ , and  $r_e/4 < r \leq r_e/2$ .

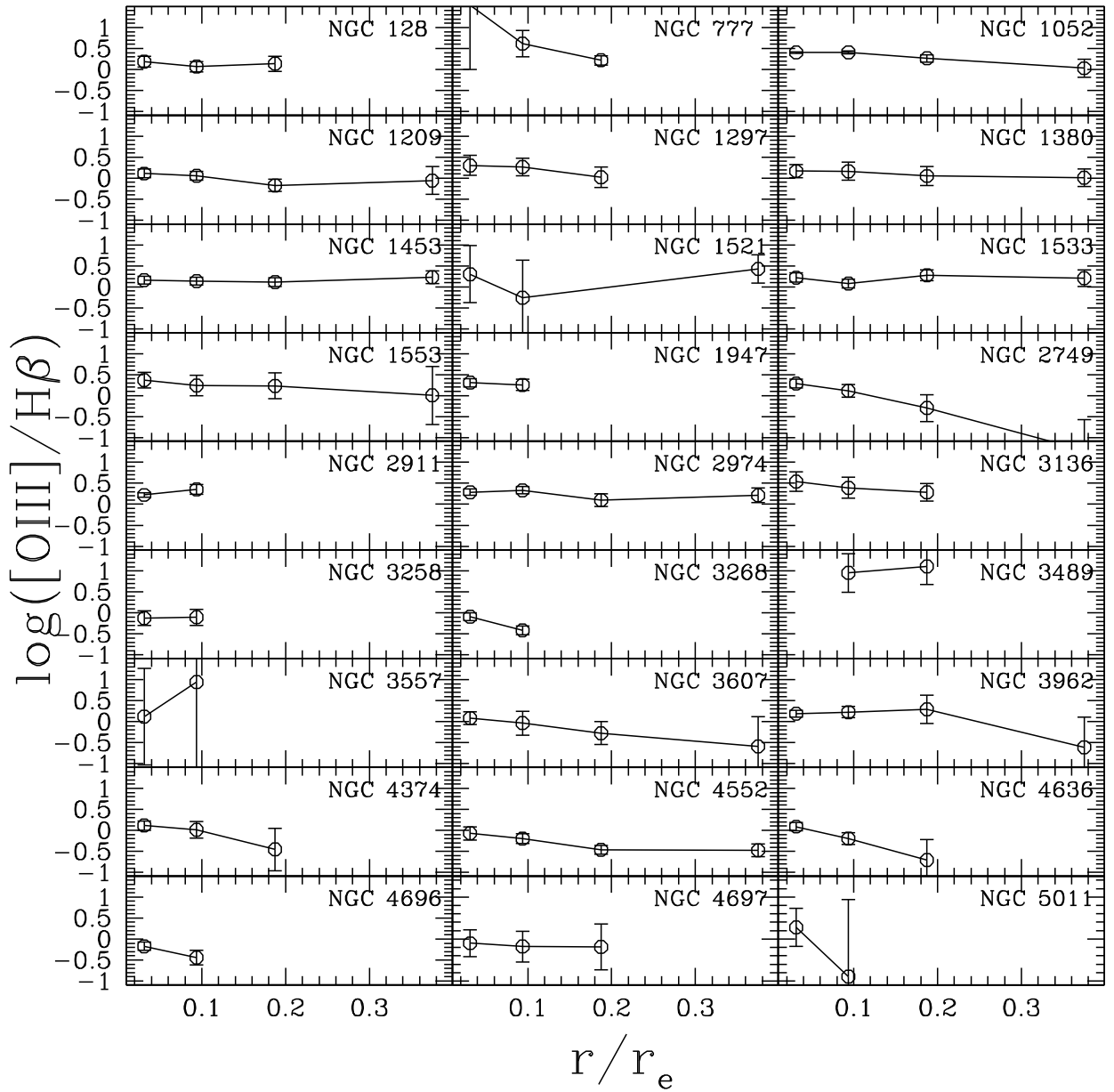


**Fig. B.3.**  $\log([\text{OIII}]/\text{H}\beta)$  ratio for the sample in the annuli  $r \leq r_e/16$ ,  $r_e/16 < r \leq r_e/8$ ,  $r_e/8 < r \leq r_e/4$ , and  $r_e/4 < r \leq r_e/2$ .

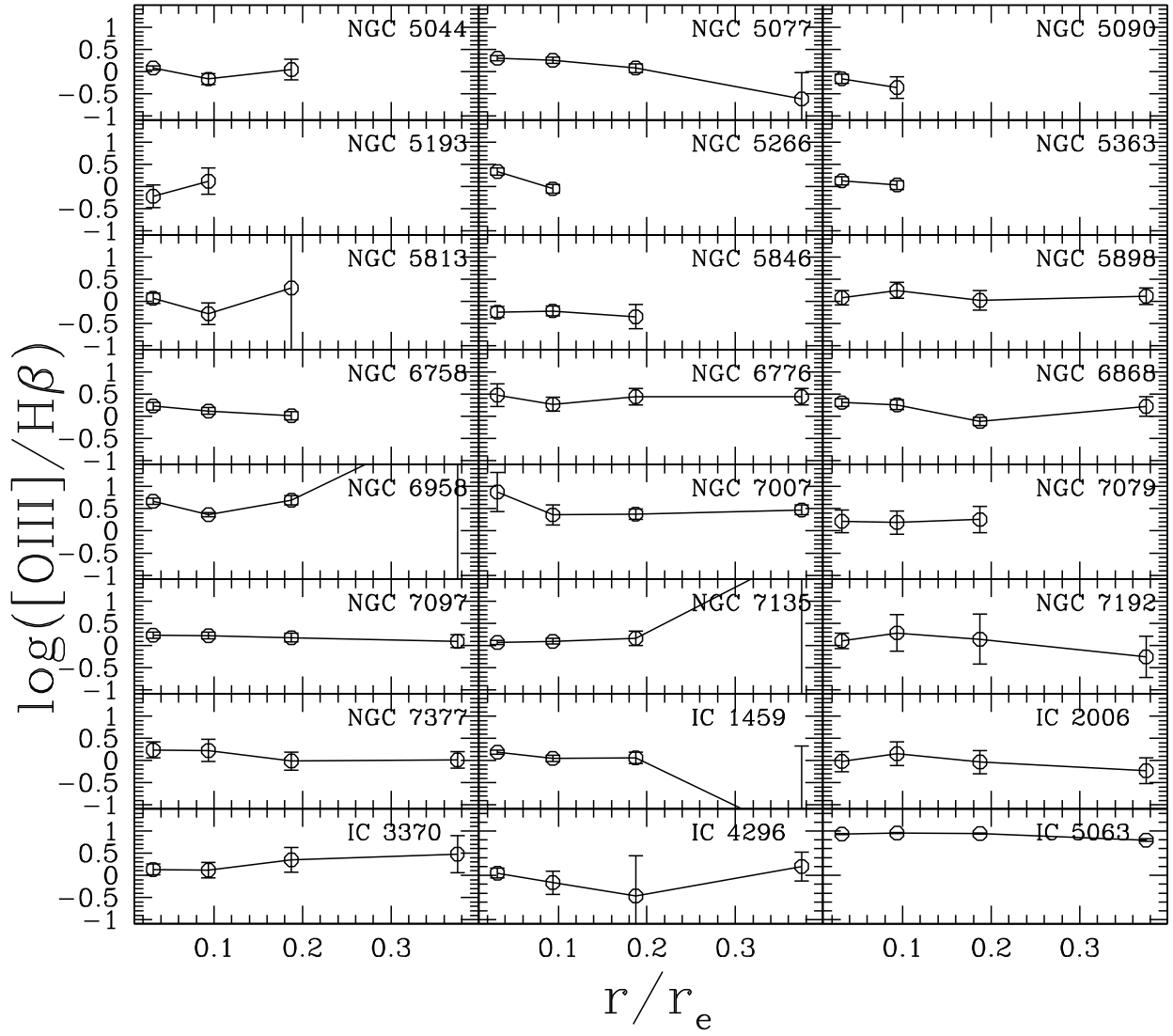


**Fig. B.4.**  $\log([\text{OIII}]/\text{H}\beta)$  ratio for the sample in the annuli  $r \leq r_e/16$ ,  $r_e/16 < r \leq r_e/8$ ,  $r_e/8 < r \leq r_e/4$ , and  $r_e/4 < r \leq r_e/2$ .